Andreas Sandvik

Probabilistic ductile fracture assessment of pipelines

Thesis for the degree philosophiae doctor

Trondheim, March 2007

Norwegian University of Science and Technology
Faculty of Engineering Science and Technology
Department of Engineering Design and Materials

NTNU
Innovation and Creativity

NTNU
Norwegian University of Science and Technology

Thesis for the degree philosophiae **doctor**

Faculty of Engineering Science and Technology
Department of Engineering Design and Materials

ISBN 978-82-471-0668-6 (printed version)
ISBN 978-82-471-0671-6 (electronic version)
ISSN 1503-8181

Doctoral theses at NTNU, 2007:31

Printed by NTNU-trykk

Preface

This thesis comprises on introduction and three journal papers. Paper 1 is published in Engineering Fracture Mechanics, where also Paper 2 is accepted with minor revision. Paper 3 is submitted for publication in International Journal of Fracture.

I have been the main author and responsible for the implementation and simulations in all the papers. However, I have received helpful contributions, corrections and comments from the co-authors. The framework and methodology in Paper 1 are built on strain-based fracture mechanics equations derived by Erling Østby (second author).

Abstract

The thesis comprises on introduction chapter and three journal papers considering probabilistic fracture assessment of pipes, using three different approaches.

In Paper 1 semi-analytical strain-based equations for surface cracked pipes were used to establish probabilistic fracture assessment models. The pipes were subjected to global plastic strains, and the tangency criterion was used to determine the global failure strain. The results showed that the strain capacity and the CTOD were strongly influenced by the effect of internal pressure. A major drop in the probability of failure was observed as the pressure increased. Similarly, the crack depth also strongly influenced the probability of failure together with the global strain capacity. The effect from increasing the crack length in the hoop direction also resulted in an increase in the probability of failure. The reliability analyses employed the FORM and SORM techniques. It should be noted that no explicit capacity term in the limit state function was calculated. Point-wise capacity solutions were obtained from an iterative procedure linked to the probabilistic software Proban.

In Paper 2 the probabilistic model is based on 3D FEM models including the effect of ductile tearing using the Gurson-Tvergaard-Needleman model. The quasi-static FEM-solutions were obtained using Abaqus/Explicit, which originally was developed for scenarios where shock and mass effects play an important role. The simulations showed how the Abaqus/Explicit solver enabled detailed analyses of a pipe with a surface defect. The different simulations were used to establish so-called response surfaces. These surfaces (i.e. equations) represented the capacity term in the limit state equation. The pipes were subjected to uniform tension in combination with internal pressure. The results showed a loss of capacity when the internal pressure was included. Additionally, a significant decrease in strain capacity was observed when the crack depth increased. Finally, the variation in crack length and material hardening also influenced the global strain capacity and the CTOD. The probability of failure was calculated using FORM and SORM.

In Paper 3 a computationally attractive method using line-springs and shell elements is used to establish a probabilistic fracture mechanics (PFM) model. The crack was represented by nonlinear finite element springs, line-springs, with various compliance dependent on the plastic deformation and the crack depth. Ductile tearing is included using the traditional CTOD-Δa relationship. As a result, the material resistance curve was included in the PFM-model together with crack depth, crack length and internal pressure. The results illustrated the effect of variation in material resistance and the internal pressure. The model was also found to be applicable for engineering purposes.

Acknowledgements

This thesis contains the main results from my work during the past three years. The work has been a part of the Joint Industry Project "Fracture Control - Offshore Pipelines" with the following funding participants: Statoil, Hydro, BP, ENI Norge, Technip and the Research Council of Norway.

The supervisors from The Norwegian University of Science and Technology have been Professor Dr.ing. Christian Thaulow and Professor Dr.ing. Dr.tech. Arvid Naess. Their assistance, encouragement and advice throughout the study are greatly acknowledged.

I have worked in close cooperation with Dr.ing. Erling Østby (Sintef). His patient and thorough guidance and criticism throughout the research study has been highly appreciated.

I also appreciate the assistance provided by Dr. Gudfinnur Sigurdsson (Det Norske Veritas) with programming of the probabilistic framework, and by Dr.ing. Knut-Aril Farnes (Statoil) with programming topics in Fortran and Matlab. I also want to thank my Statoil colleagues Dr. Richard Verley, Dr.ing. Mons Hauge and Dr.ing. Per Gerhard Grini. Richard helped me with proof-reading the manuscript, and Mons gave me the opportunity to embark on the doctoral program. Per Gerhard has motivated me to keep the time schedule, which has been important to me. When I struggled with the research progress the advice was simple but effective: don't give up; work!

Finally, I want to thank my family and colleagues for their patience and support during my PhD-study.

Contents

1 Introduction and motivation **1**
1.1 Elastic-plastic fracture mechanics 3
1.1.1 Constraint 5
1.2 Ductile crack-growth simulation 7
1.3 Failure criteria 8
1.4 Reliability analysis 9

References **12**

Paper 1: Probabilistic fracture assessment of surface cracked pipes using strain-based approach **17**

1 Nomenclature **18**

2 Introduction **19**

3 Structural reliability - establishment of the probability of failure **21**

4 The probabilistic fracture mechanics model **23**
4.1 The strain-based simplified fracture mechanics equation 24
4.2 Calculation of the critical strain - ε_{crit} 30
4.2.1 Strain due to external loading, ε_{app} 31
4.2.2 Defect location, effective crack length and modified strain . 31
4.2.3 Defect distributions 33

5 Results **35**
5.1 Analyses using deterministic defect values 35
5.2 Calculations using stochastic crack geometry values 36
5.3 Comparison of FORM and SORM calculations 37

6 Concluding remarks and discussion **38**

References **41**

Appendix **43**

A Relationship between J and CTOD **44**

Paper 2: A probabilistic fracture mechanics model including 3D ductile tearing of bi-axially loaded pipes with surface cracks **47**

1 Introduction **48**

2 3D FE-models **50**
2.1 Solution method and solution quality 54

3 Results and discussion **55**

4 The probabilistic fracture mechanics model **62**
4.1 Failure and response surfaces 65
4.2 Global failure criterion 66
4.3 Local failure criterion 66
4.4 Example using the PFM-model 69

5 Results and discussion **71**
5.1 Limitations 73

6 Conclusions and further work **74**

References **75**

Paper 3: A probabilistic ductile fracture mechanics model for biaxially loaded surface-cracked pipes using shell and line-spring elements **81**

1 Introduction **83**

2 FEM-model **84**
2.1 Results from FEM simulations 89

3 The probabilistic fracture mechanics model **93**
3.1 Failure and response surfaces 96
3.2 Failure criteria 96
3.3 Example 98

4 Results of the probabilistic simulations **98**
4.1 Discussion 105

5 Conclusions **105**

References **106**

1 Introduction and motivation

Structure of the thesis

This thesis contains an introduction section and three journal papers which were completed consecutively during the course of the past three years. I have also contributed at four international conferences during the period, but these contributions are not presented herein.

There are some "disadvantages" in presenting a thesis based on journal papers. Firstly, the structure tends to be repetitive as each paper has a similar introduction section explaining the same motivation and background to the work. Additionally, it may be difficult to see the direct connection between the papers although they are close in topic. This is the main reason I have added a section giving the motivation of the project providing short discussions and some short explanations of the central concepts applied in the thesis. Finally, the journal structure does not cover all the work done.

One clarification should be noted on the vocabulary used: the meaning of a "crack" and "defect" are used synonymously.

Motivation

This thesis is about fracture mechanics assessment of offshore pipelines, where outer surface defects located in the circumferential direction are considered. Pipelines are used to transport oil and gas for short and long distances, and may be exposed to a large variation of loads, depending on the surroundings and area of application. In fracture mechanics assessment the main interest is focused on the loading conditions resulting in tensile strains. If a crack appears in a tensile region it may develop and grow sufficiently to cause structural failure. The behaviour depends on several factors, e.g. crack size and load level. During operation, the pipeline may be exposed to temperature loads resulting in lateral or upheaval buckling with subsequent large tensile and compression strains. Additionally, free-spans due to irregular seabed topography may also introduce large deformations, see illustration in Fig. 1. The effect of internal pressure may be important as well, since the resulting hoop stresses may cause the fracture mechanics response to change considerably when longitudinal tensile strains appears in the pipe. Another scenario where the pipeline is exposed to relatively large deformations is during laying. The level of deformation depends on the laying technique and the sea depth. Fig. 2 illustrates the principle of J- and S-laying. In J-laying the pipeline leaves the lay barge vertically. Typically, several linepipes of $\sim$ 12m length are girth-welded in the horizontal position, lifted into the vertical position and welded to the pipeline. In S-laying the linepipes are girth-welded on deck, the pipeline leaves the vessel horizontally and is (gradually) deformed/bent over the stinger. The tension in the pipeline must be adjusted to avoid local

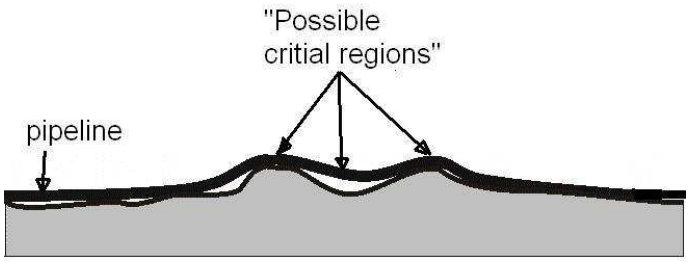

Figure 1: A possible seabed configuration for a pipeline with free-spans.

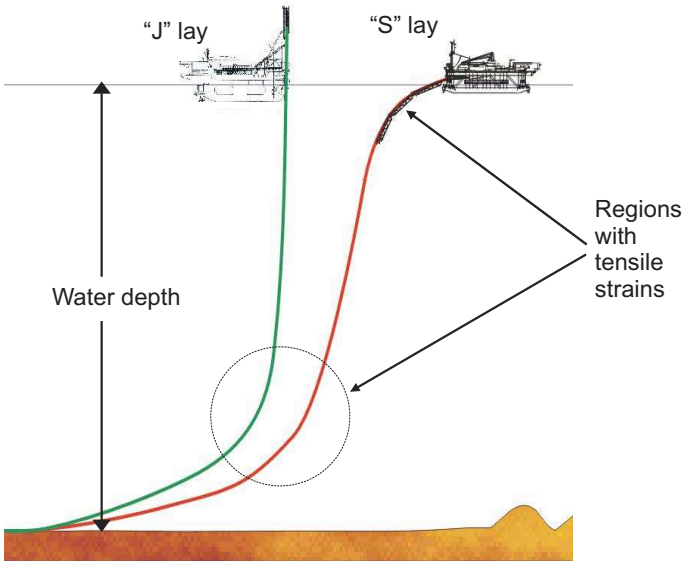

Figure 2: S- and J-laying technique. (Unknown origin of the figure)

buckling problems at touchdown on the seabed and when leaving the stinger.

Due to the nature of welding the resulting weld may contain defects, e.g. due to lack of fusion between weld and base material, or between the weld layers, or defects at the start-stop regions of the weld layers. A sketch of a girth-welded pipe with a surface defect is shown in Fig. 3. Fig. 4 gives a schematic view of the inspection process for girth welds for offshore pipelines. As the pipes are girth welded they are inspected, e.g. using automated ultrasonic testing (AUT) units, which are calibrated to detect defect-like cracks above a certain size. The AUT quality is ensured in qualification tests, and is represented by the probability of detection curve (POD). Since the weld inspection does not necessarily detects all the defects, some defects will pass undetected. These defects are shown as "Not observed defects" in Fig. 4. The detected defects exceeding a certain size will be repaired and re-inspected. As a result the defects remaining after welding, inspection and repair are represented in "Defect distribution before laying". This is the defect distribution that may be convenient to apply in probabilistic fracture assessment procedures for pipelines. When the structural and fracture response is known the probabilistic calculations can be used to calibrate safety factors in design equations. These are on the form

$$\frac{R}{\gamma_R} = L\gamma_L, \tag{1}$$

where R and L denotes the structural resistance and load, respectively. γ_R and γ_L are the partial safety factors. The partial safety factors are calibrated for different target reliability levels dependent on the area of application and failure mode. As a result, when a guideline is established, an engineer can employ it within the region of validity and be certain that he has achieved a safe and cost-effective design for the given operational conditions or laying procedure.

1.1 Elastic-plastic fracture mechanics

Linear elastic fracture mechanics (LEFM) is valid when there are only small local plastic deformations around the crack tip. The stress intensity factor K describes the stress field near the crack tip, see e.g. [1]. However, ductile materials may be impossible to characterize with LEFM when large plastic deformations appear around the crack tip. Consequently, other strategies have been developed to consider these situations.

Rice proposed the path-independent integral J as a fracture characterizing parameter for a nonlinear-elastic material. This implied the assumption of isotropic material, small strains, rate-independency and non-dissipative material behaviour. If $t_i = \sigma_{ij} n_j$ is the traction on the contour Γ, σ_{ij} the stress tensor and n_j the unit vector normal to Γ, the J-integral can be written as:

$$J = \int_\Gamma (W dy - t_i \frac{\partial u_i}{\partial x} ds). \tag{2}$$

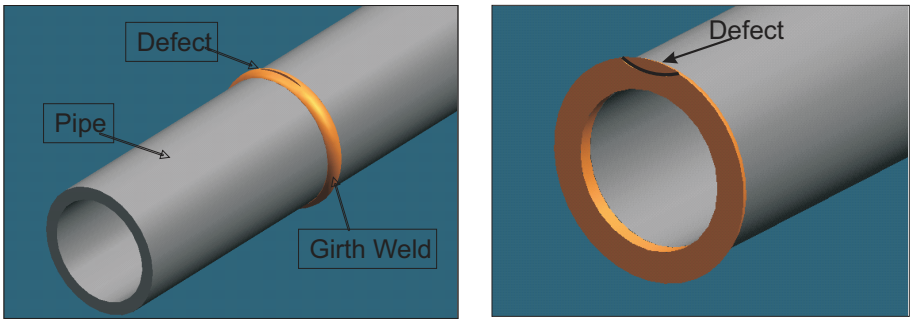

Figure 3: A girth-welded pipe with a defect. (Fig. used with permission from Snamprogetti.)

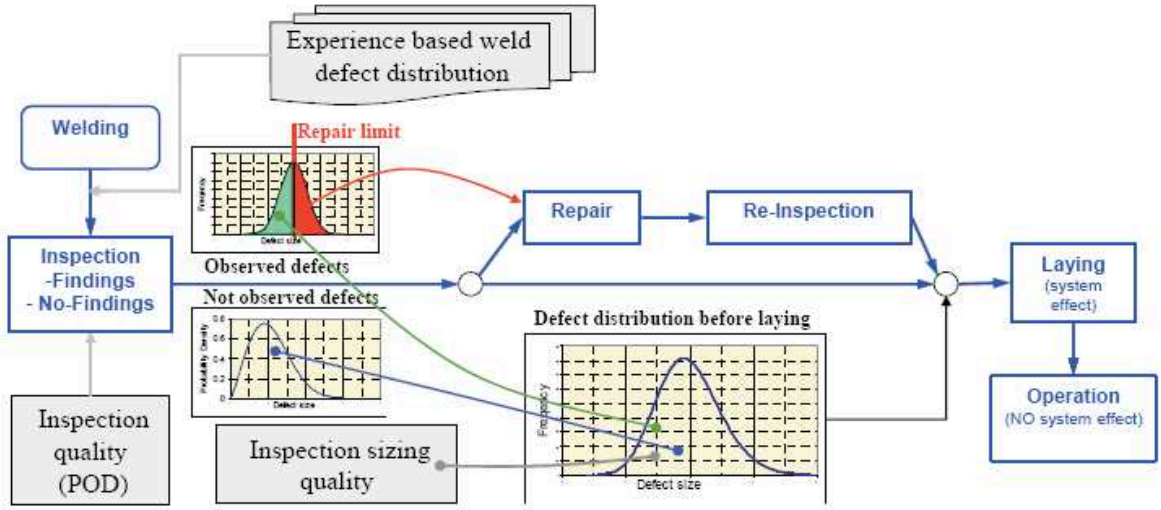

Figure 4: Schematic inspection process for girth welds in offshore pipelines. (Fig. is used with permission from DNV, Norway)

u_i denotes the displacement in direction i, and W is the strain energy density for a hyper-elastic material defined as:

$$\sigma_{ij} = \frac{\partial W}{\partial \varepsilon_{ij}}. \tag{3}$$

Hutchinson [2] and Rice and Rosengren [3] showed how the J-integral could be viewed as a stress intensity parameter that describes the asymptotic strain and stress fields in a nonlinear material obeying the Ramberg-Osgood strain-hardening function. Additionally, they showed that the stress and strain had to vary proportionally as $1/r$ near the crack tip to maintain the path independence for the J-integral, see Fig. 5. This is termed the Hutchinson-Rice-Rosengren (HRR) singularity.

The singular field around the crack tip does not exist in ductile materials. When large deformations appear around the crack tip, the crack tip blunts as indicated in Fig.6. The blunting results in a stress deviation from the HRR-solution. However, McMeeking [4] also showed that the HRR-solution was representative outside the near-tip region. As a consequence the J-parameter can also be applicable for situations involving large deformations. Rice [5] and Hutchinson [6] have shown that CTOD and the $J-$integral describe the ductile tearing behaviour sufficiently. An equivalence between J and CTOD has been shown for both a stationary and a growing crack by Shih [7], i.e.

$$J = m^* \sigma_{YS} \delta, \tag{4}$$

where m^* is a constant dependent on the material properties (mainly hardening) and stress state, σ_{YS} is the yield stress, and δ is the CTOD. In this thesis, however, the following relation has been applied:

$$J = m \sigma_{0.2} \delta, \tag{5}$$

where $\sigma_{0.2}$ denotes the yield stress at 0.2% plastic strain, and the m-factor is

$$m(\sigma_{0.2}/\sigma_{TS}) = 3.87 - 2.64(\sigma_{0.2}/\sigma_{TS}). \tag{6}$$

σ_{TS} denotes the tensile strength. The explanation for use of this function is found in Appendix A in Paper 1.

In the first paper J is used as fracture mechanics parameter, whereas with the two last papers CTOD is used for characterization of initiation and growth of ductile cracks.

1.1.1 Constraint

Geometry and mode of loading can influence the conditions around the crack tip, and therefore influence the fracture toughness. This is termed geometric

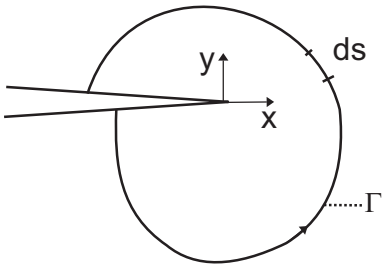

Figure 5: An arbitrary contour line around a crack tip for J-integral evaluation.

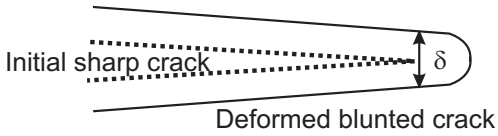

Figure 6: An initially sharp crack that is blunted due to inelastic deformations at the crack tip. The CTOD is depicted as δ.

constraint effect. When this effect is taken into account the one parameter theory must be extended. Betegon and Hancock [8] investigated the the stress field in front of the crack for different geometric constraint levels for a hardening material. They showed that the constraint could be represented by the T-stress parameter. The two-parameter theory is named J-T theory. Another approach is the J-Q theory proposed by O'Dowd and Shih [9, 10]. The theory behind two-parameter fracture mechanics is not presented in detail, and readers are referred to the references above for a more in-depth presentation The basis for not addressing constraint issues in this work can be seen from Fig. 7, showing the constraint level in different fracture mechanics specimens compared to the constraint level in pipes. Recent developments in fracture assessment of pipelines have tended towards using the SENT specimen in determination of the fracture toughness, see e.g. Nyhus et al. [11]. From Fig. 7 it can be observed that the constraint levels in pipes and SENT specimens are of negligible difference, thus, using the fracture toughness from the latter should give representative values also for the pipes without further corrections. In this work it has been assumed that crack growth resistance curves are obtained using SENT specimens, and the variation in fracture toughness is rather assumed to be due to variation in material properties, and not directly due to differences in constraint level.

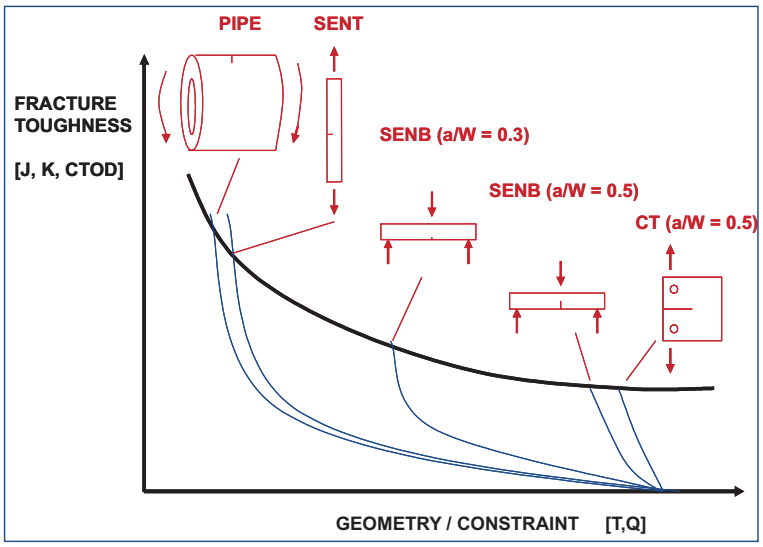

Figure 7: Illustration on how the fracture toughness varies with the constraint level. (Fig. used with permission from B. Nyhus, Sintef)

1.2 Ductile crack-growth simulation

J-Δa and CTOD-Δa curves

In Paper 1 the $J - \Delta a$ curve was employed to advance the crack front in the strain-based equations. This means that the connection between J and the crack growth, Δa, is known prior to the analysis. In the Paper 2 the Gurson-Tvergaard-Needleman model is adjusted to obtain a wanted CTOD-Δa relationship. In the Paper 3, the CTOD-Δa curve is applied as input to the Link$_{pipe}$ software.

Gurson-Tvergaard-Needleman

In the second paper 3D FEM analyses are conducted where the Gurson-Tvergaard-Needleman approximate yield model was applied to model the effect of ductile tearing. This ductile crack growth model was proposed by Gurson [12], and later modified [13,14]. The model simulates the microvoid nucleation, growth and coalescence, and assumes that the porous material behaves like a continuum where the plastic yield surface is adjusted dependent on the hydrostatic stress level and current void volume fraction. The yield condition is expressed as

$$g(\sigma_e, \sigma_m, \bar{\sigma}, f^*) = (\frac{\sigma_e}{\bar{\sigma}})^2 + 2q_1 f^* \cosh(\frac{3q_2\sigma_m}{2\bar{\sigma}}) - (1 + q_3(f^*)^2) = 0, \qquad (7)$$

where σ_e is the von Mises stress, σ_m the mean stress, $\bar{\sigma}$ the tensile flow stress and f^* is the current effective void volume fraction. q_1, q_2 and $q_3 = q_1^2$ are constants. The original Gurson model [12] is obtained by setting $q_1 = q_2 = q_3 = 1$, and $f^* = f$, where f denotes the current void volume fraction. Void coalescence is accounted for using the effective void volume fraction, f^*, from Tvergaard and Needleman [14] i.e.

$$f^*(f) = \begin{cases} f & \text{if } f \leq f_c, \\ f_c - \frac{f_F^* - f_c}{f_F - f_c}(f - f_c) & \text{if } f_c < f < f_F. \end{cases} \tag{8}$$

f_c is the critical void volume fraction at the start of void coalescence. f_F denotes the final failure void volume fraction, and is given by $f_F = 0.15 + 2f_0$, where where f_0 is the initial void volume fraction of f. The ultimate value where the macroscopic stress carrying capacity vanishes is defined as $f_F^* = 1/q_1$. The evolution of f in the second paper is purely dependent on growth of existing voids which is based on the law of conservation of mass, i.e.

$$df_{growth} = (1 - f)d\varepsilon_{kk}^p, \tag{9}$$

where df_{growth} denotes the incremental void volume growth of existing voids over an increment of load, and $d\varepsilon_{\mathbf{kk}}^{\mathbf{p}}$ is the incremental volumetric plastic strain. The summation rule over repeated indices must be applied.

1.3 Failure criteria

Three different failure criteria are applied in this thesis. The choice of failure criterion influences the results since they are based on different failure conditions.

In Paper 1 the traditional tangency criterion was employed. This criterion implies calculation and comparison of the applied crack driving force and the material crack growth resistance curve. The critical point is the tangency point defined as the instability point. If the applied J is denoted J_{app} and the material resistance J_R the following condition is met at the tangency point:

$$J_{app} = J_R \tag{10}$$

and

$$\frac{dJ_{app}}{da} = \frac{dJ_R}{da}. \tag{11}$$

This point must normally be solved by an iterative procedure. The corresponding strain at this level, ε_{crit}, has to be determined, and used in the subsequent probabilistic analyses. The criterion is used in existing standards, such as BS7910, [16]. The procedure is simple and suited to practical analyses, since the material resistance curve is obtained from simple experiments.

Another failure point is the maximum load criterion. This criterion is illustrated in Fig. 8(a). The highest point (i.e. maximum load) on the curve is

marked with the horizontal line with the corresponding critical strain ε_{critG} on the co-ordinate axis. The CTOD level at ε_{critG} on the crack driving force curve is seen in Fig. 8(b). Finally, we have a local failure criterion proposed by Østby

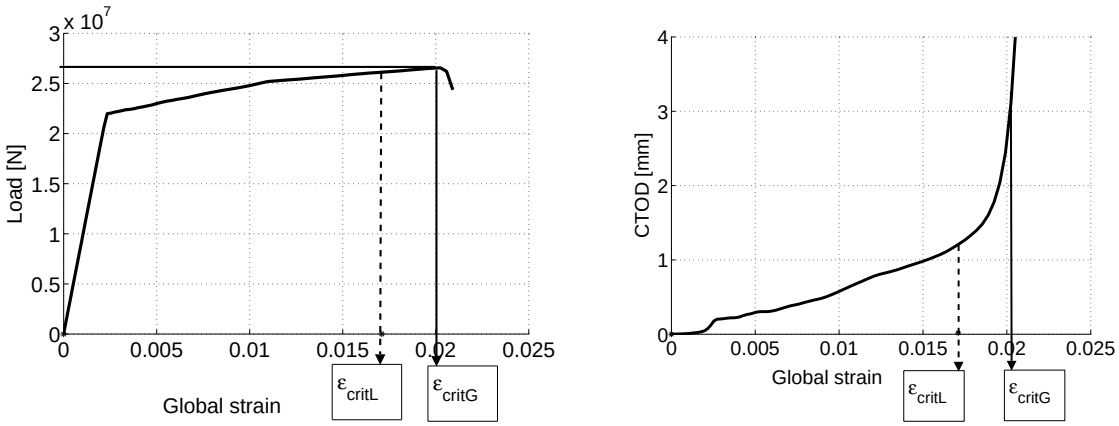

(a) (b)

Figure 8: The critical strain using the maximum load failure criterion (solid lines) and the local failure criterion (dotted line). (a) Load vs. strain curve, (b) CTOD vs. strain for a tensile loaded pipe. ε_{critL} and ε_{critG} denote the critical strain using the local and global criteria, respectively.

et al.[17]. This criterion predicts the CTOD at maximum load, δ_{max}, in the crack ligament. If L is the ligament height, and $\delta_{\Delta a=1mm}$ is the CTOD at 1mm crack growth, the local failure criterion is written as

$$\delta_{max} = (0.03L + \delta_{\Delta a=1mm} - 0.61)(-12.1(\frac{\sigma_{0.2}}{\sigma_{TS}})^2 + 18.9(\frac{\sigma_{0.2}}{\sigma_{TS}}) - 6.28). \qquad (12)$$

The critical strain, ε_{critL}, is depicted in Figs. 8(a) and 8(b) for comparison with the global maximum criterion.

1.4 Reliability analysis

The deterministic calculations provide the basis for the probabilistic fracture mechanics models. Such models can be used to describe the structural reliability of a pipe, given that we have statistical information for e.g. the load conditions, defect geometry, material, etc. This information is used to establish the limit state function, $G(\mathbf{x})$. If $f_{\mathbf{X}}(\mathbf{x})$ is the joint probability density function of $\mathbf{X}$, the

probability of failure integral can be written as:

$$p_f = \int_{G(\mathbf{X})\leq 0} f_{\mathbf{X}}(\mathbf{x})\mathbf{dx}. \tag{13}$$

The limit state function is:

$$G(\mathbf{X}) = \varepsilon_{\text{crit}}(\mathbf{X}_1) - \varepsilon_{\text{app}}(\mathbf{X}_2). \tag{14}$$

where $\mathbf{X} = (\mathbf{X}_1, \mathbf{X}_2)$ contains the basic variables. The capacity part is expressed as $\varepsilon_{\text{crit}}(\mathbf{X}_1)$ with the variables of interest represented in the vector $\mathbf{X}_1$. This could, as an example, be $\mathbf{X}_1 = (a, 2c)$ where a and 2c denote the crack depth and length, respectively, although it may in general contain other variables as well. $\varepsilon_{\text{app}}(\mathbf{X}_2)$ represents the load part of the limit state function, where $\mathbf{X}_2$ contains the load variables. $G(\mathbf{X}) \leq 0$ defines the region with structural failure, whereas $G(\mathbf{X}) > 0$ defines the safe region. The next part is to choose how Eq. (13) should be solved. Several methods exist, both analytical and numerical [18-20], and a brief overview of the methods applied in this thesis is given here.

First and second order reliability methods are popular methods to solve Eq. (13). Using these methods implies that the equation is solved by performing a mapping of the model with n correlated basic variables into uncorrelated, independent, standard, normal-distributed variables, followed by an approximation of the failure surface at the design point with a hyperplane or a parabolic surface. This mapping retains the statistical properties and can be applied for a general multi-dimensional problem with correlated statistical variables, see e.g. [21,22]. The mapping is illustrated in two dimensions in Fig. 9.

u-space is also denoted the Gaussian **u**-space where different possibilities exist for the limit state function. The first option is to use First Order Reliability Method (FORM). This method involves linearisation of the function around the design point using a first order Taylor expansion. The design point represents the highest probability of failure on the given failure surface, i.e the point on the failure surface closest to the co-ordinate origin. The distance from the origin to the design point is denoted as β, known as the safety index. Due to the rotational symmetry in the **u**-space the probability of failure can be determined from

$$p_f \approx \Phi(-\beta), \tag{15}$$

where Φ is the univariate standard normal integral. Another approximation is to apply a parabolic function around the design point, see Fig. 9. This solution technique is termed the second order reliability method (SORM) which may give a better estimate of the failure integral since the nonlinearity is better represented, e.g. Melchers [18] or Madsen et al. [19]. The FORM/SORM provide strictly asymptotic solutions, i.e., when the reliability index $\beta \longrightarrow \infty$. In cases with small β-values, the FORM/SORM yields robust solutions only for linear and

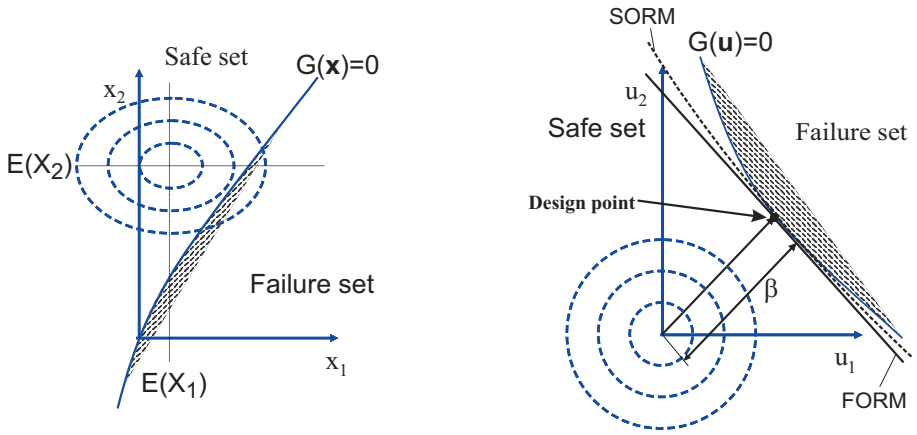

Figure 9: Illustration of mapping in two dimensions from the physical **x**-space to the Gaussian **u**-space.

quadratic failure functions. In this thesis the failure probabilities are expected to be small, i.e. we expect to have large β-values. Consequently, the FORM/SORM should be applicable.

Simple integration techniques are to use Monte Carlo simulations (MCS) or Monte Carlo simulations with importance sampling (MCSI). MCS involves random sampling of the basic variables to simulate a large number of cases to determine the proportion that fall into the unsafe region. This is checked by using an indicator function $I[G(\mathbf{x}) \leq 0]$ which returns 1 (true) if $G(\mathbf{x}) \leq 0$ or 0 (false) otherwise. From sample statistics the probability of failure integral can be estimated as:

$$p_f \approx \frac{1}{N} \sum_{j=1}^{N} I[G(\hat{\mathbf{x}}_j) \leq 0], \tag{16}$$

where $\hat{\mathbf{x}}_j$ denotes the vector j of random observations from the joint probability density function, $f_{\mathbf{X}}(\mathbf{x})$, and N is the total number of simulations.

This method may be criticized due to its poor efficiency. A large number of simulations is often necessary to obtain a probability of failure estimate with a high confidence level. If some a priori information from a problem is employed, the sampling region can be selected to improve the MCS method. This is the background for so-called importance sampling, see details in e.g. Melchers [18]. In this work the sampling has been done in the Gaussian **u**-space around the design point [23,35] using the ideas of Shinozuka [24].

Probabilistic ductile fracture mechanics

Probabilistic fracture mechanics models have been in use for several years. The main application, however, has been to brittle fracture problems. The most well-known statistical brittle fracture model is probably the one established by the French research group Beremin [25]. They proposed a local criterion for cleavage assuming that the probability of finding a micro-crack with a critical length is a function of the volume (locally around the crack tip) of the material involved. This method has later been applied in numerical models of fracture in the ductile-brittle transition regime, see e.g. Gao [26], based on the approach from Xia and Shih [27]. Attempts have also been made to establish probabilistic models for fracture assessment of welds, see e.g. [28,29].

However, a modern pipeline steel material is normally very ductile, and large plastic deformations may be allowed. The ductile fracture behaviour is fundamentally different from the brittle fracture, and new probabilistic ductile fracture mechanics models have to be established. The main contribution the past decade on this topic has been from S. Rahman and co-authors. Several approaches have been applied in their probabilistic models, e.g. analytical equations [30], FEM-models [31-33] and Galerkin meshless methods [34]. They have focused on thick-walled pipes, which are of main concern for e.g. the nuclear industry. This is different from the pipes investigated in this thesis, where the focus has been on thinner pipes with surface cracks and large deformations.

References

[1] T. Anderson, Fracture Mechanics, Fundamentals and Applications, 2nd Edition, CRC Press Inc., 1995.

[2] J. Hutchinson, Singular behavior at the end of a tensile crack in a hardening material, Journal of Mechanics and the Physics of Solids 16 (1968) 13–31.

[3] J. Rice, G. Rosengren, Plane strain deformation near a crack-tip in a power-law hardening material, Jornal of Mech Phy Solids 16 (1968) 1–12.

[4] R. McMeeking, Finite deformation analysis of crack-tip opening in elastic plastic materials and implications for fracture, Journal of the Mechanics and Physics of Solids 25 (1977) 357–381.

[5] J. Rice, A path independent integral and the approximate analysis of strain concentration by notches and cracks, Journal of Applied Mechanics 35 (1968) 379–386.

[6] J. Hutchinson, Fundamentals of the phenomenological theory of nonlinear fracture mechanics, Journal of Applied Mechanics 49 (1982) 103–197.

[7] C. Shih, Relationship between the J-integral and the crack opening displacement for stationary and extending cracks, Journal of the Mechanics and Physics of Solids 29 (1981) 305–326.

[8] C. Betegon, J.W. Hancock, Two-parameter characterization of elastic-plastic crack-tip fields, Journal of Applied Mechanics 50 (1991) 104–110.

[9] N.P. O'Dowd, C.F. Shih, Family of crack-tip fields characterized by a triaxiality parameter - I, Journal of the Mechanics and Physics of Solids 39 (1991) 989–1015.

[10] N.P. O'Dowd, C.F. Shih, Family of crack-tip fields characterized by a triaxiality parameter - II, Journal of the Mechanics and Physics of Solids 40 (1992) 939–963.

[11] B. Nyhus, E. Østby, H.O. Knagenhjelm, S. Black, P.A. Røstadsand, Fracture Control - Offshore Pipelines, Experimental studies on the effect of crack asymmetric geometries on the ductile tearing resistance, Proceedings 24th International Conference on Offshore Mechanics and Arctic Engineering (2005) OMAE2005-67532.

[12] A. Gurson, Continuum theory of ductile rupture by void nucleation and growth: Part 1 - yield critera and flow rules for porous ductile materials, Journal of Engng. Materials and technology 99 (1977) 2–15.

[13] V. Tvergaard, Influence of voids on shear band instabilities under plane strain conditions, Int. Journal of Fracture 17 (1981) 389–407.

[14] V. Tvergaard, A. Needleman, Analyses of the cup-cone fracture in a round tensile bar,, Acta Metallurgica 32 (1984) 157–169.

[15] A. Sandvik, E. Østby, C. Thaulow, Probabilistic fracture assessment of surface cracked pipes using strain-based approach, Engineering Fracture Mechanics 73 (2006) 1491–1509.

[16] BSI, Guide on methods for assessing the acceptability of flaws in metallic structures, BS 7910, British Standards Institution (2000).

[17] E. Østby, E. Torselletti, E. Levold, A strain-based approach to fracture assessment of pipelines, FITNET 2006 Conference, Paper no. 35, 17-19th of May 2006, Amsterdam, The Netherlands.

[18] R. Melchers, Structural reliability analysis and prediction, 2nd Edition, John Wiley & Sons, 1999.

[19] H. Madsen, S. Krenk, N. Lind, Methods of structural safety, Prentice Hall, 1986.

[20] P. Thoft-Christensen, M. Baker, Structural Reliability Theory and its Applications, 1st Edition, Springer-Verlag, Berlin, Germany, 1982.

[21] M. Hohenbichler, R. Rackwitz, Nonnormal dependent vectores in structural reliability, Journal of Engineering Mechanics Division 107 (1981) 1127–1238.

[22] M. Rosenblatt, Remarks on a multivariate transformation, The Annals of Mathematical Statistics 23 (1952) 470–472.

[23] DNV, Proban theory, Sesam user manual, Det Norske Veritas (2002).

[24] M. Shinozuka, Basic analysis of structural safety, Journal of Structural Engineering 109(3) (1983) 721–740.

[25] F. Beremin, A local criterion for cleavage fracture of a nuclear pressure vessel steel, Metallurgical Transactions 14A (1983) 2277–2287.

[26] X. Gao, Numerical modeling of crack growth in ductile-brittle transition regime, PhD-thesis, Brown University, 1998.

[27] L. Xia, C. Shih, Ductile crack growth-III. transition to cleavage fracture incorporating statistics., Journal of the mechanics and physics of solids 44 (1996) 603–639.

[28] M. Hauge, A probabilistic approach to fracture mechanics assessment of structural steel weldments, Doktoringeniør thesis, The Norwegian Institute of Technology, Division of Materials and Processes (1990).

[29] J. Tronskar, M. Mannan, M. Lai, G. Sigurdsson, K. Halsen, Crack tip constraint correction applied to probabilistic fracture mechanics analyses of floating production, storage and off-loading vessels, Engineering Fracture Mechanics 70 (11) (2003) 1415–1446.

[30] S. Rahman, Probabilistic elastic-plastic fracture analysis of circumferentially cracked pipes with finite-length surface flaws, Nuclear Engineering and Design 195 (2000) 239–260.

[31] S. Rahman, A stochastic model for elastic-plastic fracture analysis of circumferential through-wall-cracked pipes subject to bending, Engineering Fracture Mechanics 52 (2) (1995) 265–288.

[32] S. Rahman, Probabilistic fracture analysis of cracked pipes with circumferential flaws, International Journal of Pressure Vessels and Piping 70 (1997) 223–236.

[33] S. Rahman, J. Kim, Probabilistic fracture mechanics for nonlinear structures, International Journal of Pressure Vessels and Piping 78 (2001) 261–269.

[34] S. Rahman, B. Rao, An element-free galerkin method for probabilistic mechanics and reliability, International Journal of Solids and Structures 38 (2001) 9313–9330.

Probabilistic fracture assessment of surface cracked pipes using strain-based approach*

Andreas Sandvik, Erling Østby, and Christian Thaulow

Abstract

Simplified strain-based fracture mechanics equations, established for external surface cracked pipelines subjected to an external bending load, are presented and used in probabilistic assessment of a pipeline girth weld. The model takes into account several parameters, such as variation in crack depth, crack length, internal pressure and material hardening. The critical strain from ductile tearing in the cracked pipeline is found by using the tangency criterion. The reliability problem is solved using first and second order reliability methods for different pipe dimensions and load levels.

*Published in Engineering Fracture Mechanics, Vol. 73, pp. 1491-1509, 2006.

1 Nomenclature

t	pipe wall thickness
D	outer pipe wall diameter
ϕ	angle at the circumference of the pipe
$\sigma_0, \sigma_{0.2}$	stress at the proportional limit, stress at 0.2% plastic strain
σ_i, σ_{TS}	flow stress, tensile strength
σ_e, σ_m	von Mises, mean stress
$\bar{\sigma}$, σ_h	flow stress, hoop stress
n	hardening exponent
E	Young's modulus
ν	Poisson ratio
$CTOD$	crack tip opening displacement
ε	nominal uniaxial strain
ε_0, ε_p	strain at the proportional limit, plastic strain
ε_{lay}, ε_{app}, ε_{crit}	strain due to laying, strain input to the limit state equation, critical strain (capacity)
$\varepsilon_s, \varepsilon_d$	strain due to external static and dynamic load (load part)
C	initial slope on the driving force curve where Region 2 starts
p_f	probability of failure
$\mathbf{X}$	n-dimensional random vector
$\mathbf{x}$	realizations of $\mathbf{X}$
$f_{\mathbf{X}}(\mathbf{x})$	joint probability density function of $\mathbf{X}$
$F_{\mathbf{X}}(\mathbf{x})$	joint probability function
X_i	i-th random variable in x-space
$\mathbf{U}$	n-dimensional random vector in $\mathbf{u}$-space
$\mathbf{u}$	realizations of $\mathbf{U}$
U_i	i-th uncorrelated standard normal random variable
$G(\mathbf{x}), G(\mathbf{u})$	limit state functions in $\mathbf{x}$ and $\mathbf{u}$-space
Φ	univariate standard normal integral
β	safety index
$\alpha, \alpha_i, \alpha_{ii}, \alpha_{ij}$	polynom coefficients
f	current void volume fraction
f_0	initial void volume fraction
f^*	effective void volume fraction
f_U^*	the ultimate value where the microscopic stress carrying capacity vanish
q_1, q_2, q_3	constants in the Gurson yield function

2 Introduction

Offshore pipelines are an effective long-distance transportation method for oil and gas. Many new offshore development projects are in ultra-deep water depths with reservoirs and pipelines exposed to higher pressures and temperatures than in earlier projects. This requires better pipeline material utilization in addition to robust and reliable design guidelines.

In particular there are three conditions in which large plastic deformations may occur in the pipeline. During laying the pipeline may be exposed to large curvatures with corresponding large deformations. Further, considerable deformations may occur under operational conditions such as free-spans due to irregular seabed topography or lateral buckling due to temperature variations. Today the tensile side often limits the allowable load/deformation. In DNV-OS-

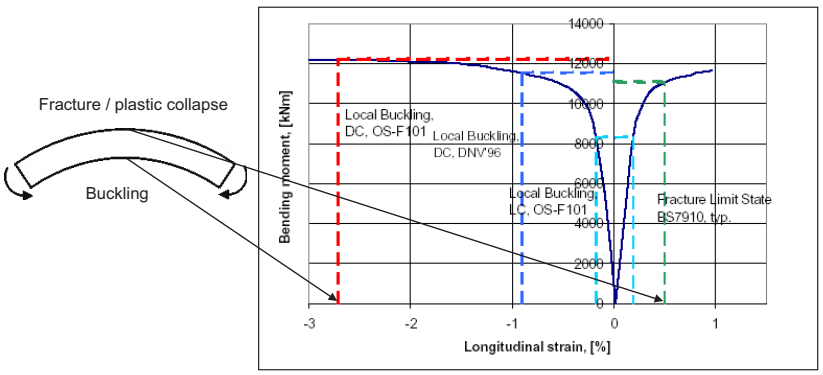

Figure 1: The difference in allowed strain on the compression and tension side in a pressurized pipeline according to different standards.

F101 [1] the local buckling criteria for a pipe with internal pressure limit the longitudinal compression strain to about 2 %, Fig. 1. In comparison, existing procedures for fracture assessment limit the tensile strain to about 0.3-0.5 % and therefore limit the utilisation of the given design. It is believed that existing fracture assessment methods may be overly conservative in addition to not fully accounting for the effects of internal pressure. As a result, new calculation strategies should enable qualification of higher tensile strains in pipelines during both laying and operation.

In fracture assessment the calculated driving force equations are important. Existing procedures, such as BS7910 [2] and R6 [3], do in general assume load-controlled approaches. This means that the stress (i.e. load) is used as input to

the analyses. To take into account the appearance of a defect in a structure (e.g. in a pipeline girth weld), the so-called reference stress is calculated. The choice of formula in the reference stress calculation will influence the results significantly. A common approach for fracture assessment of pipelines with circumferential cracks is to determine the reference stress by the method of Kastner et al. [4]. A potential problem with load-controlled methods has been their weakness in situations with large plastic deformations. The stress distribution in the structure is established from the applied load, and the corresponding strain distribution is obtained by the material's stress-strain relation. Since we now are considering the inelastic region, a small change in the stress level may result in a significant change in the strain level. Reference stress method using the Kastner solution applied to pipelines with circumferential surface defects are shown to be very conservative for long cracks and un-conservative for short cracks, Thaulow et al. [6].

Another method is to make use of displacement-controlled calculations, where the strain is determined from a given displacement and the corresponding stress is established through the material stress-strain relation. Evaluations performed with this strategy are called strain-based assessments. If the pipeline is subjected to an external load resulting in a load-controlled or a mixed load/displacement-controlled situation the strain-based methods may still be applicable in conjunction with appropriate safety factors, see Bratfos [7]. The same paper gives theory and basis for strain-based design.

It is believed that a strain-based design will enable a more reliable and precise fracture assessment when global plastic deformations occur in the pipeline. With this background the crack driving force equation applied in this paper is strain-based. A defect appears in the cross-section of a pipeline girth weld as shown in Fig. 2. The weld defects are assumed to be constant-depth (a) surface cracks with finite lengths ($2c$). This is reasonable since such defects may appear from welding. Further, an assumption is made that a defect can appear at an arbitrary position in the circumferential direction. The equations are developed for tension loads in addition to biaxial loading due to internal pressure. Further, it is assumed that the cross-section remains circular throughout the deformation and that there is no ovality or diameter expansion. Realistic dimensional parameters for offshore pipelines are considered in the examples.

Traditionally, the main focus in probabilistic fracture assessment has been brittle fracture, e.g. [8-11] and fatigue [12]. To the authors' knowledge, only minor research has been made on probabilistic fracture assessment of ductile steel materials. The main contribution on this topic seems to be from Rahman with colleagues, who have investigated the probability of failure in steel pipes with either circumferential constant-depth surface cracks or through-thickness cracks using simplified equations and Finite Element Method (FEM) calculations. In [13] and [14] Rahman established J solutions for through-wall cracked pipes subjected to pure bending loads by use of so-called influence functions established from FEM calculations. These functions are used in the

probabilistic computations together with various failure criteria and loads. Furthermore, Rahman and Brust [15] established another method for simplified computation of the J-integral for an internal, circumferential, constant-depth and finite-length surface crack, subjected to bending loads. In these methods they applied classical beam theory and deformation theory of plasticity. Additionally, they used a power-law idealisation of both the stress-strain curve and the crack-growth resistance curve. In the simulation of system compliance due to the presence of a crack, they applied a pipe with reduced thickness. This methodology was used by Rahman in e.g. [16] in a probabilistic fracture mechanic model. The model enabled closed form estimates for a range of deformation levels. However, the accuracy of the solutions for shallow cracks has not been verified. Other papers using similar methods may be found, for example Francis and Rahman [17], Rahman et al. [18], or Foxen and Rahman [19].

In Section 3, we present some basic structural reliability theory on how to solve the probability integral. In Section 4, the new probabilistic fracture mechanics model is presented, including details about how it was developed. The critical strain term is established, which is applied as the resistance term in the limit state equation. The calculation procedure and its implementation in the probabilistic software, Proban [20], are explained. In Section 4.2, the statistical input and preprocessing prior to the probabilistic calculations are presented. In Section 5 the results from the probabilistic ductile fracture analyses are presented and discussed.

3 Structural reliability - establishment of the probability of failure

In order to perform probabilistic fracture assessment we establish probabilistic calculations based on traditional structural reliability methods. The objective is to find the probability of failure from the multi-dimensional integral

$$p_f(G(\mathbf{X}) \leq 0) = \int_{G(\mathbf{x})\leq 0} f_{\mathbf{X}}(\mathbf{x}) d\mathbf{x}, \tag{1}$$

where $f_{\mathbf{X}}(\mathbf{x})$ is the joint density function and $\mathbf{X} = (X_1, ..., X_n)$ is an n-dimensional vector that represents the basic variables, i.e. the load and resistance variables. X_i denotes the i-th random variable represented by a statistical distribution. $G(\mathbf{X})$ is a general form of the limit state function, also called the performance function. It may be linear or non-linear and is a function of the load and resistance variables. $G(\mathbf{X}) > 0$ defines an outcome in the safe region, whereas $G(\mathbf{X}) \leq 0$ identifies the failure region. Finally, $G(\mathbf{X}) = 0$ defines the failure surface. The limit state equation used in this paper is presented in

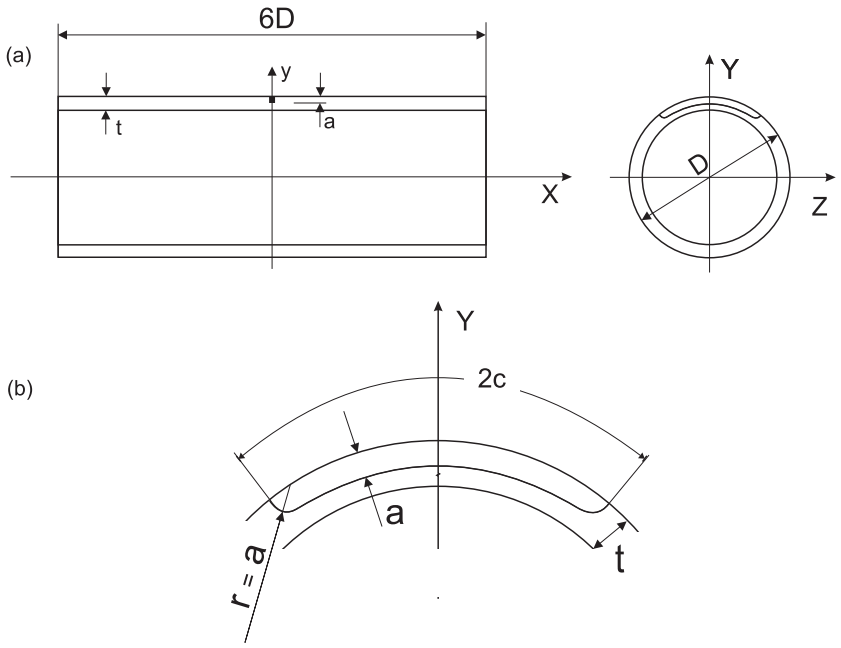

Figure 2: (a) The pipe geometry with an external circumferential constant-depth surface flaw. (b) Details of the canoe type defect with arc length, $2c$, depth, a, and end radius, r, equal to the crack depth, a.

Section 4.

Different solution strategies are available in solving the integral in Equation (1), including both analytical and numerical methods, [21-23]. A widely used, and simple, numerical integration technique is Monte Carlo Simulation (MCS) with or without sampling techniques. Details about such methods may be found in e.g. Melchers [23].

However, the main focus in this article is on transformation methods. The idea is to solve Equation (1) by performing a mapping of the probabilistic model with n correlated basic variables into uncorrelated, independent, standard, normally-distributed variables, followed by an approximation of the failure surface at the design point with a hyperplane or a parabolic surface. This mapping retains the statistical properties of the probabilistic model.

For a general, multi-dimensional problem with correlated variables represented with different statistical distributions, Hohenbichler and Rackwitz [24] proposed to use the established Rosenblatt transformation technique [25], to obtain uncorrelated, independent, standard, normally-distributed variables. This is a stepwise mapping technique requiring a known joint probability function $F_{\mathbf{X}}(\mathbf{x})$

in addition to conditional distributions. Consider n basic variables, which may be correlated, defined in the **x**-space as $\mathbf{X} = (X_1, X_2, ..., X_n)$. The uncorrelated standard normal variables are represented in **u**-space with uncertainty variables $\mathbf{U} = (U_1, U_2, ..., U_n)$. Hence, the variable transformation may be written as:

$$\begin{aligned} u_1 &= \Phi^{-1}(F(x_1)) \\ u_2 &= \Phi^{-1}(F(x_2 \mid x_1)) \\ &\cdot \\ &\cdot \\ u_n &= \Phi^{-1}(F(x_n \mid x_1, x_2, ..., x_{n-1})). \end{aligned}$$

where the conditional cumulative distribution is given by

$$F_n(x_n \mid x_1, ..., x_{n-1}) = \frac{\int_{-\infty}^{x_n} f_{\mathbf{X}_n}(x_1, ..., x_{n-1}, t)dt}{f_{\mathbf{X}_{n-1}}(x_1, ..., x_{n-1})}. \tag{2}$$

Further, we transform the limit state function into the **u**-space, i.e.

$$G(\mathbf{x}) \rightarrow G(\mathbf{u}) \tag{3}$$

The limit state function can, for example, be linearized using a first order Taylor expansion. This technique is known as the First Order Reliability Method (FORM). The linearization is made around the design point, which is the point on the failure surface closest to the co-ordinate origin in the Gaussian **u**-space. This distance is denoted β and is known as the safety index. In Fig. 3 this is illustrated in a 2D situation for simplicity. β represents the highest probability of failure on the given failure surface. Hence, the probability of failure can be established by using the relation

$$p_f = \Phi(-\beta), \tag{4}$$

where Φ is the univariate standard normal integral.

We use the general non-linear optimization constraint procedure solver called Sequential Quadratic Programming (SQP) optimizer [26] for determination of the design point.

As indicated in Fig. 3 there also exists a Second Order Reliability Method (SORM). Here, the failure surface is approximated by a parabolic function at the design point and a better approximation of p_f may be obtained when having large curvatures on the failure surfaces where FORM may produce inaccurate results. Theory about SORM may be found in e.g. Madsen et al. [21] or Melchers [23].

4 The probabilistic fracture mechanics model

The limit state equation, as defined in Equation (1), is expressed as

$$G(\mathbf{X}) = \varepsilon_{\text{crit}}(\mathbf{X}_1) - \varepsilon_{\text{app}}(\mathbf{X}_2). \tag{5}$$

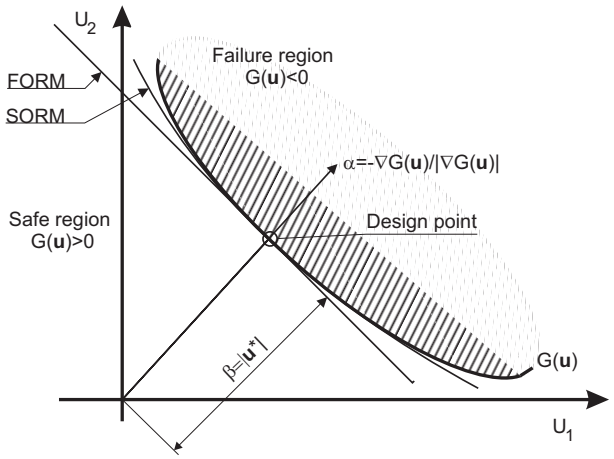

Figure 3: Approximation of the failure surface about the design point, i.e. the point of maximum likelihood, in the **u**-space where u_1 and u_2 are uncertainty variables.

The basic variables are included in $\mathbf{X} = (\mathbf{X}_1, \mathbf{X}_2)$. Furthermore, the resistance part (capacity) is represented by $\varepsilon_{\text{crit}}(\mathbf{X}_1)$ with the variables represented in the vector $\mathbf{X}_1$. Similarly, the load part is expressed as $\varepsilon_{\text{app}}(\mathbf{X}_2)$, where $\mathbf{X}_2$ contains the variables on the load side. There is in general assumed to be no correlation between the resistance and the load variables. However, it should be noted that in the present case the resistance function consists of both statistical and deterministic variables.

The problem was solved using the general purpose probabilistic analysis program, Proban [20]. The critical strain was calculated in an external Fortran subroutine using the driving force equation and the tangency criterion. The basic variables involved in the problem were given as input to Proban as distributions or deterministic values. Subsequently, the ε_{crit}-value was calculated. In this way, several pointwise solutions were obtained enabling a numerical representation of the limit state surface. This enabled a subsequent FORM/SORM solution with a corresponding estimate of the probability of failure.

4.1 The strain-based simplified fracture mechanics equation

The basic idea of the simplified strain-based driving force equations is presented in Østby et al. [27] and Østby [28]. In the following, the equations are based

on three dimensional (3D) FEM-analyses using Abaqus [29] with solid elements and Link$_{pipe}$ using linespring elements based on the ideas of Rice and Levy [30] and Parks and White [31]. A thorough examination of the numerical aspects and implementation of the linespring element into the Link$_{pipe}$ software is given in [32-34].

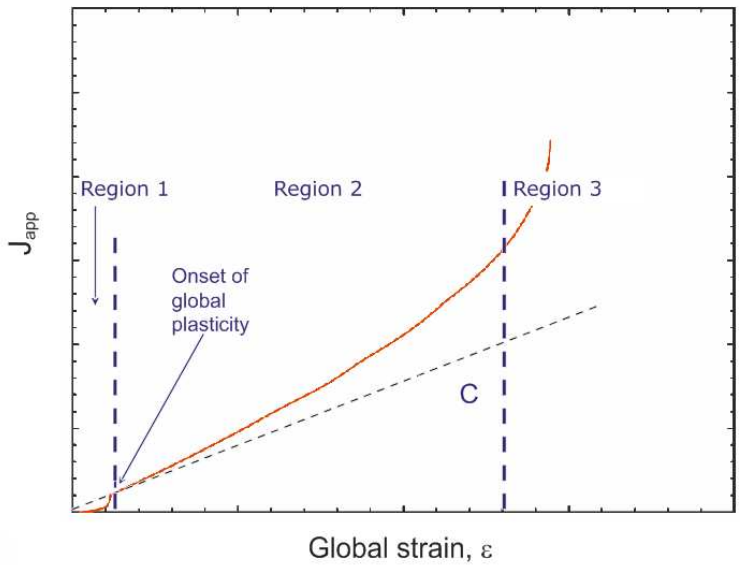

Figure 4: Characteristics of the driving force curve with the initial slope where the global plastic region starts.

The general concept is to express the relationship between the applied J, J_{app}, and the global strain, ε, in a surface cracked pipe. J_{app} is here the so-called far field J that is not influenced by the local crack tip conditions. First, it is assumed that global elastic deformation, shown as Region 1 in Fig. 4, is of minor interest. This is reasonable since we are interested in the fracture mechanisms with global plastic deformations, as shown in Region 2 and Region 3 in Fig. 4. C is defined as the initial slope that characterizes the crack driving force curve where Region 2 starts. This region is characterized by plasticity development through the whole pipe wall thickness. There is a tendency that the curve has a slight upward curvature. This is due to the necking of the crack ligament as significant plastic strains develop. Furthermore, Region 3 defines the collapse region with rapid increase of J. In this region the J increases rapidly since the collapse develops in the crack ligament. More details of the local deformation levels in the pipe due to external load may be found in [5,27].

The strain on the abscissa axis is global strain, which means that the strain is not influenced by local deformations. It was found that this was ensured if the strain was extracted one pipe diameter in the lengthwise direction away from the crack in the FEM analyses, [5,27].

All the derivations were done with a material following an isotropic power law hardening, namely

$$\sigma_i = \sigma_0 \left(1 + \frac{\varepsilon_p}{\varepsilon_0}\right)^n, \tag{6}$$

where σ_i is the flow stress, σ_0 is the stress at the proportional limit, ε_p is the plastic strain and n the hardening exponent. Next, $\varepsilon_0 = \sigma_0/E$, is the strain at the proportional limit, and E is the Young's modulus. If $\sigma < \sigma_0$ the material behaviour is linear elastic. It should be noted that the material hardening in this paper is obtained as $\sigma_{0.2}/\sigma_{TS}$, which is convenient in engineering application. σ_{TS} is defined as the tensile strength at $\varepsilon = n$ and $\sigma_{0.2}$ is the yield stress at 0.2 % plastic strain.

The parameterised driving force equation is in the form

$$J_{app} = tm\sigma_{0.2} \int_0^{\varepsilon} f g d\varepsilon, \tag{7}$$

where f, g, and m are functions presented in the following and t is the pipe wall thickness. As seen, the expression is integrated with respect to the global strain, ε, from zero to the desired strain value. m is a function merely dependent on the material hardening, and is defined as

$$m = 3.87 - 2.64\left(\sigma_{0.2}/\sigma_{TS}\right). \tag{8}$$

Details about this function are found in Appendix A. Next, f takes into account the crack depth and crack length, i.e.

$$f\left(\frac{a}{t}, \frac{2c}{\pi D}\right) = A_2 \left(\frac{a}{t}\right)^2 + A_1 \left(\frac{a}{t}\right) + A_0, \tag{9}$$

where a is defined as the current crack depth, D is the pipe diameter, and $2c$ is the crack length, all depicted in Fig. 1. The parameters, A_i, are expressed as

$$\begin{aligned} A_0 &= 183.43\left(\frac{2c}{\pi D}\right)^2 - 27.32\left(\frac{2c}{\pi D}\right) + 0.5507, \\ A_1 &= -2078\left(\frac{2c}{\pi D}\right)^2 + 191.56\left(\frac{2c}{\pi D}\right) + 2.577, \text{ and} \\ A_2 &= 4238.2\left(\frac{2c}{\pi D}\right)^2 + 339.32\left(\frac{2c}{\pi D}\right) - 16.4. \end{aligned}$$

The effect of crack depth and crack length variation on the calculated J_{app} is shown in Fig. 5 and Fig. 6, respectively. It should be noted that the curves in

Fig. 5 to Fig. 8 are from ductile tearing calculations using the $J - J_R$ relation referred to in Section 4.2. J_R follows the power law function

$$J_R = b_1(\Delta a)^{b_2}, \tag{10}$$

where Δa defines the ductile crack growth and b_1 and b_2 are constants. In the following deterministic curves with $b_1 = 852$ and $b_2 = 0.52$, which are representative values for X65 steel, Table 1, are used in the figures in this section.

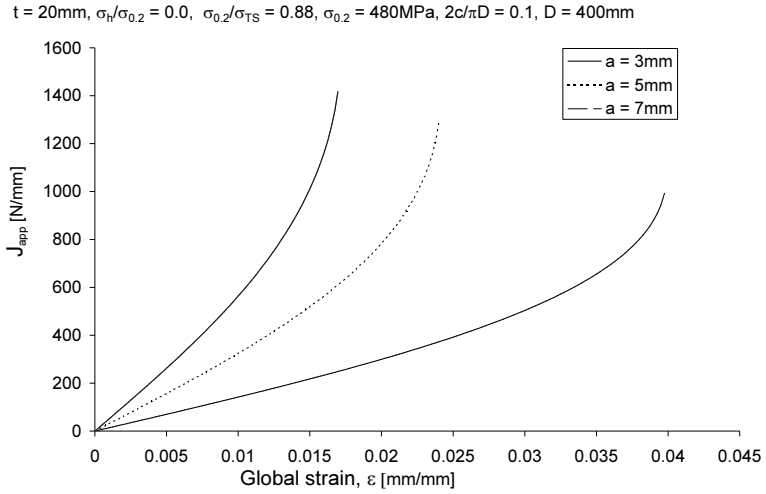

Figure 5: The evolution of applied J against global strain, for different a/t ratios.

The effect of material hardening has been included by two approximations dependent on the relative crack depth and the relative crack length. Consequently, the function g when $a/t \leq 0.25$ is

$$g\left(\frac{a}{t}, \frac{2c}{\pi D}, \frac{\sigma_{0.2}}{\sigma_{TS}}\right) = 1 + h\left(\frac{\sigma_{0.2}}{\sigma_{TS}}\right)\left(\frac{2c}{\pi D}\right)\left(\frac{a}{t} - 0.1\right). \tag{11}$$

On the other hand, if $a/t > 0.25$ then

$$g\left(\frac{a}{t}, \frac{2c}{\pi D}, \frac{\sigma_{0.2}}{\sigma_{TS}}\right) = 1 + h\left(\frac{\sigma_{0.2}}{\sigma_{TS}}\right)\left(\frac{2c}{\pi D}\right)0.15. \tag{12}$$

As observed, these expressions for g depend on the function h. This function gives a direct expression for the material hardening:

$$h\left(\frac{\sigma_{0.2}}{\sigma_{TS}}\right) = 2310.5\left(\frac{\sigma_{0.2}}{\sigma_{TS}}\right)^2 - 3765.2\left(\frac{\sigma_{0.2}}{\sigma_{TS}}\right) + 1524. \tag{13}$$

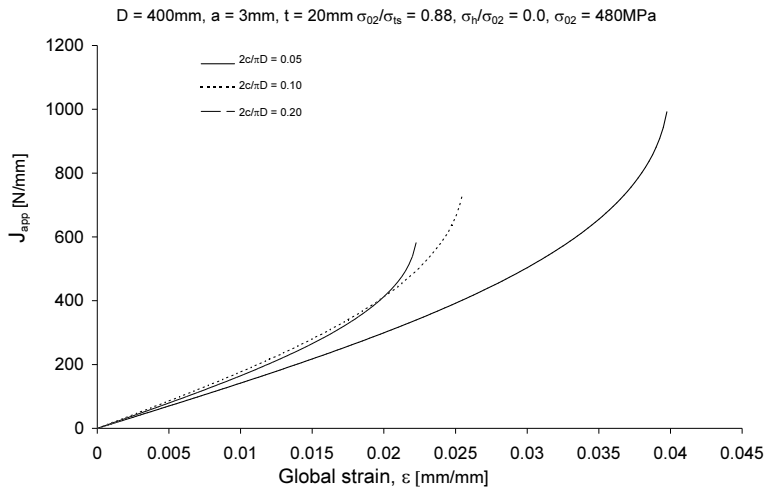

Figure 6: The evolution of applied J against global strain for various crack lengths, $2c$.

In Fig. 7 the effect of various hardening levels is depicted. As seen in this range, no significant difference is observed. However, it should be noted that the hardening effect increases with deeper cracks. The equations given so far have been fitted for the case where $D/t = 20$. To make the equation applicable for several D/t-ratios the following transformation has been shown to give reasonably good results:

$$2c/\pi D \rightarrow (2c/\pi D)(D/t)/20. \tag{14}$$

The background for this transformation is that for longer crack lengths, FE simulations show that the slope of the driving force curve saturates, and become virtually independent of 2c. When considering different D/t ratios the crack length at which this saturation occurs is closely related to the absolute length of the crack. Thus, the transformation proposed in Equation 14 relates other D/t ratios to the case with $D/t = 20$ through the value of $2c$.

Finally, the biaxial loading due to internal pressure is taken into account by adjusting the effective pipe wall thickness as a function of the hoop stress to yield stress ratio, while the crack ligament height is kept constant. When assuming a von Mises yield surface, this will lead to an increase in the effective relative crack depth in case of internal overpressure in the pipe. σ_h is defined as the hoop

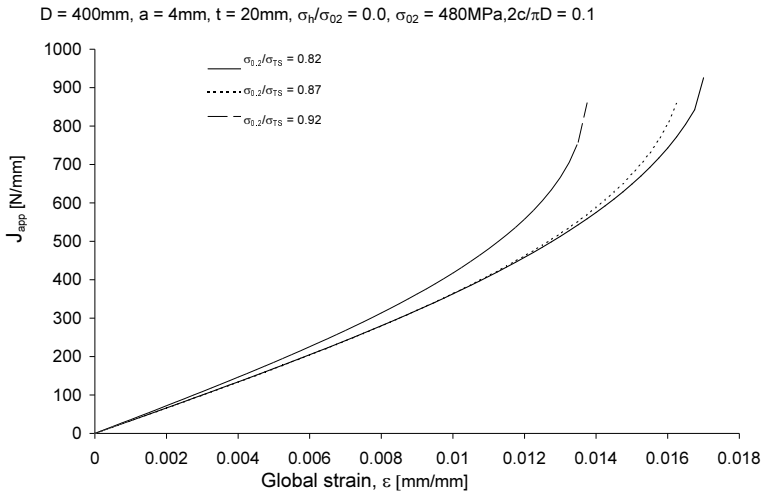

Figure 7: The evolution of J_{app} against global strain from the simplified driving force equation, for various material hardening levels.

stress, and for $\sigma_h/\sigma_{0.2} \leq 0.5$ we have:

$$\left(\frac{a}{t}\right)_{eff} = \frac{k-1}{k} + \frac{a}{kt}, \tag{15}$$

where

$$k = \left(1 - \frac{\sigma_h}{\sigma_{0.2}} + \left(\frac{\sigma_h}{\sigma_{0.2}}\right)^2\right)^{-1/2}.$$

In the case where $\sigma_h/\sigma_{0.2} > 0.5$ the effect of the internal pressure saturates and the relative crack depth is set to

$$\left(\frac{a}{t}\right)_{eff} = 0.134 + \frac{a}{1.15t}. \tag{16}$$

Further discussion about the effect of internal pressure may be found in [28]. The significant effect of variation of the internal pressure is shown in Fig. 8.

Equation (7) now has the expressions needed to calculate the relation between the global strain and the applied J. The equations have been established within the following window of parameters:

- Pipe wall thickness, [mm]: $15 \leq t \leq 35$

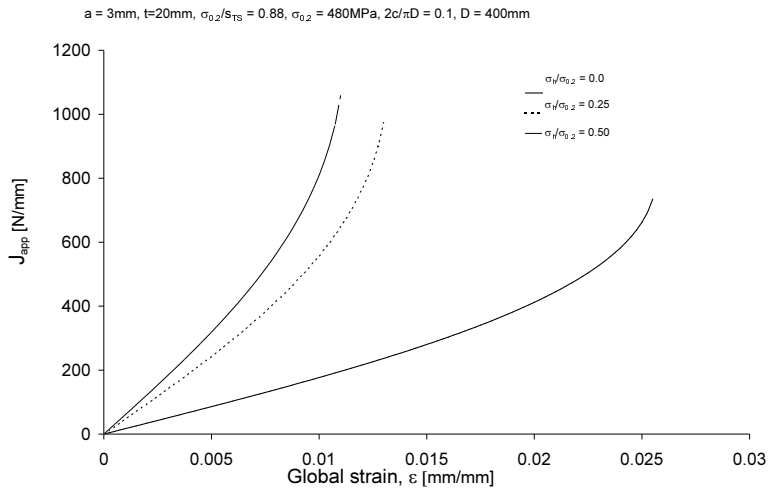

Figure 8: The effect of variation of internal pressure, $\sigma_h/\sigma_{0.2}$, on the evolution of J_{app} against global strain.

- Diameter to thickness ratio: $20 \leq D/t \leq 40$
- Relative crack depth: $a/t \leq 0.35$
- Crack length [mm]: $2c \leq 300$
- Material hardening: $0.82 \leq \sigma_{0.2}/\sigma_{TS} \leq 0.93$

In this range the accuracy of the equation generally lies within $\pm 20\%$. This is significantly better, when compared to 3D FE simulations, than when using the Kastner solution [4] as input to calculation of the reference stress in the BS7910 [2] equations, Thaulow et al. [6].

4.2 Calculation of the critical strain - ε_{crit}

The complete history of the crack development (i.e. ductile tearing) due to loading may be expressed by J_{app} and the material resistance J_R. The material crack growth resistance increases as the crack is loaded, and the crack growth will remain stable as long as the crack driving energy is lower than the resistance. However, a critical point, named the tangency point or the instability point, is reached when the following condition is met:

$$J_{\text{app}} = J_R, \tag{17}$$

and

$$\frac{dJ_{\text{app}}}{da} = \frac{dJ_R}{da}. \tag{18}$$

Then, an incremental change in crack size results in instability and a subsequent unstable crack growth. Since this criterion is a nonlinear relation, (17) and (18) have to be solved by an iterative procedure. During this procedure the critical strain, ε_{crit}, which is defined as the strain level where ductile tearing instability occurs, is calculated.

The J-resistance curve follows the power law function:

$$J_R = X_j b_1 (\Delta a)^{b_2}, \tag{19}$$

where the variable X_j is chosen to represent the statistical variation in the material resistance curve with the relation $Z_j = \log X_j$. Representative data for X65 pipeline steel are found in Table 1.

4.2.1 Strain due to external loading, ε_{app}

The second term in the limit state equation is the load part, ε_{app}, which is the strain due to external loading. Two load cases are considered with 0.5 % and 1.0 % global strain. The load has two contributing parts, static and dynamic. [2] These are represented by normal distributions summed up to a "total" strain distribution with mean value of 0.5% in the first load case, and 1.0% in the second load case. These load cases are presented in the result section as "Load case 0.5% strain" and "Load case 1% strain", respectively. The static load contributes 85% and the dynamic 15% to the total distribution, and the density distributions are illustrated in Fig. 9 for the "Load case 0.5% strain" case. The mean values and covariances for the distributions are presented in Table 1.

4.2.2 Defect location, effective crack length and modified strain

A linear strain variation over the pipe cross-section is assumed as depicted in Fig. 10. The maximum strain acting on a specific defect is obtained from the cross-section and used as input to the equation. This assumption implies that the pipe is subjected to a uniform load equal to the maximum strain.

Only defects subjected to tension in the pipe cross-section are assumed to contribute to the probability of failure. Thus, the strain due to laying, ε_{app}, and the crack length, $2c$, have to be modified in the analyses, as described below.

The localization of the surface crack was determined from a stochastic sampling from the uniform distribution for ϕ (Table 1). Then the maximum strain acting on the defect was determined. If the defect location passed the top of the pipe (12 o'clock in the cross-section in Fig. 10) the maximum strain was set to

[2] By dynamic load we mean a load not resulting in inertial effects.

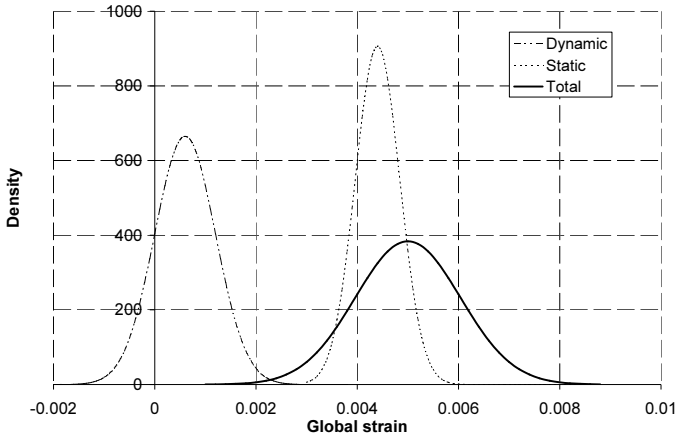

Figure 9: The static, dynamic, and total strain distributions. The given total mean strain is 0.5%.

Table 1: Input parameters and distributions used in the analyses.

Description		Distribution	$E[-]$	COV
J_R	Z_j	Normal	0	0.11*
J_R	b_1	-	852	-
J_R	b_2	-	0.52	-
Yield stress [MPa]	$\sigma_{0.2}$	-	480	-
Static load (strain)	ε_s	Normal	$4.4 \cdot 10^{-3}$	0.1
Dynamic load (strain)	ε_d	Normal	$6.0 \cdot 10^{-4}$	1
Angle	ϕ	Uniform	π	-
Pressure	$\sigma_h/\sigma_{0.2}$	-	$0, 0.5$	-

* *StD*

remain ε_{app}. Otherwise, the maximum tension strain acting on the defect was chosen (i.e. the defect end), and ε_{app} was modified to ε_{mod}.

Since the defect location is known, the effective crack length, $2c_{eff}$, was modified from the original crack length, $2c$ as illustrated in Fig. 10.

The output from this procedure was used to modify ε_{app} in the limit state equation, Equation (5), to ε_{mod}. Additionally, the effective crack length, $2c_{eff}$, was used as input to the crack driving force computation.

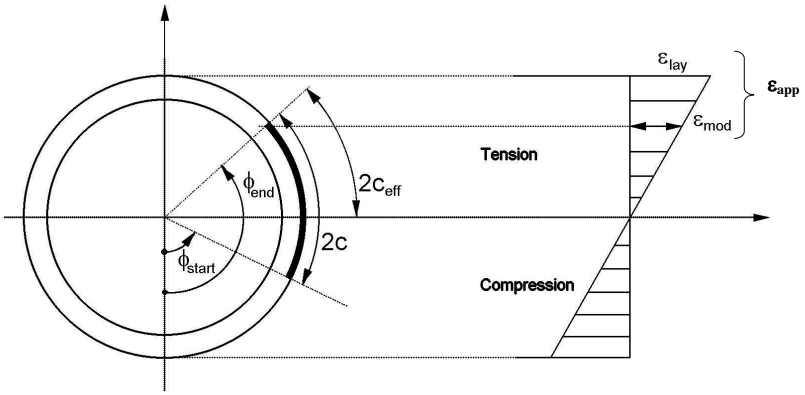

Figure 10: Illustration of a pipe cross-section with a surface defect. The adjusted effective crack length, $2c_{eff}$, and the modified strain, ε_{mod}, are depicted in addition to the strain due to laying, ε_{app}.

4.2.3 Defect distributions

In the second part of the result section we present results from complete probabilistic analysis using defect geometry distributions. The distributions are retrieved by performing a "virtual inspection" procedure.

The distributions are not necessarily realistic distributions, but definitely illustrative in realistic probabilistic analyses. The main idea was to reproduce the situation where we have a given girth weld inspected by Non Destructive Testing (NDT). Unfortunately, NDT tools do not necessarily discover all defects, due to the nature of defect location and occurrence in addition to measurement quality. Consequently, some defects pass the NDT control. To simulate this, we performed a conditional Monte Carlo Simulation procedure on a given initial crack defect distribution conditional on the probability of detection (PoD) distribution for a given NDT tool. Afterwards, the result was fitted to a lognormal distribution with values shown in Table 2. All the input variables used in the analyses with defect geometry represented with statistical distributions are found in Table 1 and Table 3.

The crack length distribution, $2c$, was established from a known two parameter Weibull distribution for aspect ratios between crack length and crack depth

conditional on defect depth, i.e.

$$f_{R|A}(r|a) = \frac{\beta_R(a)}{\alpha_R(a)} \left(\frac{r}{\alpha_R(a)} \right)^{\beta_R(a)-1} e^{-\left(\frac{r}{\alpha_R(a)}\right)^{\beta_R(a)}}. \quad (20)$$

The distribution parameters, namely the scale parameter, $\alpha_R(a)$, and the shape parameter, $\beta_R(a)$, are given as exponential functions in the form

$$\theta(a) = c_0 + c_1 e^{ac_2}, \quad (21)$$

where a is the current crack depth value and c_0, c_1 and c_2 are constants presented in Table 3. Furthermore, r is defined as the ratio between the crack length and crack depth, namely $r = 2c/a$. As a result, we now have the crack length distribution for a given crack depth.

Table 2: Distributions parameters and input variables in the second part of the analysis.

Description		Distribution	$E[-]$	COV
Depth [mm]	a	Lognormal	3.67	0.1
Diameter [mm]	D	-	$300 - 800$	-
Thickness [mm]	t	-	$7 - 40$	-
Pressure	$\sigma_h/\sigma_{0.2}$	-	$0, 0.5$	-

* *StD*

Table 3: Parameters in the conditional Weibull distribution in Equation 20.

Distribution parameters		Exponential function parameters		
		c_0	c_1	c_2
Scale	$\alpha_R(a)$	5.25	60.94	-0.425
Shape	$\beta_R(a)$	6.62	-5.83	-0.0084

5 Results

This section has three subsections. In the first subsection results from the analyses with load and J_R as uncertainty parameters is presented. Different runs are presented for several deterministic defect values to investigate the physical behaviour of the equations. In the next subsection we present results where the defect geometry is represented by statistical distributions. In the final part we compare results where FORM and SORM are used to investigate the solution accuracy in the calculations.

5.1 Analyses using deterministic defect values

In this part we present results illustrating the physical behaviour of the established probabilistic model. Only results for a pipe with diameter 600 mm and $t = 15$ mm are presented for two different load cases. The first load case has a mean value of 0.5% strain. This is referred as "Load case 0.5% strain" in the figures and text. The other load case, "Load case 1% strain" is similar, but here the mean strain value is 1%.

In Fig. 11 the probability of failure (PoF) is plotted against the defect depth (a) for the two load cases. A pronounced difference is seen between the different load cases for different crack geometries. Only crack depths from $2 - 4$ mm are plotted with constant crack lengths ($2c$) equal to 50 mm and 100 mm. This is chosen since the PoF is already as low as 10^{-8} for Load case 0.5% strain" with $2c = 50$ mm. The PoF is about equal to one in Load case 1% strain" with $2c = 100$ mm and $a = 4$ mm. Cracks with $a = 2$ mm and $a = 4$ mm represent $a/t = 0.13$ and $a/t = 0.27$, respectively. In "Load case 1% strain", the difference in PoF between the two relative crack depths is about five orders of magnitude. Additionally it is seen that increasing the crack length from 50 mm to 100 mm in the same load case increases the PoF by about three order of magnitude. Next, in Fig. 12, the influence from variation in pipe wall thickness is presented. The thickness is varied from 15 mm to 20 mm resulting in a diameter to thickness ratio of 40 and 30. As seen, there is a change of about three orders of magnitude when increasing the thickness from 15 mm to 20 mm for the "Load case 0.5% strain". However, for "Load case 1% strain" the change in PoF is less pronounced, i.e. from one to two orders of magnitude.

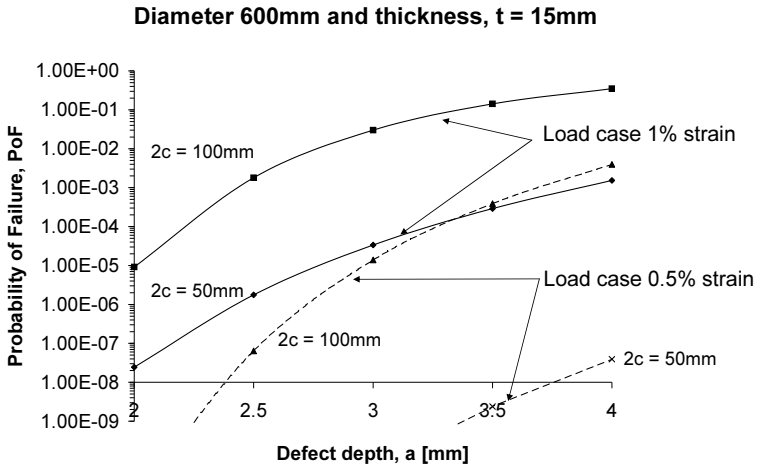

Figure 11: Influence of variation in crack lenght in the two different load cases.

Finally, in Fig. 13, we present results where the internal pressure is taken into account. Here, the crack length and thickness are kept constant. It is seen that the PoF is influenced significantly by introduction of internal pressure in particular for shallow crack depths. This is observed in both load cases, however for deeper cracks (i.e. increasing a) the difference is less pronounced.

5.2 Calculations using stochastic crack geometry values

In this section we present the results from the analyses where defect distributions are used as input.

Different load cases are presented, with and without internal pressure. Results from pipes with D/t ratios ranging from 20 to 40 are presented in Fig. 14. These results are from computations from "Load case 0.5% strain" and "Load case 1% strain", with and without internal pressure.

In "Load case 0.5% strain", the PoF is ranging from about 10^{-1} to 10^{-4}. The analysis results are from pipe diameters from 300 mm to 800 mm and is shown as an almost continuous line. Further, it is seen that the small diameter pipes have the highest PoF. We also observe that the PoF increases when the internal pressure is included. This increase is most pronounced for thick-walled pipes where the difference in PoF is about one order of magnitude.

In "Load case 1% strain" the PoF increases significantly when increasing the strain load, both for the pressurised and non-pressurised pipes, Fig. 14. The effect

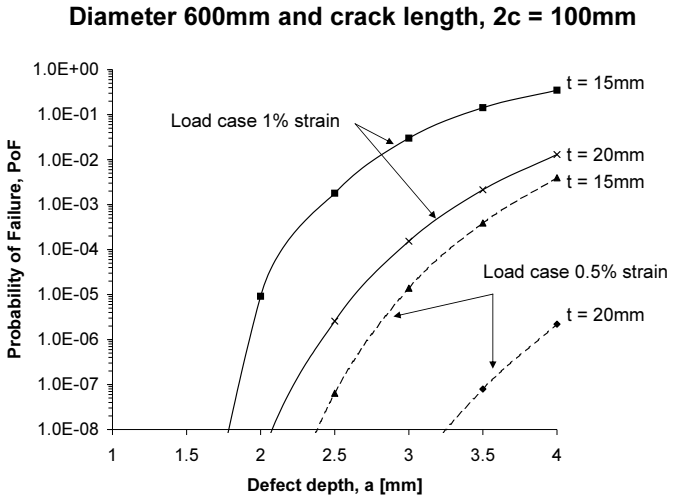

Figure 12: Influence of variation in pipe wall thickness on the probability of failure.

of internal pressure is most significant for the thickest pipes. For the thinner pipes, minor differences are seen in the PoF in the pressurised and un-pressurised cases. However, the differences show a monotonic increase as the pipe wall thickness increases. Another observation is that the un-pressurised results seem to be of the same order as the pressurised pipe in "Load case 0.5% strain".

5.3 Comparison of FORM and SORM calculations

In this section we compare results obtained by use of FORM and SORM. The results are presented in Fig. 15 and Fig. 16. The SORM results are given as broken lines and the FORM solutions are given as continuous lines. It is observed that both solution methods give results of the same order of magnitude. In "Load case 0.5 % strain" without pressure, Fig. 15, the FORM and SORM solutions are more or less coincident, at least for engineering purposes. In the pressurised case, the SORM solutions predict a lower PoF compared with FORM solutions. Minor differences are observed between the two solution methods in "Load case 1 % strain". However, the solutions are almost coincident in the pressurised load case and some difference is seen in the un-pressurised load case, see Fig. 16.

All the analysis results tend to have the SORM solution on the lower side of the FORM solutions. This means that the FORM results are on the conservative side.

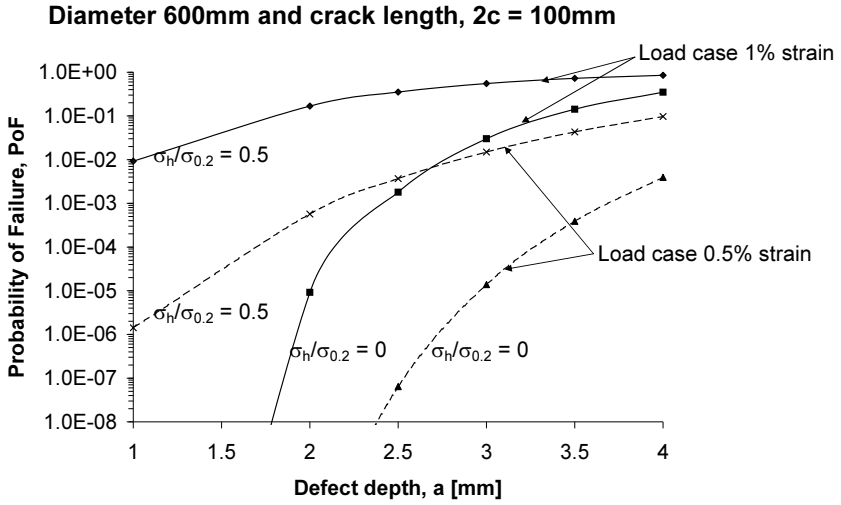

Figure 13: The influence on the probability of failure of internal pressure in the two different load cases.

Overall, for practical applications, we observe only minor differences between the FORM and SORM. Consequently, it appears that the FORM solution technique is sufficient to use in the further development of probabilistic models.

6 Concluding remarks and discussion

In this paper we have presented a methodology for probabilistic ductile tearing calculations for pipes with surface cracks, subjected to global plastic strains. The method involves the use of strain-based driving force equations and the tangency criterion to determination the global failure strain. This has served as a basis for a numerical representation of the failure surface with subsequent use of FORM and SORM solution methods. The model has been implemented in the Proban software for probabilistic calculations.

The simulations using a strain-based approach showed that an increase in the strain results in a corresponding increase in the probability of failure. When internal pressure was included a similar increase in PoF was observed. Additionally, the defect depth influenced the PoF significantly together with the defect length. Finally, it was shown that using the FORM solution gave robust and "conservative" results compared to SORM.

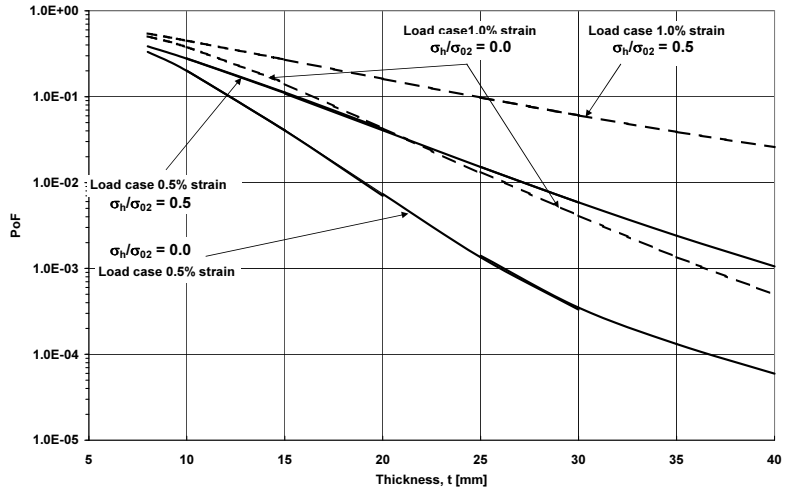

Figure 14: Results from the FORM calculations. 0.5 % and 1.0 % mean strain with and without internal pressure.

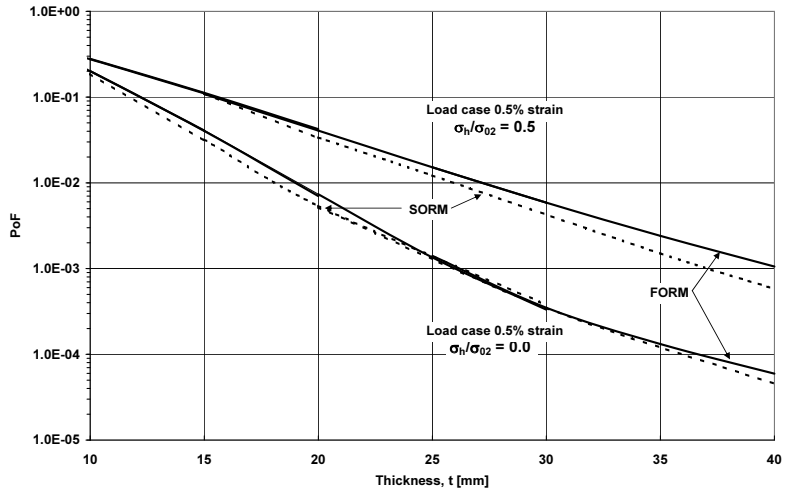

Figure 15: Comparison of FORM and SORM calculations in Load case 0.5 % strain with and without internal pressure.

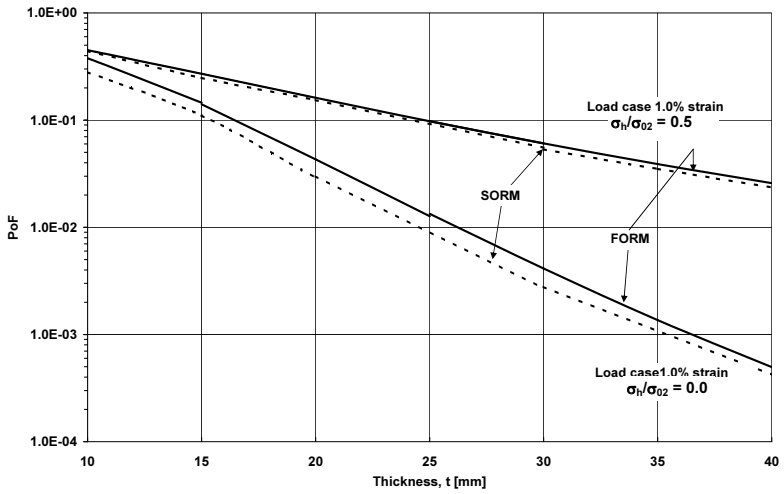

Figure 16: Comparison of FORM and SORM calculations in Load case 1 % strain with and without internal pressure.

Several topics should be subject to further investigation. The driving force equation has potential for further improvement. This is due to the fact that the accuracy of the equation is about ±20 %. Investigation in this respect is currently being carried out. However, for the time being it is worth to underline that the proposed driving force equations generally are more accurate than the reference stress method using the Kastner solution. Another aspect is to implement other physical effects like material mismatch and misalignment. A proposal for how this can be implemented is found in Østby [28].

The tangency criterion is used in the ductile tearing calculations to establish the critical global strain. The applicability of this criterion for cases with global ductile behaviour is uncertain, and possible alternative criteria determining the critical strain level should be investigated.

Another extension of the work is to analyse a complete pipeline system. Here we need to take into account the defect rate in addition to investigate the distinction between system effects, in which all defects are likely to be subjected to the same load, and cases where only a small part of the pipeline experiences extreme loads.

Additionally, the physical uncertainty of more parameters should be included in the model, like variation in yield stress, pipe thickness and internal pressure. A study on how the statistical uncertainty influences the PoF is also essential. One way to include this is to model the parameters, e.g. mean and variance, as

random values [23].

Aknowledgements

The authors want to express their gratitude to the Joint Industry Project Fracture Control - Offshore Pipelines with the following funding participants: Statoil, Hydro, BP, ENI Norge, Technip and the Research Council of Norway. Additionally, the advice and assistance from Dr. Gudfinnur Sigurdsson at Det Norske Veritas, Norway, and Professor Arvid Naess at NTNU, Norway, have been highly appreciated.

References

[1] DNV-OS-F101, Offshore standard, submarine pipeline system, Standard, Det Norske Veritas (2000).

[2] BSI, Guide on methods for assessing the acceptability of flaws in metallic structures, BS 7910, British Standards Institution (2000).

[3] Assessment of the integrity of structures containing defects - revision 4, R6, British Energy (2001).

[4] W. Kastner, E. Rohrich, W. Schmitt, R. Steinbuch, Critical crack sizes in ductile piping, International Journal of Pressure Vessels and Piping 9 (1981) 197–219.

[5] K. Jayadevan, E. Østby, C. Thaulow, Fracture response of pipelines subjected to large plastic deformation under tension, International Journal of Pressure Vessels and Piping 81 (2004) 771–783.

[6] C. Thaulow, B. Skallerud, K. Jayadevan, E. Berg, Fracture control offshore pipelines - advantages of using direct calculations in fracture assessments of pipelines, 24th International Conference on Offshore Mechanics and Arctic Engineering (2005).

[7] H. Bratfos, Use of strain-based - eca for the assessment of flaws in pipeline girth welds subjected to plastic deformations, Proceedings of the International Conference of Applications and Evaluations of High-Grade Linepipes in Hostile Environments (2002) 957–985.

[8] F. Beremin, A local criterion for cleavage fracture of a nuclear pressure vessel steel, Metallurgical Transactions 14A (1983) 2277–2287.

[9] S. Slatcher, A probabilistic model for lower-shelf fracture toughness - theory and application, Fatigue Fract. Engng. Mater. Struct. 9 (4) (1986) 275–289.

[10] M. Hauge, A probabilistic approach to fracture mechanics assessment of structural steel weldments, Doktoringeniør thesis, The Norwegian Institute of Technology, Division of Materials and Processes (1990).

[11] J. Tronskar, M. Mannan, M. Lai, G. Sigurdsson, K. Halsen, Crack tip constraint correction applied to probabilistic fracture mechanics analyses of floating production, storage and off-loading vessels, Engineering Fracture Mechanics 70 (11) (2003) 1415–1446.

[12] T. Bokalrud, A. Karlsen, A probabilistic fracture assessment of fatigue failure from weld defects in butt welds joints, Conf. on Fitness for Purpose Validation of Welded Constructions (1981).

[13] S. Rahman, A stochastic model for elastic-plastic fracture analysis of circumferential through-wall-cracked pipes subject to bending, Engineering Fracture Mechanics 52 (2) (1995) 265–288.

[14] S. Rahman, Probabilistic fracture analysis of cracked pipes with circumferential flaws, International Journal of Pressure Vessels and Piping 70 (1997) 223–236.

[15] S. Rahman, F. Brust, Approximate methods for predicting J-integral of a circumferentially surface-cracked pipe subject to bending, International Journal of Fracture 85 (1997) 111–130.

[16] S. Rahman, Probabilistic elastic-plastic fracture analysis of circumferentially cracked pipes with finite-length surface flaws, Nuclear Engineering and Design 195 (2000) 239–260.

[17] M. Francis, S. Rahman, Probabilistic analysis of weld cracks in center-cracked tension specimen, Computers and Structures 76 (2000) 483–506.

[18] S. Rahman, G. Chen, R. Firmature, Probabilistic analysis of off-center cracks in cylindrical structures, International Journal of Pressure Vessels and Piping 77 (2000) 3–16.

[19] J. Foxen, S. Rahman, Elastic-plastic analysis of small cracks in tubes under internal pressure and bending, Nuclear Engineering and Design 197 (2000) 75–87.

[20] DNV, Proban user guide, Sesam user manual, Det Norske Veritas (2002).

[21] H. Madsen, S. Krenk, N. Lind, Methods of structural safety, Prentice Hall, 1986.

[22] P. Thoft-Christensen, M. Baker, Structural Reliability Theory and its Applications, 1st Edition, Springer-Verlag, Berlin, Germany, 1982.

[23] R. Melchers, Structural reliability analysis and prediction, 2nd Edition, John Wiley & Sons, 1999.

[24] M. Hohenbichler, R. Rackwitz, Nonnormal dependent vectores in structural reliability, Journal of Engineering Mechanics Division 107 (1981) 1127–1238.

[25] M. Rosenblatt, Remarks on a multivariate transformation, The Annals of Mathematical Statistics 23 (1952) 470–472.

[26] DNV, Proban theory, Sesam user manual, Det Norske Veritas (2002).

[27] E. Østby, K. Jayadevan, C. Thaulow, Fracture response of pipelines subject to large deformations under bending, International Journal of Pressure Vessels and Piping (2004) (2004) 201–215.

[28] E. Østby, Fracture control offshore pipelines - new strain-based fracture mechanics equations including the effects of biaxial loading, mismatch, and misalignment, 24th International Conference on Offshore Mechanics and Arctic Engineering (2005).

[29] Abaqus User's Manual Version 6.4 (2003).

[30] J. Rice, N. Levy, The part through surface crack in an elastic plate, Journal of applied mechanics (1972) 185–194.

[31] D. Parks, C. White, Elastic plastic linespring finite element formulation, Computers and structures 104 (1982) 287–292.

[32] B. Skallerud, K. Holthe, B. Haugen, Thin shell and surface crack finite elements for simulation of combined failure modes, Computer methods in applied mechanics and engineering (2004) 2619–2640.

[33] K. Jayadevan, C. Thaulow, E. Østby, E. Berg, B. Skallerud, K. Holthe, B. Nyhus, Structural integrity of pipelines:T-stress by line-spring, Fatigue and Fracture of Engineering Materials and Structures 28 (2005) 467.

[34] C. Thaulow, K. R. Jayadevan, E. Østby, E. Berg, B. Skallerud, K. Holthe, B. Nyhus, Advances in computational procedures for the structural integrity of pipelines, International Conference on Advances in Structural Integrity (2004).

[35] C. Shih, Relationship between the J-integral and the crack opening displacement for stationary and extending cracks, Journal of the Mechanics and Physics of Solids 29 (1981) 305–326.

A Relationship between J and CTOD

The equations in this project is derived in parallel for CTOD (denoted δ) and J. As a result a conversion factor, m was found when the material follows the isotropic material hardening, Equation (8) as presented in Section 4.1. On a

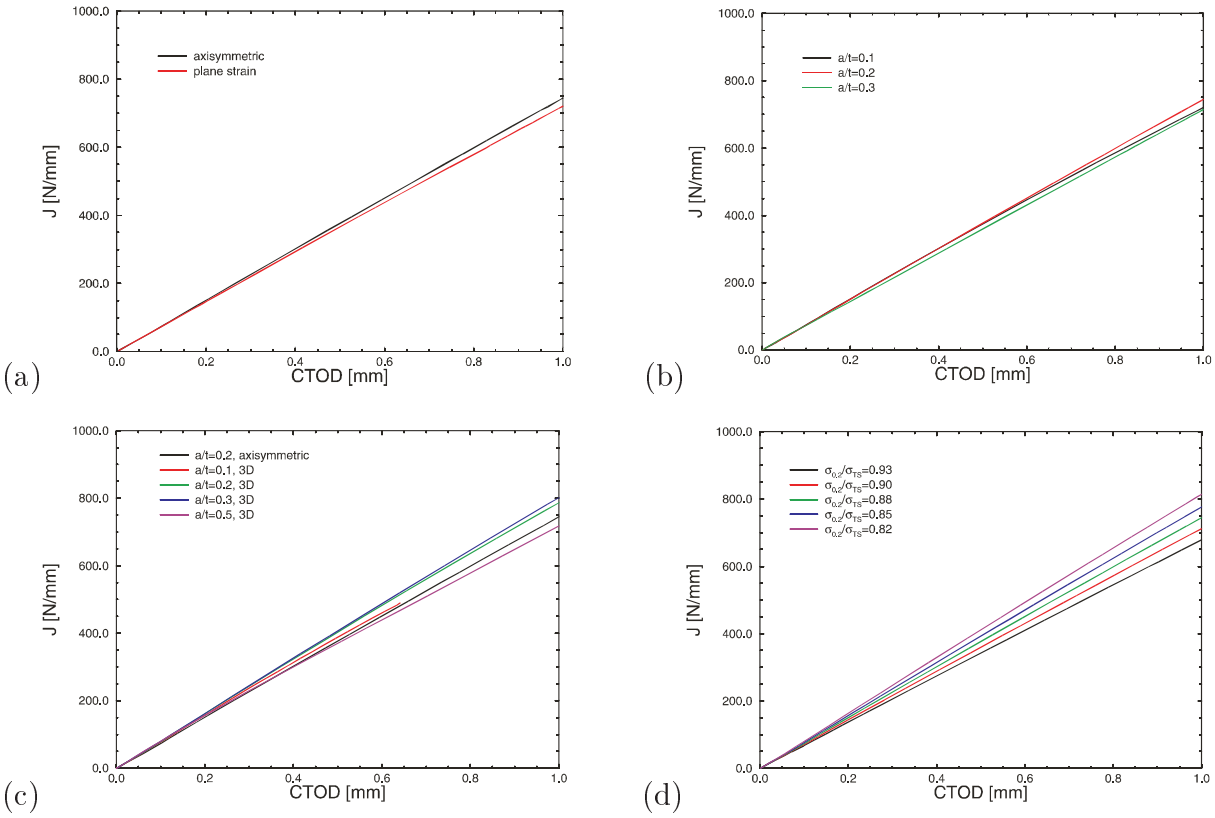

Figure 17: (a)The relationship between J and CTOD with the assumption of plain strain and axis-symmetric solutions, respectively. (b) The effect of the relative crack depth on the relationship between J and CTOD. (c) Comparison between the J-CTOD relationship from 2D analyses and 3D pipes with different crack depths. (d) The effect of the $\sigma_{0.2}/\sigma_{TS}$ ratio on the relationship between J and CTOD.

theoretical basis Shih [35] has shown that there is a direct link between J and CTOD, thus, they are equally valid parameters for expressing the crack driving force. The basic relation between the two parameters can be given as:

$$J = m\sigma_{0.2}\delta \tag{22}$$

where m is a constant that depends on the material properties and possibly the crack depth.

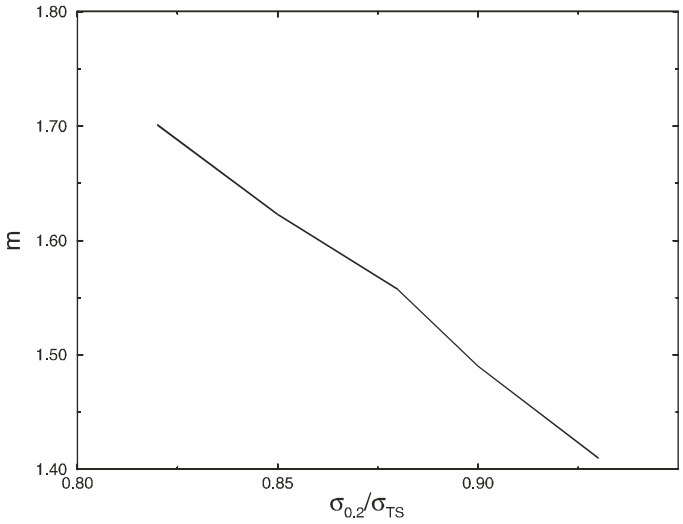

Figure 18: The factor m relating J and CTOD as a function of the $\sigma_{0.2}/\sigma_{TS}$ ratio.

In the results below the J-integral is calculated as the so-called far field J, to prevent break-down of the path independence at very small J values, as observed when calculating the J-integral close to the crack tip.

It can be shown that the yield stress (with fixed $\sigma_{0.2}/\sigma_{TS}$ ratio) had no effect on the driving force against the applied strain, when the driving force was expressed as the CTOD. In case of J this holds with one exception, the CTOD value must be multiplied by the ration between the two yield stresses, when going from one value to the other. This follows directly from Equation (22).

In Fig. 17 (a) the effect of relative crack depth on the relationship between J and CTOD is shown for an axisymmetric model. It can bee seen that there is a linear relationship between the J and the CTOD. Further, only a negligible effect of the relative crack depth is seen. Thus, the dependence of the relative crack depth can be discarded. In Fig. 17 (b) the axisymmetric model is compared with a model assuming plane strain condition. Also in this case we see that the two different models yield more or less the same relationship between J and CTOD. A comparison between the results from a 2D axis-symmetric simulations and different 3D simulations is shown in Fig. 17 (c). We see that there is some difference in the slope of the J-CTOD relation in the 3D simulations. However, the difference between the 2D axis-symmetric analysis and all the 3D analyses are not very significant (within 10%). Based on this it is proposed to use 2D simulations to establish the effect of the material properties on the relationship between J and CTOD.

Figure 17 (d) shows the effect of changing the $\sigma_{0.2}/\sigma_{TS}$ ratio on the relation between J and CTOD ($\sigma_{0.2} = 480N/mm^2$). From this figure we see that the slope, i.e. the m-factor in Equation 22, increases as the $\sigma_{0.2}/\sigma_{TS}$ ratio decreases

(or as the hardening of the material increases). This is in line with what was theoretically shown by Shih in [35]. To establish the dependency of the m-factor the following value has been calculated based on the results presented in Fig. 17 (d):

$$m = \frac{J_{\delta=1mm}}{\sigma_{0.2}} \tag{23}$$

where $J_{\delta=1mm}$ is the J value at 1mm. Fig. 18 shows the m-value value as a function of the $\sigma_{0.2}/\sigma_{TS}$ ratio calculated based on the results in Fig. 17 (d). As seen from Fig. 18 the m-value is quite close to a linear function of the $\sigma_{0.2}/\sigma_{TS}$ ratio. As a result, the following m-factor is used:

$$m\left(\sigma_{0.2}/\sigma_{TS}\right) = 3.87 - 2.64\left(\sigma_{0.2}/\sigma_{TS}\right). \tag{24}$$

A probabilistic fracture mechanics model including 3D ductile tearing of bi-axially loaded pipes with surface cracks*

Andreas Sandvik, Erling Østby, and Christian Thaulow

Abstract

This paper presents a probabilistic fracture mechanics model established from three dimensional FEM analyses of surface cracked pipes subjected to tension load in combination with internal pressure. The models are particularly interesting for offshore pipelines under operational conditions or during laying, where inelastic deformations may occur. In the numerical models the plastic deformations, including ductile tearing effects, are accounted for by use of the Gurson-Tvergaard-Needleman model. This model is calibrated to represent a typical X65 pipeline steel behaviour under ductile crack growth and collapse. Several parameters are taken into account, such as crack depth, crack length and material hardening. Another important topic is the examination of the influence of bi-axial loading due to internal pressure on capacity. From the results of the deterministic analyses a probabilistic fracture mechanics model is established using the response surface methodology. Two failure criteria are examined to represent the structural capacity. Based on the established model we illustrate the methodology by examples employing the two different failure criteria solved with first and second order reliability methods.

*Accepted for publication with minor revision in Engineering Fracture Mechanics

Nomenclature

t	pipe wall thickness
D	pipe wall diameter
ϕ	angle at the circumference of the pipe
$\sigma_0, \sigma_{0.2}$	stress at the proportional limit, stress at 0.2% plastic strain
σ_i, σ_{TS}	flow stress, tensile strength
σ_e, σ_m	von Mises stress, mean stress
σ_h	hoop stress
n	hardening exponent
E	Young's modulus
ν	Poisson ratio
$CTOD$	crack tip opening displacement
ε	nominal global longitudinal strain
ε_0, ε_p	strain at the proportional limit, plastic strain
ε_{lay}, ε_{app}	strain due to laying, strain input to the limit state equation
ε_{crit}, $\bar{\varepsilon}_{crit}$	critical strain (capacity), critical strain function
$\varepsilon_s, \varepsilon_d$	strain due to external static and dynamic load
p_f	probability of failure
$\mathbf{X}$	n-dimensional random vector
$\mathbf{x}$	realizations of $\mathbf{X}$
$f_{\mathbf{X}}(\mathbf{x})$	joint probability density function of $\mathbf{X}$
$F_{\mathbf{X}}(\mathbf{x})$	joint probability function
X_i	i-th random variable in x-space
$\mathbf{U}$	n-dimensional random vector in $\mathbf{u}$-space
$\mathbf{u}$	realizations of $\mathbf{U}$
U_i	i-th uncorrelated standard normal random variable
$G(\mathbf{x}), G(\mathbf{u})$	limit state functions in $\mathbf{x}$ and $\mathbf{u}$-space
Φ	univariate standard normal integral
β	safety index
$\alpha, \alpha_i, \alpha_{ii}, \alpha_{ij}$	polynomial coefficients
f_0, f, f^*	initial, current, and effective void volume fraction
$\dot{f}_{growth}$	change in void volume fraction due to void growth
f_F^*	the ultimate value where the microscopic stress carrying capacity vanishes
q_1, q_2, q_3	constants in the Gurson yield function

1 Introduction

Under installation and operational conditions of offshore pipelines it is of utmost importance to have calculation procedures to account for different failure modes, such as brittle and ductile fracture and buckling. Additionally, it is important to utilize the pipe capacity to enable a safe and cost effective design. In this paper we focus on steel pipe materials, such as $X65$, exposed to ductile fracture. In high grade pipeline steels fracture mechanics assessment is important due to the

high utilization of the material. Large plastic deformations may be allowed, and a defect positioned in an area with high tension load can result in catastrophic failure. Under operational conditions with internal pressure, the external loads may come from free-spans due to seabed topography or lateral snaking due to thermal loads. This means that the loading is often introduced as applied strain.

Presently, BS7910 [1] and R6 [2] are two examples of common fracture assessment procedures used in pipeline engineering. These procedures are mainly established for elastic global response and do not consider large plastic deformations. It has been shown that BS7910 [1] has restricted applicability where large longitudinal plastic deformations occur, Thaulow et al. [3]. In addition, the stress-based BS7910 procedure is not able to predict safe strain limits for high strain conditions accounting for internal pressure. Therefore, the emphasis in the Joint Industry Fracture Control-Offshore Pipelines project [4] is on large plastic deformations in pipelines and strain-based design. It is believed that a strain-based methodology has the potential to improve the physical prediction of the fracture mechanics response. Strain-based fracture mechanics equations, including the effects of biaxial loading, mismatch, and misalignment, have recently been presented, Østby [5]. These simplified equations are used to establish a strain-based design procedure for laying and operational conditions for offshore pipelines using the partial safety factor format as found in e.g. DNV-OS-F101 [6].

It is believed that probabilistic calculation for ductile materials is an area of increasing importance due to the trend of using high strength steels and utilizing the material to high strains. Probability analyses will give fundamental information about the reliability of the structural system of interest in addition to the sensitivity of the various parameters involved. In the past much focus has been on the probability of brittle fracture , e.g. [7-10], and fatigue[11]. Probabilistic models taking into account ductile tearing prior to cleavage fracture are also found, e.g. [12]. Ductile tearing analyses using 3D FEM are still not common. However, some results including ductile tearing effects in wide plates have been obtained, Chen and Lambert [13], who compared simulation results with pipe section experiments and illustrated the applicability of the solutions. Probabilistic calculations for ductile materials have mainly been contributed in the past decade by Rahman and various co-authors. Their main focus has been on pipes with through-wall or internal cracks on relatively thick-walled pipes using using FEM and analytical methods [14-18]. Ernst et al. have established structural reliability models for reeling processes [19,20]. The response surface technique has also been applied in probabilistic fracture assessment, Rahman et al. [21]. Foxen and Rahman [22] analysed small cracks in tubes under internal pressure and bending loads, where one of the observations was that for through-wall-thickness cracks the effect of internal pressure was significant for high-hardening pipe materials, and insignificant otherwise. However, none of these models is directly applicable for our purpose for highly ductile offshore pipelines. In Sandvik et

al. [23] a probablistic fracture mechanics model (PFM) of surface cracked pipes using a strain-based approach is presented. This PFM-model was based on semi-analytical strain based equations established by Østby [5]. These results showed that the combination of internal pressure with tension load gave a significant reduction of the pipe capacity compared with an un-pressurized pipe.

In this paper we present 3D FEM-models of pipes with external surface defects, including the effect of ductile tearing. The analysis results are used to establish response surfaces suitable for use in reliability analyses. The structure of the paper is as follows: In the first part we present the three dimensional deterministic FE-models. Pipe and defect geometry, material properties and the ductile tearing model are presented and explained. A separate result section comments the findings from the FE-simulations. The simulation results are then used to establish response surfaces in the proposed PFM-model [24,25], and this is presented in the second part. In the following section the proposed methodology is illustrated with examples where the probability of failure is determined using first and second order reliability methods (FORM and SORM). Finally, we present conclusions and suggestions for further work.

2 3D FE-models

Geometry

A sketch of the pipe geometry containing a constant depth surface defect is shown in Fig 1. The uniform crack depth, a, and crack length, $2c$, are depicted. The defect end has a radius equal to the defect depth. A single pipe diameter and thickness are used in all the analyses, but the defect geometry is varied, see Table 1. Three defect depths and three defect lengths are modelled, giving a total of nine defect geometries.

Element mesh

Due to loading and geometric conditions two-plane symmetry was applied in all the analyses such that only one quarter of the cylinder was modelled. The element mesh is a focused mesh with two levels. First, the local level represents the defect zone, where the element mesh size in the pipe's lengthwise direction is 0.1 mm around the crack front. This element size was fixed for all analyses due to the mesh dependent material parameter f_0. Details about this are found in the "Material" subsection. Second, a gradually coarser element mesh in the lengthwise and circumferential direction were applied using transition elements to minimize the model size. An element mesh of a pipe with a crack is shown in Fig. 2, and a more detailed view of a local mesh around the defect front in Fig. 3. Details on pre-processing of FE-models with surface cracked pipes are given in

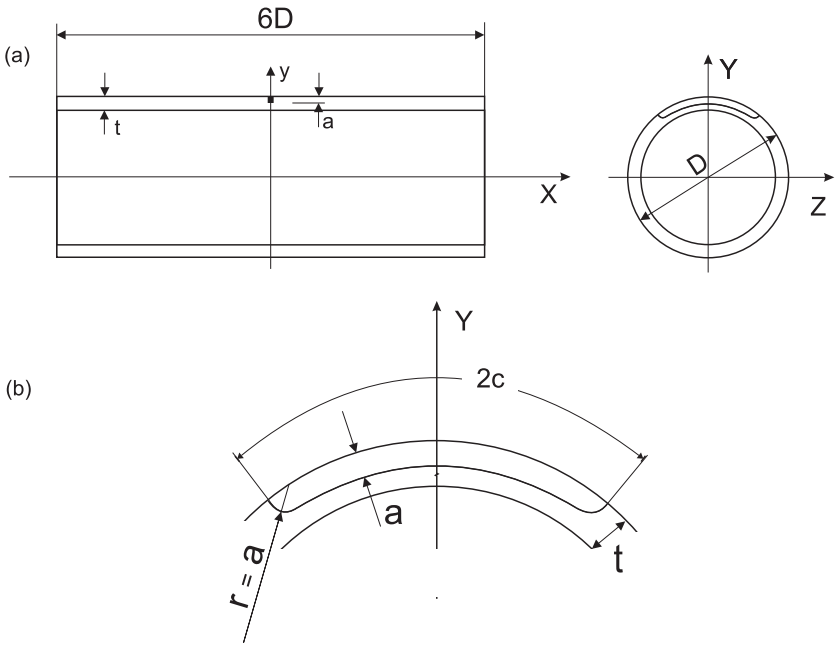

Figure 1: (a) Pipe geometry with an external circumferential constant-depth surface flaw. (b) Details of the constant depth surface defect with arc length, $2c$, depth, a, and end radius, r, equal to the crack depth, a.

Sandvik et al. [26].

In all the analyses the 8-node linear continuum element with reduced integration and hourglass control, C3D8R, [27] was applied. Due to variation in defect length in the different models there is some variation in the number of elements in the circumferential direction. Consequently, the element and node number range from 49299 elements and 58170 nodes to 65790 elements and 75816 nodes, for the models with the shortest (50 mm) and the longest (250 mm) cracks, respectively.

Loads and boundary conditions

Both the pressure load and tension load were successively applied using a smooth amplitude function [27] to ensure a quasi-static behaviour. The amplitude function has the property that the first and second derivatives are zero at both end points. If s denotes the amplitude, $\hat{t}$ the load step time, and the end points are given as $(\hat{t}_0, s_0) = (0, 0)$ and $(\hat{t}_1, s_1) = (1, 1)$ the amplitude function is expressed as:

$$s(\hat{t}) = \hat{t}^3(10 - 15\hat{t} + \hat{t}^2). \tag{1}$$

A satisfactory loading rate was found when 200000 increments were used for each load step. For the pressurized cases, loading due to internal pressure load was applied as a separate load step prior to the tension load. The uniform tension load was applied as a displacement at the un-cracked end of the pipe. Further, three different load levels for the internal pressure were analysed. Since internal pressure results in a biaxial load state, it is expressed through $\sigma_h/\sigma_{0.2}$, where σ_h is the hoop stress and $\sigma_{0.2}$ is the stress at 0.2 % plastic strain. Three load levels were analysed, $\sigma_h/\sigma_{0.2} = 0, 0.25$ and 0.5.

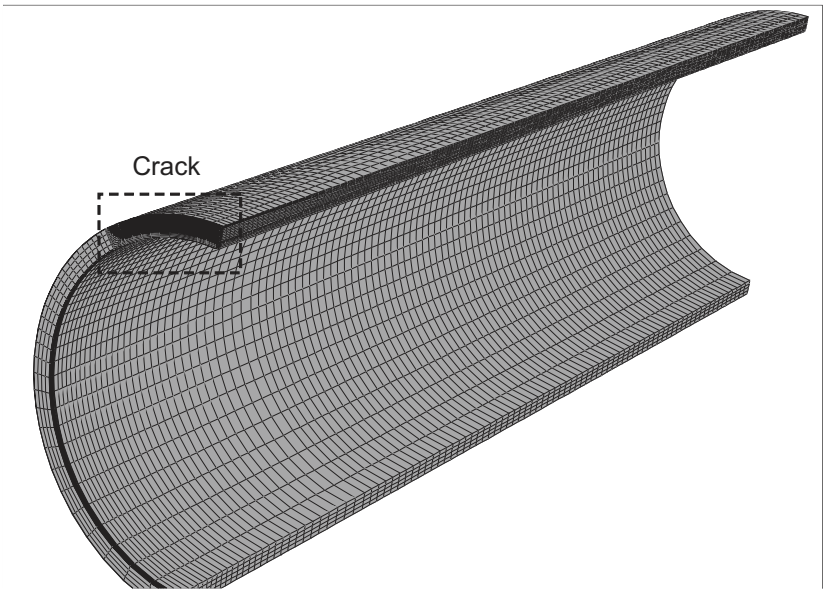

Figure 2: A typical FE-mesh of one quarter of a pipe containing a surface defect. The dotted frame marks the close-up view of the defect zone shown in Fig. 3.

Material

The material's plasticity behaviour was represented using an isotropic power law hardening relationship, i.e.

$$\sigma_i = \sigma_0 \left(1 + \frac{\varepsilon_p}{\varepsilon_0}\right)^n. \tag{2}$$

σ_0 is the stress at the proportional limit, σ_i is the flow stress, ε_p is the plastic strain and n the hardening exponent. Further, $\varepsilon_0 = \sigma_0/E$, is the strain at the proportional limit, and E is Young's modulus. If $\sigma < \sigma_0$ the material behaviour is linear elastic. In the analyses $\sigma_0 = 460$MPa, $E = 200$GPa and the Poisson ratio

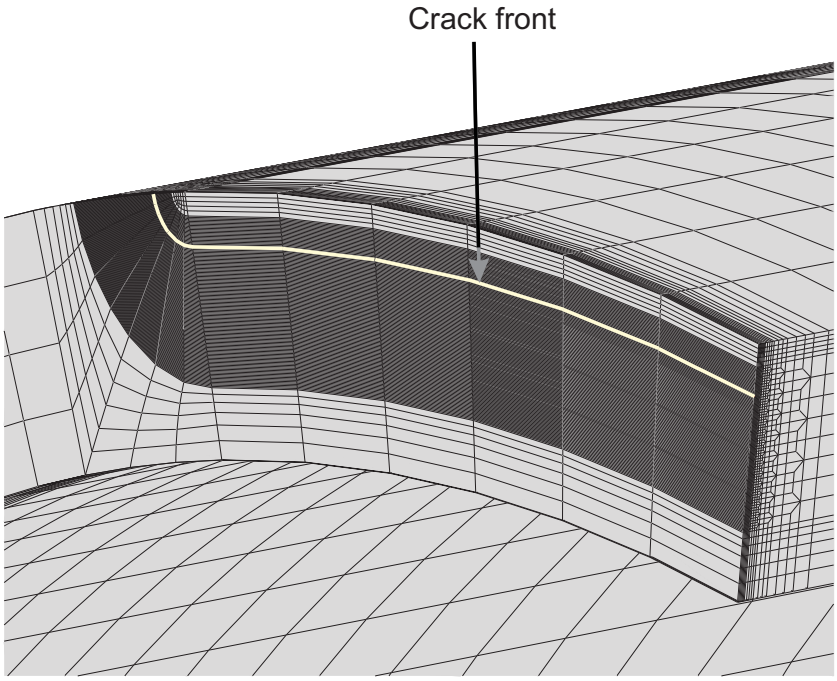

Figure 3: Close-up view of the defect zone where the smallest element size is 0.1 mm in the lengthwise direction.

was $\nu = 0.3$. Three different hardening levels were used in the models, namely $n = 0.05$, $n = 0.07$ and $n = 0.09$, see Table 1.

Ductile tearing effects were taken into account using the Gurson-Tvergaard-Needleman approximate yield model. This model was proposed by Gurson [28], and later modified [29,30]. The model simulates the microvoid nucleation, growth and coalescence, and assumes that the porous material behaves like a continuum where the plastic yield surface is adjusted dependent on the hydrostatic stress level and current void volume fraction. The yield condition is expressed as

$$g(\sigma_e, \sigma_m, \bar{\sigma}, f^*) = (\frac{\sigma_e}{\bar{\sigma}})^2 + 2q_1 f^* \cosh(\frac{3q_2\sigma_m}{2\bar{\sigma}}) - (1 + q_3(f^*)^2) = 0, \qquad (3)$$

where σ_e is the von Mises stress, σ_m the mean stress, $\bar{\sigma}$ the tensile flow stress and f^* is the current effective void volume fraction. $q_1 = 1.5$, $q_2 = 1.0$ and $q_3 = q_1^2$ are constants with values proposed by Tvergaard [29]. These constants improved the model considerably compared with the original model which predicted too high maximum loads. The original Gurson model [28] is obtained by setting $q_1 = q_2 = q_3 = 1$, and $f^* = f$, where f denotes the current void volume fraction. Void coalescence was taken into account using Tvergaard and Needleman's [30]

Table 1: Input parameters for the different FEM-models (9 runs per model).

Model	a mm	$2c$ mm	n	$\sigma_h/\sigma_{0.2}$	D mm	t mm
1	3	50	0.05, 0.07, and 0.09	0, 0.25, and 0.5	400	20
2	3	50	0.05, 0.07, and 0.09	0, 0.25, and 0.5	400	20
3	3	50	0.05, 0.07, and 0.09	0, 0.25, and 0.5	400	20
4	4	150	0.05, 0.07, and 0.09	0, 0.25, and 0.5	400	20
5	4	150	0.05, 0.07, and 0.09	0, 0.25, and 0.5	400	20
6	4	150	0.05, 0.07, and 0.09	0, 0.25, and 0.5	400	20
7	5	250	0.05, 0.07, and 0.09	0, 0.25, and 0.5	400	20
8	5	250	0.05, 0.07, and 0.09	0, 0.25, and 0.5	400	20
9	5	250	0.05, 0.07, and 0.09	0, 0.25, and 0.5	400	20

effective void volume fraction, f^*, i.e.

$$f^*(f) = \begin{cases} f & \text{if } f \leq f_c, \\ f_c - \frac{f_F^* - f_c}{f_F - f_c}(f - f_c) & \text{if } f_c < f < f_F. \end{cases} \tag{4}$$

f_c is the critical void volume fraction referring to start of void coalescence. $f_F = 0.15 + 2f_0$, where f_0 is the initial void volume fraction of f. f_F denotes the final failure void volume fraction. Since f_0 is element size dependent, it was fitted to represent a traditional $X65$ steel material, and the corresponding element size was fixed in all the analyses. It should be noted that a variation of f_0 implies a corresponding variation of the crack growth resistance curve. $f_F^* = 1/q_1$ is defined as the ultimate value at which the macroscopic stress carrying capacity vanishes. The ductile crack growth is simulated by removing elements successively as the crack grows, and an element is removed from the analysis when the element's material point reaches failure. The evolution of f in our analyses is purely dependent on growth of existing voids which is based on the law of conservation of mass, i.e.

$$df_{growth} = (1 - f)d\varepsilon_{kk}^p, \tag{5}$$

where df_{growth} denotes the incremental void volume growth of existing voids over an increment of load, and $d\varepsilon_{\mathbf{kk}}^{\mathbf{p}}$ is the incremental volumetric plastic strain.[2] The employed input data are listed in Table 2.

2.1 Solution method and solution quality

Abaqus Explicit [27] was applied in the solution of the 3D models. One reason for this is that it includes the failure effect in Eq. 4, which is not the case for Abaqus

[2]The summation rule over repeated indices must be applied.

Table 2: Material input to the FEM-models.

E	ν	σ_0	n	q_1	q_2	q_3	f_0	f_F	f_c
200[GPa]	0.3	460[MPa]	0.05, 0.07, 0.09	1.5	1.0	2.25	0.0002	0.1504	0.013

Standard. Explicit solvers were originally developed for dynamic scenarios where shock and mass effects played an important role. The solver is based on the principle of conservation of mass, momentum and energy, and theory and background information are found in Wilkins [31] and Belytschko et al. [32]. Further, quasi-static solutions are obtainable for several structural problems with use of explicit solvers as long as the dynamic effects are negligible [27,32].

To illustrate the solution quality of the explicit solution we have performed a comparison between an implicit and an explicit solution using Abaqus Standard and Abaqus Explicit, respectively. The implicit analyses are presented in Jajadevan et al. [33], who performed a detailed mesh sensitivity study for their models. The pipe diameter was $D = 400$ mm, and the pipe thickness, $t = 20$ mm. Two different defect geometries were investigated. The first model had a defect depth, $a = 2$ mm and a defect length which was 10 % of the outer circumference. The other model had $a = 4$ mm and defect length that was 20 % of the outer circumference. In the Abaqus Standard analyses 20-node 3D elements with reduced integration were used, with 0.25 mm element size around the crack tip in the lengthwise direction. However, 8 node constant stress elements with 0.1 mm element size in the lengthwise direction around the crack tip were applied in the explicit solutions. The pipes were subjected to a uniform tension load.

In order to compare the two solution methods the crack driving force curves obtained from the analyses are presented, i.e. the crack tip opening displacement (CTOD) is plotted against global axial strain. In Fig. 4 (a) crack driving force curves are presented for the case with stationary cracks. The curves are seen to almost coincide which means that the explicit solution matches the implicit solution. In Fig. 4 (b) another comparison is presented for the case with a deeper and longer crack. However, in this case the explicit solution includes ductile tearing, whereas the implicit results are from a stationary crack solution. The curves are seen to coincide until the ductile tearing starts in the explicit solution case. The ductile tearing results in a more rapid growth in CTOD.

From these results it is seen that the chosen loading rate for the explicit solutions, for the given load scenario, agrees well with the implicit solutions. Consequently, this loading rate is applied in the further work.

3 Results and discussion

In this section we present an extract of results from the 81 analyses performed. CTOD has been applied as the fracture parameter for characterization of ini-

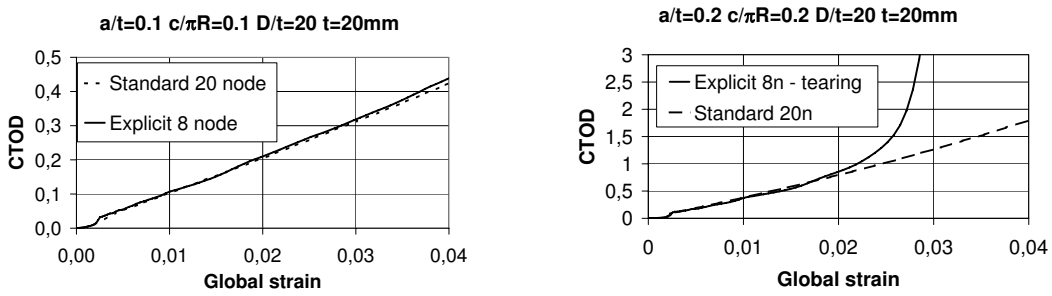

(a) (b)

Figure 4: Comparison of Abaqus Standard and Abaqus Explicit solutions for two different crack geometries with $D = 400$ mm and $t = 20$ mm. (a) $a/t = 0.1$ and $c/\pi R = 0.1$ and solutions without ductile tearing. (b) $a/t = 0.2$ and $c/\pi R = 0.2$ where the Standard solution is without and the Explicit solution is including ductile tearing.

tiation of ductile crack growth, stable crack growth and subsequent instability. CTOD and the J-integral are the most applicable fracture parameters describing ductile fracture behaviour according to Rice [34] and Hutchinson [35]. An equivalence between J and CTOD has been shown for both a stationary and a growing crack by Shih [36]. The results herein are presented as driving force curves, i.e. CTOD against global strain. The CTOD value was extracted from a fixed node in the symmetry plane two nodes above the initial crack front nodes. It was found that using this node the high plastic deformations around the crack tip were captured during the loading. Additionally, this node was used as the CTOD output node during the ductile crack growth. The global longitudinal strain was extracted 25 mm from the (un-cracked) tension loaded end. It has been validated that local deformation effects are avoided if the strain is extracted at least two pipe diameters in the lengthwise direction away from the crack [33,37].

In order to simplify the interpretation of the results we give a short explanation of general trends in the crack driving force curves. In Fig. 5 a characteristic driving force curve is plotted, and three different regions are indicated. Region 1 denotes the global elastic deformation and is of minor interest in this context, since we are interested in predicting fracture after global plastic deformation has occured, shown as Region 2 and Region 3. In Region 2 a relatively linear relationship between the CTOD and global strain. This region is characterized by plasticity development through the whole pipe wall thickness, and we also

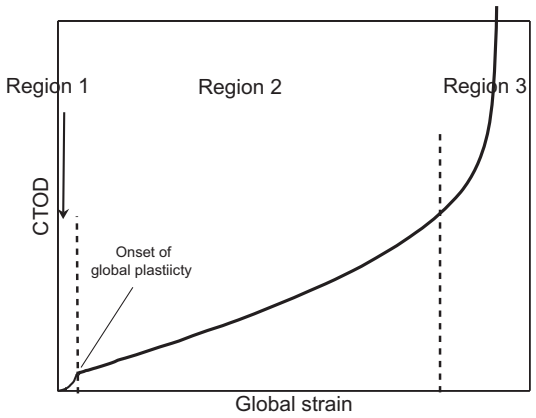

Figure 5: Three characteristic regions on the crack driving force curve.

observe a slight upward curvature of the curve. Region 3 defines the collapse region with rapid increase of CTOD where significant plastic deformations and ductile tearing develop in the crack ligament. Thus, the rapid crack growth leads to loss of strain capacity, shown as an almost vertical crack driving force curve, indicating a limit for the pipe's global strain capacity. More details of the local deformation levels in the pipe due to external load may be found in Jayadevan et al. [33]. In Figure 6(a), the CTOD is plotted against the global strain, for a surface cracked pipe with three crack depths, $a = 3$, 4, and 5 mm, crack length $2c = 50$ mm and $n = 0.05$. It is observed that the defect depth affects the crack driving force, the CTOD at a specific strain level is increasing as the defect depth increases. Similar trends are seen in Figs. 6(b)-6(c) with longer cracks, i.e. 150 and 250 mm. For the deepest and longest cracks the transition from Region 1 to 3 occurs directly. As a result a small change in the strain level causes a large increase in CTOD, even for low strain levels. Consequently, we observe approximately 75 % strain capacity reduction from the shallowest to the deepest defect. Similar trends are seen in Figs. 7(a)-7(c), but here the strain capacity is higher, as expected, due to the higher hardening, n=0.09. In Figs. 8(a)-8(c) the three crack depths are plotted with three different crack lengths for the case with $n = 0.07$. The crack length variation is also seen to affect the crack driving force. A large increase in the crack driving force is observed as the crack length is increased from 50 mm to 150 mm. Furthermore, the increase is most pronounced for the deepest cracks. The shortest crack has the lowest CTOD at a specific strain, and the 150 mm and 250 mm cracks are more or less coincident until Region 3 starts. This indicates that the crack length influence on the crack driving force curve saturates around this crack length level. Further,

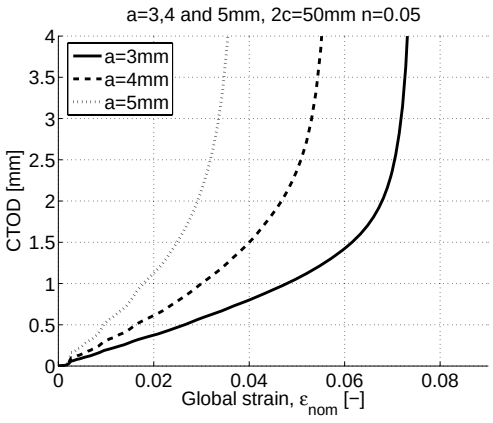

(a)

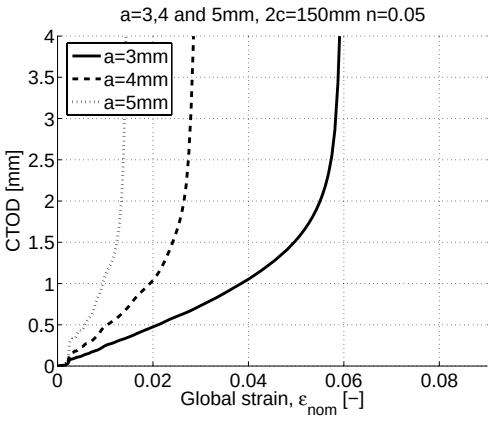

(b)

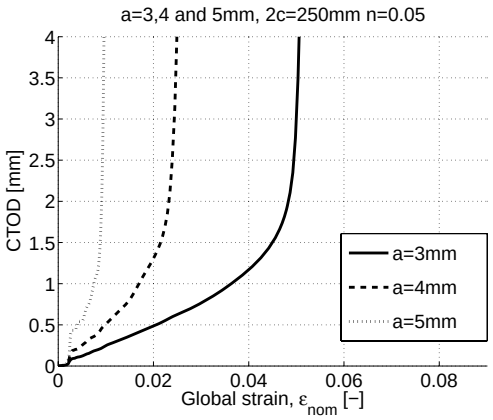

(c)

Figure 6: The effect of different defect depths, a, with $2c = 50$ mm, $n = 0.05$.

the differences are most pronounced for $a = 5$ mm, as seen in Figure 8(c). It is observed that Region 2 is narrowed significantly for the two longest defects, such that a rapid increase is CTOD starts almost immediately after the initiation for the deepest cracked pipe. Similar trends are also observed for the two other hardening levels. In Figs. 9(a)-9(c) the effect of hardening variation for one defect length and three different defect depths is illustrated. As expected, the capacity increases as the hardening increases. In Region 2 we observe that the slope increases as the hardening decreases. This means that we have lower CTOD at a given strain for the higher hardening materials. A significant effect is seen on the CTOD evolution for the cases with biaxial loading, caused by internal pressure, as depicted in Figs 10-11. The internal pressure is expressed as the ratio between

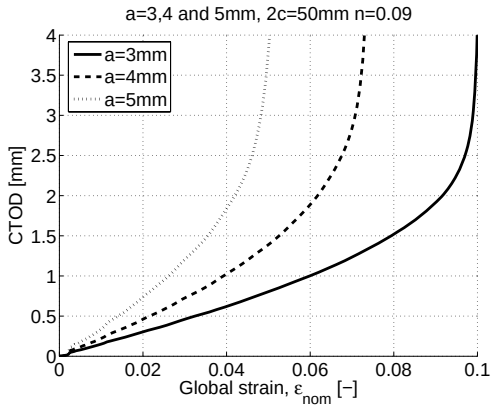

(a)

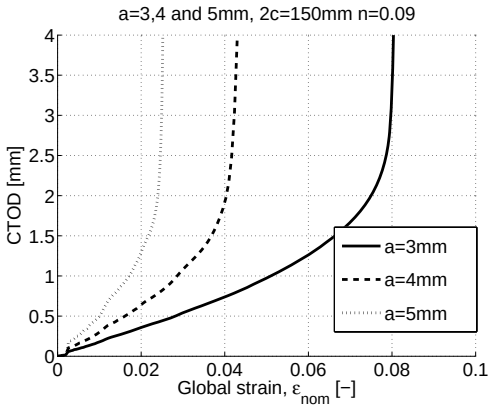

(b)

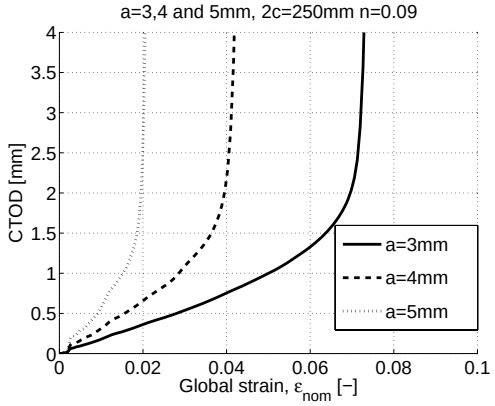

(c)

Figure 7: The effect of different defect depths, a, with $2c = 50$ mm, $n = 0.09$.

the pipe wall hoop stress, σ_h, and the stress at 0.2 % plastic strain, $\sigma_{0.2}$. In Figure 10(a) a comparison between three different pressure levels is presented for a fixed crack depth, $a = 3$ mm, crack length, $2c = 50$ mm, and $n = 0.07$. A significant increase in CTOD at a specific strain level is seen from the unpressurized to the pressurized case. Region 1-3 from Figure 5 are still evident, but the slope of the curves increases with increasing internal pressure. An increase in the internal pressure also reduces the pipe's strain capacity significantly. The same trend for the crack driving force is seen in Figs. 10(c) and 10(b) with deeper defects and consequently less strain capacity. In Fig. 11 results with crack length $2c = 250$ mm are presented. For the deepest crack with $a = 5$ mm, a more serious influence of the internal pressure is observed. The effect is more significant when the pressure is increased from $\sigma_h/\sigma_{0.2} = 0$ to $\sigma_h/\sigma_{0.2} = 0.25$ compared with the

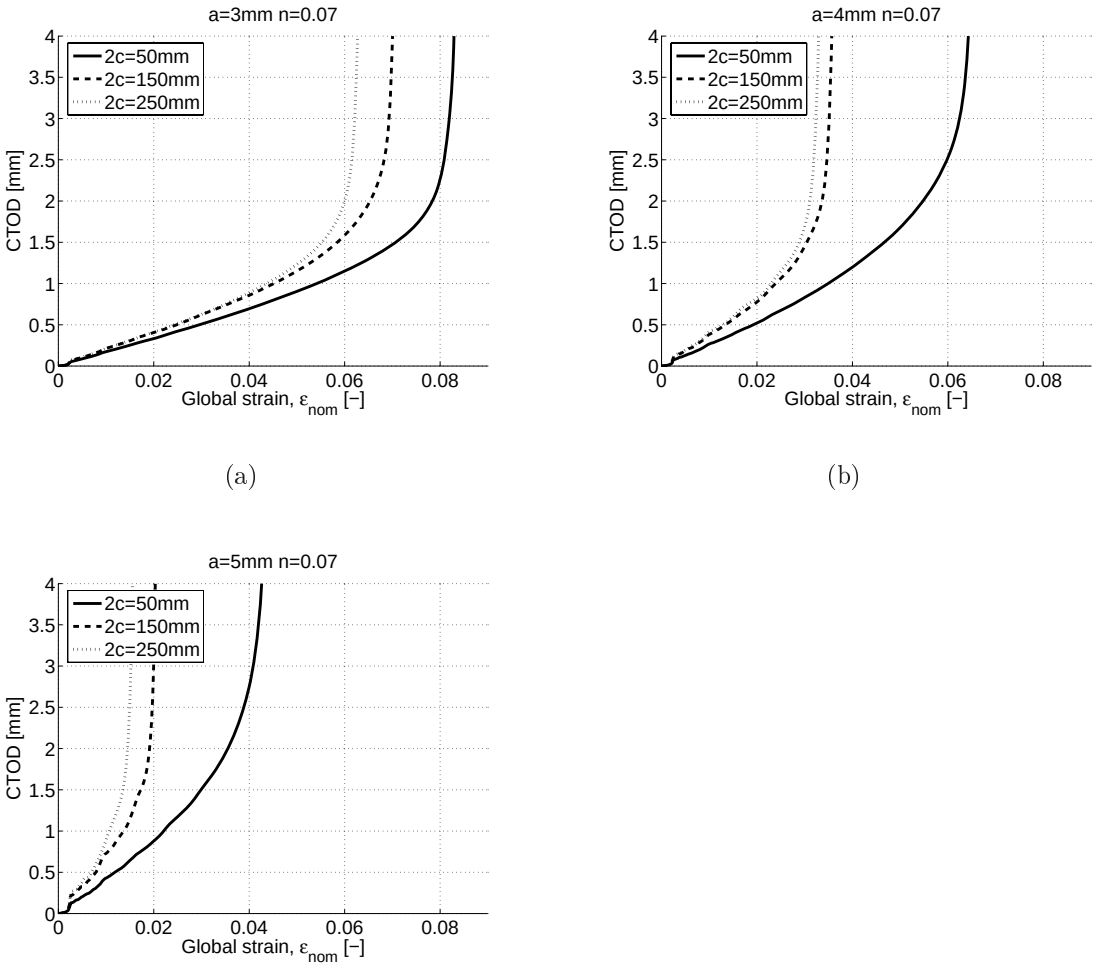

Figure 8: The influence of variation of defect lengths, $2c$, with $a = 3$, 4, and 5 mm, and $n = 0.07$.

increase from $\sigma_h/\sigma_{0.2} = 0.25$ to $\sigma_h/\sigma_{0.2} = 0.5$. For the case in Fig. 11(c) with $\sigma_h/\sigma_{0.2} = 0.25$ and $\sigma_h/\sigma_{0.2} = 0.5$ there is an almost direct transition from the global elastic response situation to a detrimental crack growth. Moreover, it is seen that the CTOD at the end of Region 1 increases rapidly for the cases with internal pressure. Similar observations have been reported by Jayadevan et al. [33] for stationary cracks in 3D FEM analyses of surface cracked pipes in tension. They observed that the biaxial loading strongly enhanced the ligament localization.

Finally, in Figure 12, the crack growth resistance curves derived from some of the analyses are presented. Here the CTOD is plotted against the crack growth,

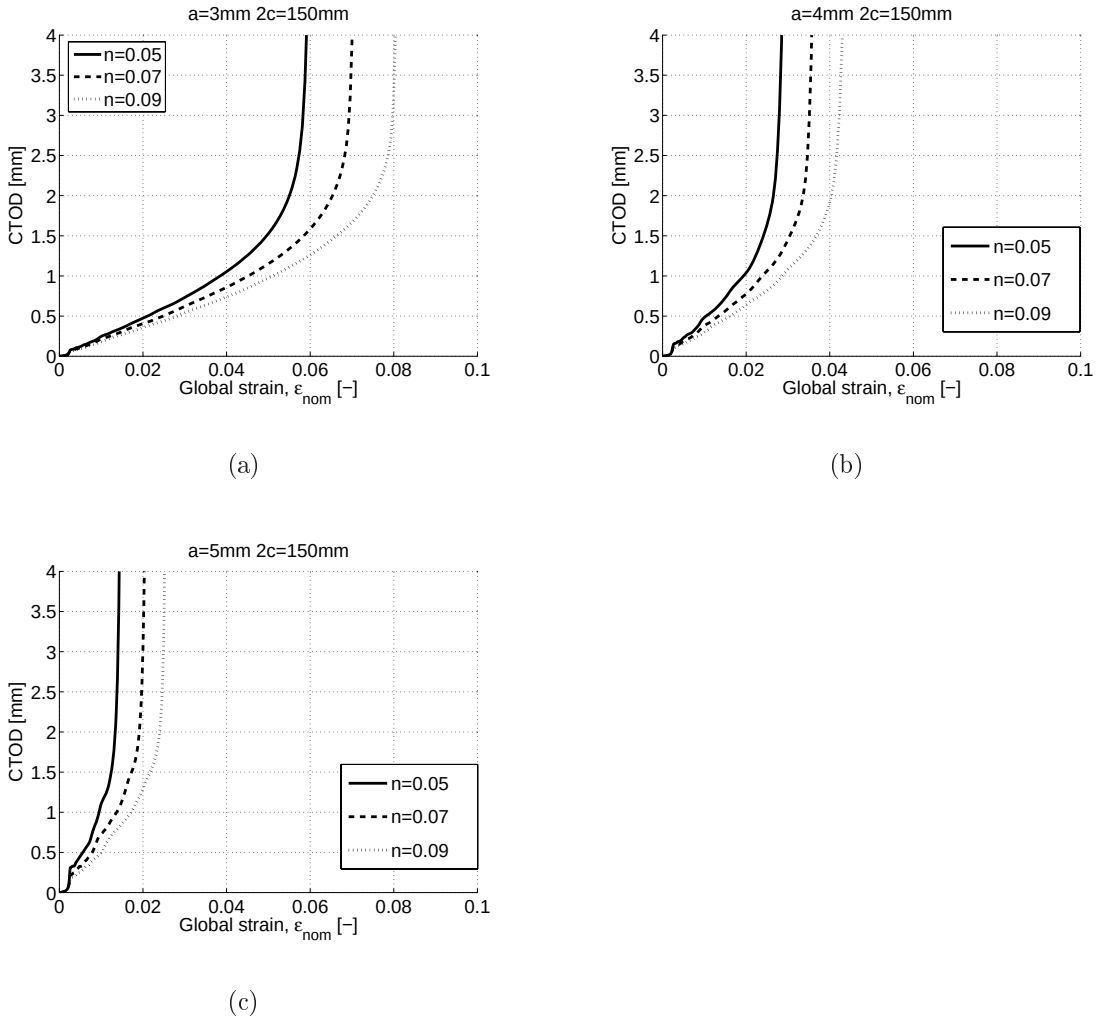

Figure 9: The effect of different hardening levels for a defect with $2c = 150$ mm and three different hardening levels.

Δa. The crack growth curves have been shifted to the right with the value of 0.5 times the CTOD at initiation of ductile tearing. This is an approximative method to account for the blunting included in the experimentally measured crack growth. Some variation is observed between the analyses with various geometries, especially at higher Δa levels. However, only one clear trend was observed in the curves, namely in the cases with the shortest cracks ($2c = 50$ mm). These are the six most elevated resistance curves in the region above $\Delta a = 1$ mm. This result could be a topic for further investigation. From the resistance curve we observe that at $\Delta a = 1$ mm a characteristic CTOD value is about 1.2 mm.

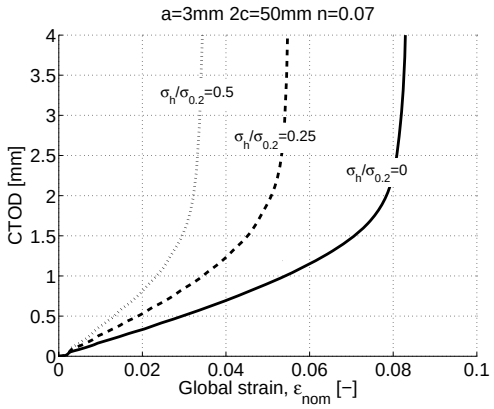

(a)

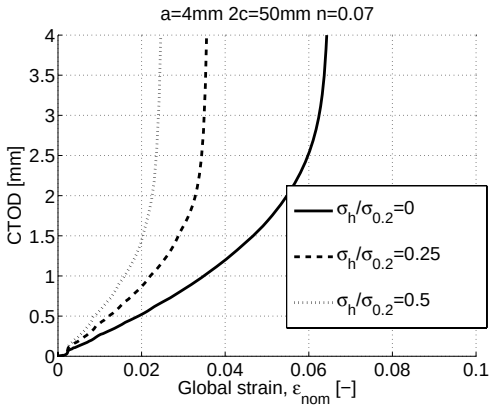

(b)

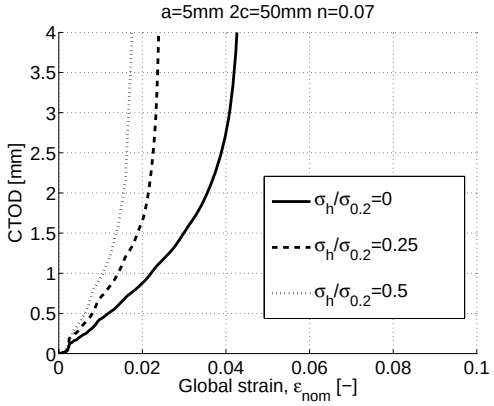

(c)

Figure 10: The effect of three different pressure levels for a defect with $2c = 50$ mm, $a = 3, 4$ and 5 mm, and $n = 0.07$.

4 The probabilistic fracture mechanics model

The next step is to use the deterministic calculations to establish a PFM-model. Such models can be used to describe the structural reliability of a pipe given that we have statistical information of the loading conditions, defect geometry and material, etc. Typically we need an expression to predict when the structure fails, i.e. a failure point, that denotes the structural capacity. If we extract failure points from several simulations that cover a region of interest, and assume a continuous relation between these points, we can establish a function describing the pipe capacity in the region of interest. This function is directly applicable in reliability analyses as the capacity term in the limit state function, $G(\mathbf{x})$. When

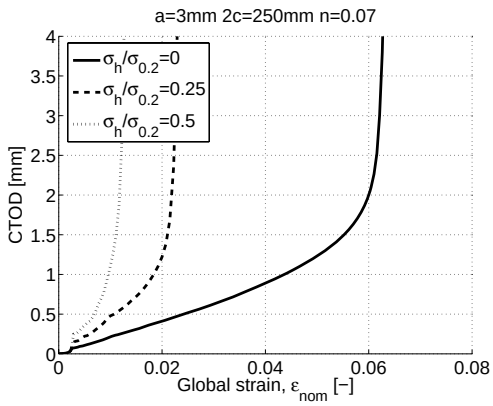

(a)

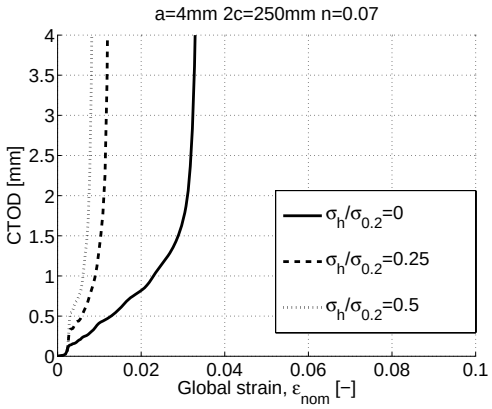

(b)

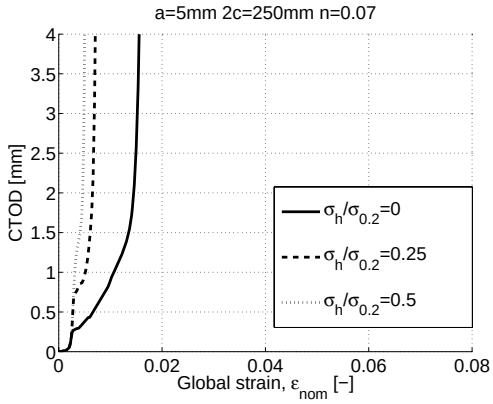

(c)

Figure 11: The effect of three different pressure levels for a defect with $2c = 250$ mm, $a = 3, 4$ and 5 mm, and $n = 0.07$.

this function is known, and we have statistical information of the parameters involved in the problem, we can calculate the probability of failure integral, i.e.

$$p_f = \int_{G(\mathbf{x})\leq 0} f_{\mathbf{X}}(\mathbf{x})\mathbf{dx}, \tag{6}$$

where $f_{\mathbf{X}}(\mathbf{x})$ is the joint probability density function of $\mathbf{X}$, and the limit state function is

$$G(\mathbf{X}) = \varepsilon_{\text{crit}}(\mathbf{X}_1) - \varepsilon_{\text{app}}(\mathbf{X}_2). \tag{7}$$

where $\mathbf{X} = (\mathbf{X}_1, \mathbf{X}_2)$ contains the basic variables. The capacity part is expressed as $\varepsilon_{\text{crit}}(\mathbf{X}_1)$ with the variables of interest represented in the vector $\mathbf{X}_1$. In our case $\mathbf{X}_1 = (a, 2c, \sigma_h/\sigma_{0.2}, n)$, but in general it may contain other variables as

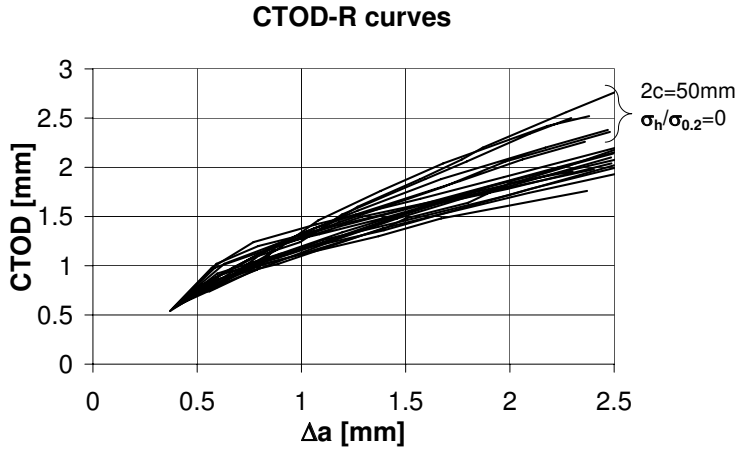

Figure 12: Crack growth resistance curves from the analyses, where CTOD is plotted against crack growth, Δa.

well. Further, the load part is denoted $\varepsilon_{\text{app}}(\mathbf{X}_2)$, where $\mathbf{X}_2$ contains the load variables. $G(\mathbf{X}) \leq 0$ defines the region with structural failure, whereas $G(\mathbf{X}) > 0$ defines the safe region. It is possible to solve the multi-dimensional integral in Eq. (6) with both analytical and numerical methods, [25,38,39]. A well known and simple numerical integration technique is Monte Carlo Simulation (MCS) with or without sampling techniques, see e.g. Melchers [25]. In this paper we apply first and second order reliability methods in the calculation of Eq. (6). This means that the equation is solved by performing a mapping of the probabilistic model with n correlated basic variables into uncorrelated, independent, standard, normal-distributed variables, followed by an approximation of the failure surface at the design point with a hyperplane or a parabolic surface. A vital property from this mapping is that it retains the statistical properties of the probabilistic model. For a general, multi-dimensional problem with correlated variables represented with different statistical distributions, Hohenbichler and Rackwitz [40] proposed to use the established Rosenblatt transformation technique [41]. This stepwise mapping technique requires a known joint probability function $F_{\mathbf{X}}(\mathbf{x})$ in addition to conditional distributions. If we have n basic variables, which may be correlated, defined in the $\mathbf{x}$-space as $\mathbf{X} = (X_1, X_2, ..., X_n)$, and the uncorrelated standard normal variables represented in $\mathbf{u}$-space with uncertainty variables

$\mathbf{U} = (U_1, U_2, ..., U_n)$, we can express the variable transformation $\mathbf{T}$ as:

$$\mathbf{T}: \begin{cases} u_1 & = \Phi^{-1}(F_1(x_1)) \\ u_2 & = \Phi^{-1}(F_2(x_2 \mid x_1)) \\ & ... \\ u_n & = \Phi^{-1}(F_n(x_n \mid x_1, x_2, ..., x_{n-1})). \end{cases} \tag{8}$$

where the conditional cumulative distribution for $j = 2, .., n$ is given by

$$F_j(x_j \mid x_1, ..., x_{j-1}) = \frac{\int_{-\infty}^{x_j} f_{\mathbf{X}_j}(x_1, ..., x_{j-1}, t)dt}{f_{\mathbf{X}_{j-1}}(x_1, ..., x_{j-1})}. \tag{9}$$

The limit state function in $\mathbf{u}$-space, $G(\mathbf{u})$, in terms of $G(\mathbf{x})$, is expressed as

$$G(\mathbf{x}) = G(\mathbf{T^{-1}}(\mathbf{u})). \tag{10}$$

In the Gaussian $\mathbf{u}$-space we have different possibilities for the limit state function. One is to linearize around the design point using a first order Taylor expansion. The design point represents the highest probability of failure on the given failure surface, i.e the point on the failure surface closest to the co-ordinate origin. The distance from the origin to the design point is denoted as β, known as the safety index. Due to the rotational symmetry in the $\mathbf{u}$-space the probability of failure can be determined from

$$p_f \approx \Phi(-\beta), \tag{11}$$

where Φ is the univariate standard normal integral. This solution technique is referred to as first order reliability method (FORM). Alternatively, the failure surface can be approximated by a parabolic function around the design point. This solution technique is termed the second order reliability method (SORM), and theory about this method is found in e.g. Melchers [25] or Madsen et al. [38]. Finally, we determined the design point by using the general non-linear optimization constraint procedure solver called Sequential Quadratic Programming (SQP) optimizer [42].

4.1 Failure and response surfaces

It is normally a challenge to establish expressions for the capacity and load terms in the limit state function. If possible, analytical functions are to be preferred, but they may be complex to establish. Another method is to establish continuous functions from deterministic point-wise solutions for the capacity using e.g. FEM or experiments. In this paper the established function representing the capacity is denoted ε_{crit}, Eq. (7). This method is called the Response Surface Method (RSM). Based on the parameter variation in the present work a second degree polynomial was found to represent the failure points with acceptable precision.

The cross-terms in the polynomial function were found to be important for the surface quality. It should be noted that the choice of limit state function is dependent on the specific case. Four variables are varied in the deterministic analyses to describe a second degree polynomial:

$$\bar{\varepsilon}_{crit} = \alpha_0 + \sum_{i=1}^{4} \alpha_i y_i + \sum_{i=1}^{4} \alpha_{ii} y_i^2 + \sum_{\substack{i=1 \\ i<j}}^{4} \sum_{j=1}^{4} \alpha_{ij} y_i y_j, \tag{12}$$

where y_i and y_j denote the variables, and the α coefficients are determined through regression analyses and least square optimization. A base point in the middle of all the simulations results was selected with values $a = 4$ mm, $2c = 150$ mm, $\sigma_h/\sigma_{0.2} = 0.25$, and $n = 0.07$. This implied the following linear variable transformation: $y_1 = \frac{a}{4} - 1$, $y_2 = \frac{2c}{150} - 1$, $y_3 = 4\frac{\sigma_h}{\sigma_{0.2}} - 1$ and $y_4 = \frac{n}{0.07} - 1$. Since the response surface approximation is an explicit expression, the limit state function, Eq.5 could be solved by direct Monte Carlo Simulations (MCS). However, MCS are time-consuming when low failure probability estimates shall be established. This is inconvenient in practical applications, and in this paper it was chosen to apply the faster FORM/SORM technique. The next step was to extract the failure points from the FEM-analyses. Two different failure mechanisms were considered to represent the pipe's global strain capacity, in the process of establishing the response surfaces as described in the next section.

4.2 Global failure criterion

First, we considered the maximum load criterion which is meaningful in engineering design due to its simple physical interpretation. An example of how to determine the global failure is illustrated in Figure 13(a), where the applied load is plotted against the global strain, ε_{nom}. The critical strain, ε_{crit}, at maximum load is also illustrated. In this case the crack growth and local deformation results in a global collapse, Figure 13(b). Here the global strain ε_{nom}, is plotted against CTOD. A rapid change in CTOD for a small variation of the global strain is observed in this region. Consequently, the almost vertical driving force curve indicates a maximum capacity level. In this case, the ductile tearing starts at about CTOD= 0.6 mm, and a significant amount of ductile tearing has therefore occurred before the maximum load is reached. The 15 coefficients determined from the least square optimization from the establishment of the response surface, are given in Table 3.

4.3 Local failure criterion

Additionally, a local failure criterion proposed by Østby et al. [43] was examined. This criterion predicts the CTOD at maximum load in the crack ligament, δ_{max},

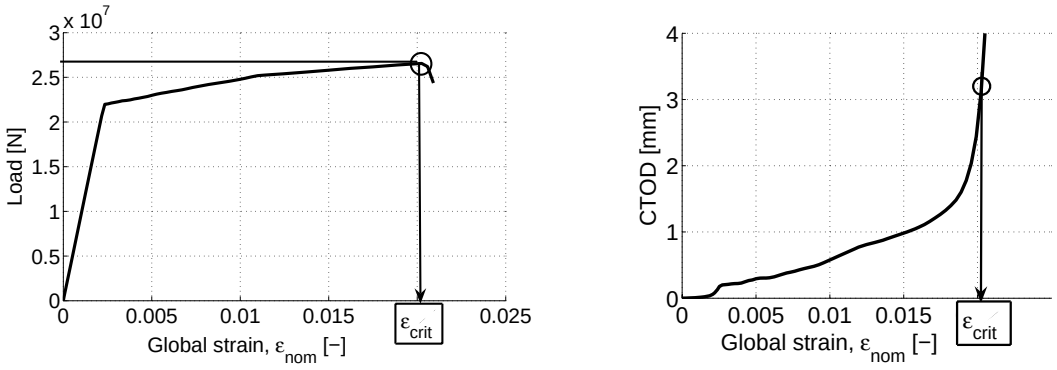

(a) (b)

Figure 13: The maximum load failure criteria. (a) Load vs. strain curve and the corresponding (b) CTOD vs. strain for a pipe with $a = 5$ mm, $2c = 250$ mm and n=0.09. The critical strain, ε_{crit}, is depicted in both figures.

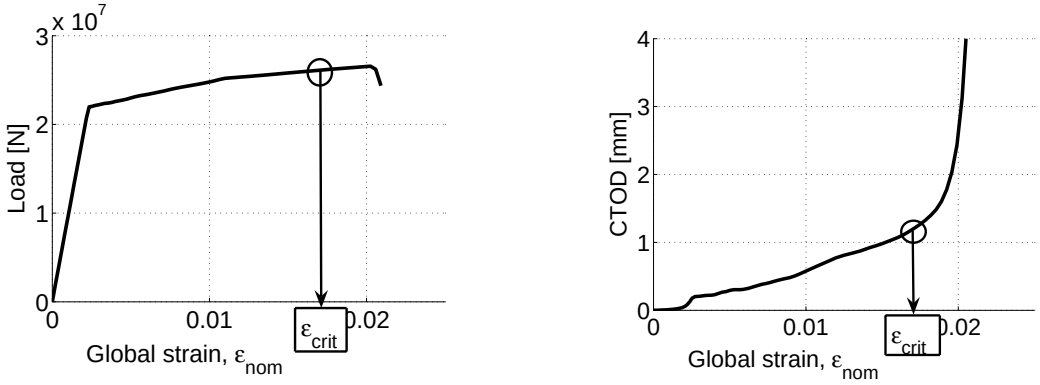

(a) (b)

Figure 14: The local failure criteria. (a) Load vs. strain curve and the corresponding (b) CTOD vs. strain for a pipe with $a = 5$ mm, $2c = 250$ mm and n=0.09. The critical strain, ε_{crit}, is depicted in both figures.

i.e.

$$\delta_{max} = (0.03L + \delta_{\Delta a=1mm} - 0.61)(-12.1(\frac{\sigma_{0.2}}{\sigma_{TS}})^2 + 18.9(\frac{\sigma_{0.2}}{\sigma_{TS}}) - 6.28), \qquad (13)$$

where L is the ligament height, $\delta_{\Delta a=1}$ mm is the CTOD at 1 mm crack growth, and $\sigma_{0.2}$ and σ_{TS} are the engineering yield stress and tensile strength, respectively. The same optimization procedure as used in Section 4.2 was followed to

Table 3: Coefficient values for the response surface from the global failure criterion.

Coeff.	α_0	α_1	α_2	α_3	α_4	α_{11}	α_{22}	α_{33}
Value	0.0148	-0.0509	-0.0168	-0.0162	0.0229	0.0565	0.0169	0.0087
Coeff.	α_{44}	α_{12}	α_{13}	α_{14}	α_{23}	α_{24}	α_{34}	
Value	0.0117	0.0058	0.0309	-0.0342	0.0035	-0.0067	-0.0073	

establish the coefficients in Eq. (12) which are listed in Table 4.

Table 4: Coefficient values for the response surface established using the local failure criteria.

Coeff.	α_0	α_1	α_2	α_3	α_4	α_{11}	α_{22}	α_{33}
Value	0.0122	-0.043	-0.0096	-0.0109	0.0218	0.0531	0.0095	0.0052
Coeff.	α_{44}	α_{12}	α_{13}	α_{14}	α_{23}	α_{24}	α_{34}	
Value	0.0047	0.0086	0.0262	-0.0338	0.0004	-0.0050	-0.0069	

Three examples of the response surface using the local failure criterion are presented in Figs.15-17. The response function is plotted in three different spaces within the predefined parameter window listed in Table 1. The original failure points which were extracted using the local failure criterion are depicted as '+'. Additionally, a bar from this point to the established surface is drawn to illustrate the accuracy of the approximation. Thus, if the bar is above or below the surface the approximation is conservative or un-conservative, respectively. First, in Figure 15, the critical strain is plotted as a function of the crack depth, a, and internal pressure, $\sigma_h/\sigma_{0.2}$. A very good fit between the deterministic point-wise solutions and the established surface is observed. Some minor deviations are seen on the edges but these represent rather small relative errors. In Figure 16 the critical strain is plotted as a function of the crack depth, a and crack length, $2c$. Again a very good fit between the established response surface and the point-wise solutions is observed. Finally, in Figure 17, the function values on the axes are crack depth, a and hardening, n. The surface almost represents the points satisfactorily, but a significant deviation is observed at the corner where $a = 5$ mm and $n = 0.05$. The surface is conservative in this area, i.e. the strain capacity is under-predicted. However, this may not be a problem as long as the calculated design point ends up elsewhere in our domain. If this region needs modification, several adjusting techniques are available to solve this problem, such as weighting, but they are not dealt with in this paper.

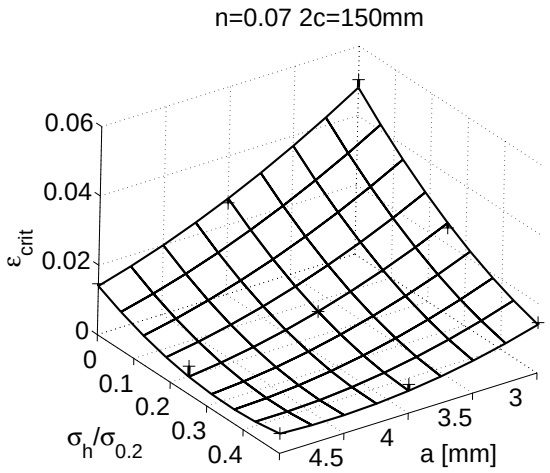

Figure 15: The response surface plotted as a function of the crack depth, a, and the internal pressure, $\sigma_h/\sigma_{0.2}$.

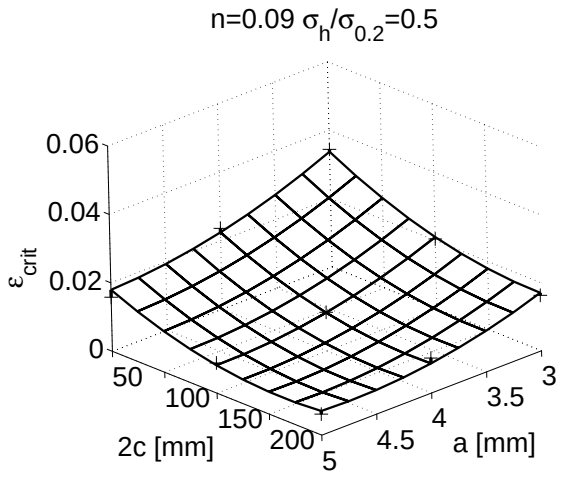

Figure 16: The response surface plotted as a function of the crack depth, a, and the crack length, $2c$.

4.4 Example using the PFM-model

The PFM-model is now applied for a specific case with a pipe subjected to bending. The results from the tension loaded pipes are applied, but the external load

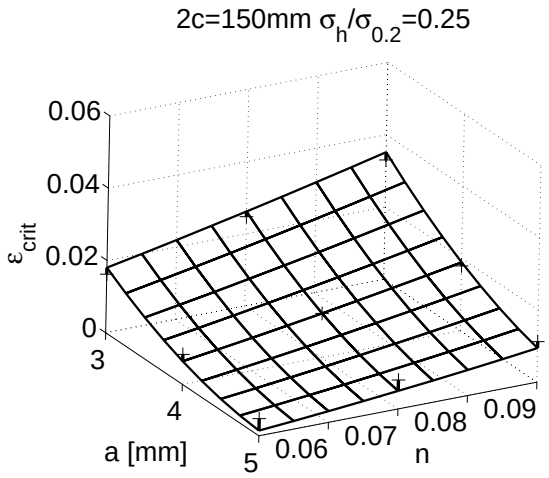

Figure 17: The response surface based on the local criterion plotted as a function of the crack depth, a, and the material hardening exponent, n.

is assumed to form a linear strain variation over the pipe cross-section as depicted in Fig. 18. The defect localization was determined from a stochastic sampling using MCS from the uniform distribution for ϕ (Table 5), and the maximum strain at the given defect was obtained. This assumption implies that the defect was subjected to a uniform strain corresponding to the maximum strain. Additionally, the critical strain for the given defect geometry was taken from the established response functions. The procedure also calculated the effective crack length, which is the part of the defect placed in the tension part of the pipe cross section. If the defect location passed the top of the pipe (12 o'clock in the cross-section in Fig. 18) the maximum strain was set to remain ε_{lay}. Otherwise, the maximum tension strain ε_{app} was modified to ε_{mod}.

Two load cases were investigated for several deterministic pressure levels. The load with a corresponding strain, which here is given as the strain ε_{lay}, has two contributing parts, static and dynamic. These are represented by normal distributions summed up to a "total" strain distribution with mean value 1 % and 1.5 % in load cases LC1 and LC2, respectively. The dynamic load contributes with 15 % and the static 85 % to the total load. The input data for the reliability analyses is listed in Table 5.

Table 5: Input parameters and distributions used in the analyses.

Description		Distribution	$E[-]$	COV
Depth, [mm]	a	Lognormal	1	0.5
Length, [mm]	2c	Lognormal	75	0.33
Hardening, [-]	n	Normal	0.07	$7.14 \cdot 10^{-2}$
Static load (strain) [-]	ε_s	Normal	$0.0085, 0.01275$	0.1
Dynamic load (strain) [-]	ε_d	Normal	$0.0015, 0.00225$	1
Angle [-]	ϕ	Uniform	π	-
Pressure [-]	$\sigma_h/\sigma_{0.2}$	-	$0 - 0.5$	-

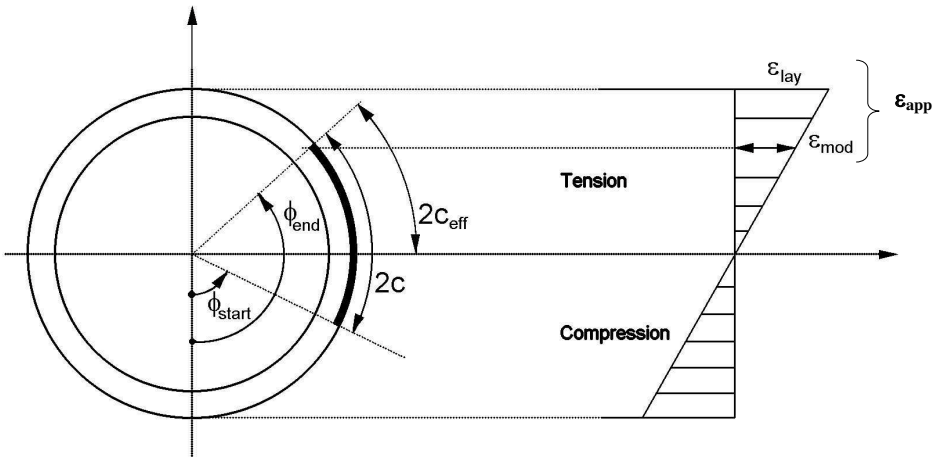

Figure 18: The effective crack length and the applied strain, ε_{app} in a given pipe cross section for a pipe in bending.

5 Results and discussion

In Figs. 19-21 the probability of failure, p_f, is plotted against internal pressure, $\sigma_h/\sigma_{0.2}$. Two different load cases are presented, namely LC1 and LC2 from sim-

ulations using the "Global criterion" and the "Local criterion". The mean values were E[Load]=0.01 and E[Load]=0.015 in LC1 and LC2, respectively. Both SORM and FORM results are presented.

In Figure 19 results from the "Global criterion" simulations for LC1 and LC2 are presented. The FORM results over-predict the p_f compared with the SORM simulations. However, this over-prediction is most significant for the lower pressure ratios. Another observation is that an increase in internal pressure, $\sigma_h/\sigma_{0.2}$,

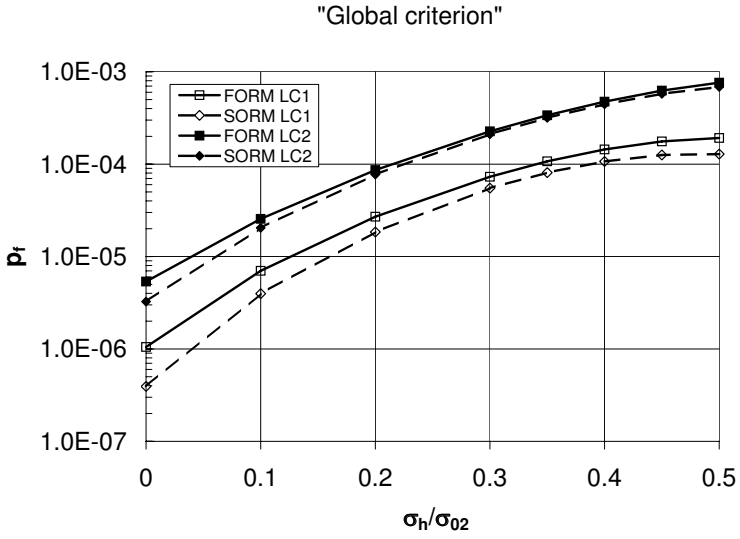

Figure 19: Probability of failure plotted against $\sigma_h/\sigma_{0.2}$, for LC1 and LC2 using the "Global criteria".

results in a corresponding increase in p_f. There is an approximately two decade difference in the p_f level from the un-pressurized pipe to pressurized pipe with $\sigma_h/\sigma_{0.2} = 0.5$, which is in accordance with earlier observations, [23]. The same trend is observed for both load cases. In the cases using the "Local criterion", Fig. 20, we observe similar trends of the influence of internal pressure. However, the local criterion predicts higher probability of failure than the global criterion. This is as expected since the critical strain level using the "Local criterion" is

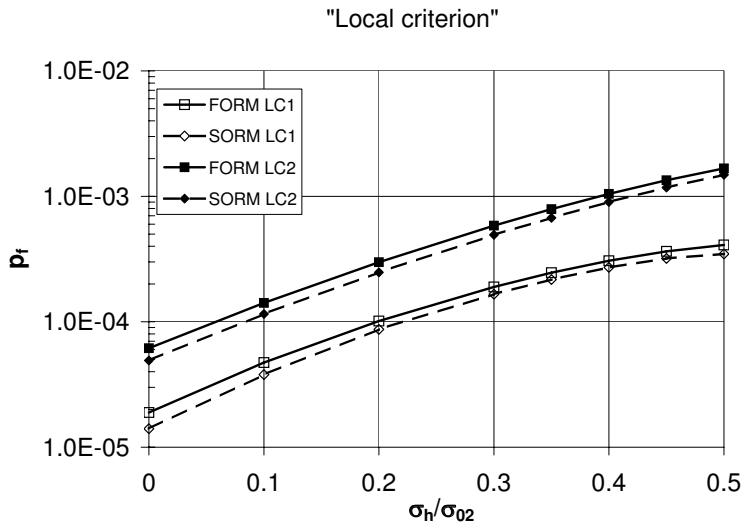

Figure 20: p_f plotted against $\sigma_h/\sigma_{0.2}$, for LC1 and LC2 using the "Local criteria".

lower than using the "Global criterion". In Figure 21 the SORM results from the two previous figures are compared. A significant difference is observed for low $\sigma_h/\sigma_{0.2}$ ratios. However, it is believed that both criteria are applicable for calibration purposes. Finally, it should be noted that the presented failure estimates using FORM/SORM depends on the representativeness of Eq. (12). Possibly, some effort could be done to evaluate the goodness of the choice of function. This would, however, involve a larger number of heavy FEM-calculations, which are inappropriate in this context.

5.1 Limitations

The response surfaces are established within a specific window of parameters. It has been assumed that we have a continuous failure value relation inside this region. This may be plausible, but the validity outside this region is likely to be more restricted. Consequently, in a practical problem it must be checked whether

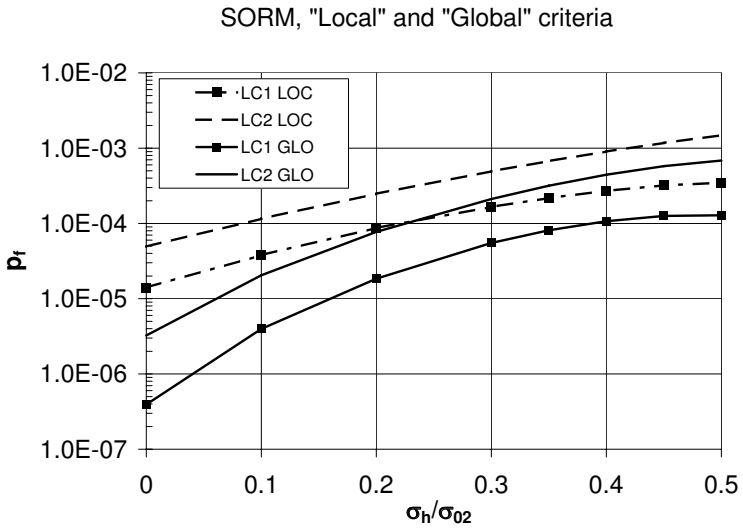

Figure 21: Comparison of SORM-results from analyses using the "Local" and "Global" criteria for LC1 and LC2.

the design point obtained from the reliability analyses is within the parameter window. If not, some precautions should be taken. One alternative is to run a few extra FEM-analyses to check if the outcome is on the "safe side" of the response surface. If so, the reliability solution may be valid for the given case. Another solution is to define a new solution matrix with another basis point which is nearer to the design point in the former analyses. Alternatively, other function expressions may be investigated.

6 Conclusions and further work

Abaqus Explicit and FEM were employed in the solution of surface cracked pipes subjected to tension load in combination with internal pressure. A total of 81 3D FE-analyses were made including large plastic deformations with ductile tearing using the Gurson-Tvergaard-Needleman criterion. The defect depth variation

and the effect of internal pressure were shown to significantly influence the strain capacity of the pipes. An increase in the material hardening increased the pipe capacity. A crack length effect was observed with a decrease in the pipe capacity as the crack length increased. However, this effect was reduced for larger crack lengths.

The simulation results were used to establish response surfaces. Both local and global failure criteria were employed, and it was shown that the capacity of the surface cracked pipes in tension could be well represented with quadratic surfaces. The strong influence of internal pressure was clearly evident.

3D ductile tearing analyses represent high computational cost in addition to beeing time-consuming and complex to handle. Therefore, we have decided to use Link_{pipe} in the following work. This is a newly developed program using linespring and shell elements based on the ideas of Rice and Levy [44] and Parks and White [45]. A thorough examination of the numerical aspects and implementation of the linespring element into the Link_{pipe} software is given in Skallerud et al. [46], Jayadevan et al. [47] and Thaulow et al. [48]. Link_{pipe} can, among other things, take into account ductile tearing effects, internal and external pressure, bending and tension loads, and mismatch. Since this solution technique will reduce the computational time considerably, further parameters can easily be included in the stochastic models in order to improve their applicability.

Finally, an alternative method to the RSM and FORM/SORM exists, namely a new dimensional decomposition method suitable for stochastic mechanics presented by Rahman [49]. This method appears to provide accurate probabilistic characteristics at lower computational cost, and should be considered in the further work.

Acknowledgements

The authors want to express their gratitude to the Joint Industry Project Fracture Control - Offshore Pipelines with the following funding participants: Statoil, Hydro, BP, ENI Norge, Technip and the Research Council of Norway. The assistance from Dr. Knut-Aril Farnes at Statoil Research Center, Trondheim, Norway, has been highly appreciated.

References

[1] BSI, Guide on methods for assessing the acceptability of flaws in metallic structures, BS 7910, British Standards Institution (2000).

[2] Assessment of the integrity of structures containing defects - revision 4, R6, British Energy (2001).

[3] C. Thaulow, B. Skallerud, K. Jayadevan, E. Berg, Fracture control offshore pipelines - advantages of using direct calculations in fracture assessments of pipelines, In: 24th International Conference on Offshore Mechanics and Arctic Engineering (2005).

[4] SINTEF, Fracture control-offshore pipelines (JIP), Trondheim, Norway, 2002-2006.

[5] E. Østby, Fracture control offshore pipelines - new strain-based fracture mechanics equations including the effects of biaxial loading, mismatch, and misalignment, 24th International Conference on Offshore Mechanics and Arctic Engineering (2005).

[6] DNV-OS-F101, Offshore standard, submarine pipeline system, Standard, Det Norske Veritas (2000).

[7] F. Beremin, A local criterion for cleavage fracture of a nuclear pressure vessel steel, Metallurgical Transactions 14A (1983) 2277–2287.

[8] S. Slatcher, A probabilistic model for lower-shelf fracture toughness - theory and application, Fatigue Fract. Engng. Mater. Struct. 9 (4) (1986) 275–289.

[9] M. Hauge, A probabilistic approach to fracture mechanics assessment of structural steel weldments, Doktoringeniør thesis, The Norwegian Institute of Technology, Division of Materials and Processes (1990).

[10] J. Tronskar, M. Mannan, M. Lai, G. Sigurdsson, K. Halsen, Crack tip constraint correction applied to probabilistic fracture mechanics analyses of floating production, storage and off-loading vessels, Engineering Fracture Mechanics 70 (11) (2003) 1415–1446.

[11] T. Bokalrud, A. Karlsen, A probabilistic fracture assessment of fatigue failure from weld defects in butt welds joints, Conf. on Fitness for Purpose Validation of Welded Constructions (1981).

[12] C. Ruggieri, R. Dodds Jr., Probabilistic modeling of brittle fracture including 3-d effects on constraint loss an ductile tearing, Journal de physique IV 6 (1996) 353–362.

[13] Y. Chen, S. Lampert, Numerical modeling of ductile tearing for elliptical surface cracks in wide plates, International Journal of Pressure Vessels and Piping 82 (2005) 417–426.

[14] S. Rahman, A stochastic model for elastic-plastic fracture analysis of circumferential through-wall-cracked pipes subject to bending, Engineering Fracture Mechanics 52 (2) (1995) 265–288.

[15] S. Rahman, Probabilistic fracture analysis of cracked pipes with circumferential flaws, International Journal of Pressure Vessels and Piping 70 (1997) 223–236.

[16] S. Rahman, F. Brust, Approximate methods for predicting J-integral of a circumferentially surface-cracked pipe subject to bending, International Journal of Fracture 85 (1997) 111–130.

[17] S. Rahman, Probabilistic elastic-plastic fracture analysis of circumferentially cracked pipes with finite-length surface flaws, Nuclear Engineering and Design 195 (2000) 239–260.

[18] M. Francis, S. Rahman, Probabilistic analysis of weld cracks in center-cracked tension specimen, Computers and Structures 76 (2000) 483–506.

[19] H. Ernst, D. Passarella, R. Bravo, F. Daguerre, Structural reliability analysis of pipes subjected to multiple strain cycles – application to reeling processes, Proceedings of OMAE2006, 25th International Conference on Offshore Mechanics and Arctic Engineering OMAE2006-92473.

[20] H. Ernst, R. Schifini, R. Bravo, D. Passarella, F. Daguerre, M. Tivelli, Probabilistic fracture mechanics structural reliability analysis of reeled pipes, Proceedings of OMAE2006, 25th International Conference on Offshore Mechanics and Arctic Engineering OMAE2006-92474.

[21] S. Rahman, G. Chen, R. Firmature, Probabilistic analysis of off-center cracks in cylindrical structures, International Journal of Pressure Vessels and Piping 77 (2000) 3–16.

[22] J. Foxen, S. Rahman, Elastic-plastic analysis of small cracks in tubes under internal pressure and bending, Nuclear Engineering and Design 197 (2000) 75–87.

[23] A. Sandvik, E. Østby, C. Thaulow, Probabilistic fracture assessment of surface cracked pipes using strain-based approach, Engineering Fracture Mechanics 73 (2006) 1491–1509.

[24] G. E. P. Box, R. D. Draper, Empirical model building and response surfaces, Wiley, 1987.

[25] R. Melchers, Structural reliability analysis and prediction, 2nd Edition, John Wiley & Sons, 1999.

[26] A. Sandvik, E. Østby, C. Thaulow, Abaqus explicit simulations of strain capacity in pipelines including the effect of biaxial loading and ductile tearing, In: proceedings from Abaqus User's Conference, AUC2006.

[27] Abaqus User's Manual Version 6.4 (2003).

[28] A. Gurson, Continuum theory of ductile rupture by void nucleation and growth: Part 1 - yield critera and flow rules for porous ductile materials, Journal of Engng. Materials and technology 99 (1977) 2–15.

[29] V. Tvergaard, Influence of voids on shear band instabilities under plane strain conditions, Int. Journal of Fracture 17 (1981) 389–407.

[30] V. Tvergaard, A. Needleman, Analyses of the cup-cone fracture in a round tensile bar,, Acta Metallurgica 32 (1984) 157–169.

[31] M. Wilkins, Computer simulation of dynamic phenomena, Scientific computation, Springer, 1999.

[32] T. Belytschko, W. Liu, B. Moran, Nonlinear finite elements for continua and structures, John Wiley & sons Ltd., 2003.

[33] K. Jayadevan, E. Østby, C. Thaulow, Fracture response of pipelines subjected to large plastic deformation under tension, International Journal of Pressure Vessels and Piping 81 (2004) 771–783.

[34] J. Rice, A path independent integral and the approximate analysis of strain concentration by notches and cracks, Journal of Applied Mechanics 35 (1968) 379–386.

[35] J. Hutchinson, Fundamentals of the phenomenological theory of nonlinear fracture mechanics, Journal of Applied Mechanics 49 (1982) 103–197.

[36] C. Shih, Relationship between the J-integral and the crack opening displacement for stationary and extending cracks, Journal of the Mechanics and Physics of Solids 29 (1981) 305–326.

[37] E. Østby, K. Jayadevan, C. Thaulow, Fracture response of pipelines subject to large deformations under bending, International Journal of Pressure Vessels and Piping (2004) (2004) 201–215.

[38] H. Madsen, S. Krenk, N. Lind, Methods of structural safety, Prentice Hall, 1986.

[39] P. Thoft-Christensen, M. Baker, Structural Reliability Theory and its Applications, 1st Edition, Springer-Verlag, Berlin, Germany, 1982.

[40] M. Hohenbichler, R. Rackwitz, Nonnormal dependent vectores in structural reliability, Journal of Engineering Mechanics Division 107 (1981) 1127–1238.

[41] M. Rosenblatt, Remarks on a multivariate transformation, The Annals of Mathematical Statistics 23 (1952) 470–472.

[42] DNV, Proban theory, Sesam user manual, Det Norske Veritas (2002).

[43] E. Østby, E. Torselletti, E. Levold, A strain-based approach to fracture assessment of pipelines, FITNET 2006 Conference, Paper no. 35, 17-19th of May 2006, Amsterdam, The Netherlands.

[44] J. Rice, N. Levy, The part through surface crack in an elastic plate, Journal of applied mechanics (1972) 185–194.

[45] D. Parks, C. White, Elastic plastic linespring finite element formulation, Computers and structures 104 (1982) 287–292.

[46] B. Skallerud, K. Holthe, B. Haugen, Thin shell and surface crack finite elements for simulation of combined failure modes, Computer methods in applied mechanics and engineering (2004) 2619–2640.

[47] K. Jayadevan, C. Thaulow, E. Østby, E. Berg, B. Skallerud, K. Holthe, B. Nyhus, Structural integrity of pipelines:T-stress by line-spring, Fatigue and Fracture of Engineering Materials and Structures 28 (2005) 467.

[48] C. Thaulow, K. R. Jayadevan, E. Østby, E. Berg, B. Skallerud, K. Holthe, B. Nyhus, Advances in computational procedures for the structural integrity of pipelines, International Conference on Advances in Structural Integrity (2004).

[49] S. Rahman, A dimensional decomposition method for stochastic fracture mechanics, Engineering Fracture Mechanics 73 (2006) 2093–2109.

A probabilistic ductile fracture mechanics model for bi-axially loaded surface-cracked pipes using shell and line-spring elements*

Andreas Sandvik, Erling Østby, and Christian Thaulow

Abstract

A new probabilistic fracture mechanics model for surface-cracked pipes is presented. The model applies FEM-simulations using shell and line-spring elements where ductile tearing effects are accounted for. The pipes are subjected to loading in tension combined with internal pressure. A number of variables are included in the model: internal pressure, material resistance, crack depth and crack length. In the reliability analyses the strain capacity is predicted from the FEM results using two different failure criteria: the maximum load criterion and a local criterion. The response surface technique is applied to represent the structural resistance in the reliability models, and examples are presented for illustration. The established models are solved using first and second order reliability methods as well as Monte-Carlo Simulation with and without importance sampling. The results clearly illustrate the important effect from the internal pressure on the pipe's strain capacity; increasing pressure decreases the strain capacity.

*Published in Engineering Fracture Mechanics, Vol. 73, pp. 1491-1509, 2006.

Nomenclature

t	pipe wall thickness
D	outer pipe wall diameter
ϕ	angle at the circumference of the pipe
$\sigma_0, \sigma_{0.2}$	stress at the proportional limit, stress at 0.2% plastic strain
σ_i, σ_{TS}	flow stress, tensile strength
σ_h	hoop stress
n	hardening exponent
E	Young's modulus
ν	Poisson ratio
$CTOD$	crack tip opening displacement
ε	nominal global longitudinal strain
ε_0, ε_p	strain at the proportional limit, plastic strain
ε_{lay}, ε_{app}	strain due to laying, strain input to the limit state equation
ε_{crit}, $\bar{\varepsilon}_{crit}$	critical strain (capacity), critical strain function
ε_{critG}	critical strain estimated from the global maximum load criterion
ε_{critL}	critical strain estimated from the local criterion
p_f	probability of failure
$\mathbf{X}$	n-dimensional random vector
$\mathbf{x}$	realizations of $\mathbf{X}$
$f_{\mathbf{X}}(\mathbf{x})$	joint probability density function of $\mathbf{X}$
$F_{\mathbf{X}}(\mathbf{x})$	joint probability function
X_i	i-th random variable in x-space
$\mathbf{U}$	n-dimensional random vector in $\mathbf{u}$-space
$\mathbf{u}$	realization of $\mathbf{U}$
U_i	i-th uncorrelated standard normal random variable
$G(\mathbf{x}), G(\mathbf{u})$	limit state functions in $\mathbf{x}$ and $\mathbf{u}$-space
Φ	univariate standard normal integral
β	safety index
$\alpha, \alpha_i, \alpha_{ii}, \alpha_{ij}$	polynomial coefficients
δ_R	CTOD, material resistance

1 Introduction

Simple and reliable standardized assessment procedures are generally of utmost importance in structural engineering to ensure a safe and cost effective design. This is also the case for offshore pipeline engineering, where the pipeline can be exposed to a variety of loading conditions. Large deformations can occur during installation and under operation. During operation the pressurized pipe may be subjected to external loads for example in free-spans due to irregular seabed topography or lateral/upheaval buckles caused by thermal loads.

Existing fracture assessment procedures used in pipeline engineering are mainly established for elastic global response and do not consider large plastic deformations [1]. This may be unsuitable since highly ductile materials, such as pipeline steel, may be subjected to high loads resulting in considerable plastic deformations. Additionally, an amount of ductile tearing may be accepted since it will not necessarily influence the pipe capacity. Fracture Control-Offshore Pipelines is a joint industry project [2] with focus on large plastic deformations and strain-based design for offshore pipelines. The strain-based methodology is believed to hold the potential to improve the physical prediction of the fracture mechanics response. This will enable a more fundamental calibration of partial safety factors for fracture assessment of pipelines. This project has already developed simplified strain-based fracture mechanics equations for surface-cracked pipes, including the effects of biaxial loading, mismatch, and misalignment, see Østby [3]. The simplified equations are used to establish a strain-based project design procedure for laying and operational conditions for offshore pipelines using the partial safety factor format as found in e.g. DNV-OS-F101 [4].

Three dimensional ductile tearing FEM-analyses of pipes with defects are challenging and still not common. Such calculations typically involve complex modelling, time-consuming solution and extensive post-processing. However, 3D FEM models are important in order to investigate the detailed physics of fracture mechanics problems, see e.g. [5]. This is neither suitable in engineering fracture mechanics assessment nor as a basis in probabilistic models for pipes where numerous analyses are needed. A specially designed program based on shell and line-spring elements for fracture mechanics analyses is applied in this paper. This program enables efficient fracture mechanics analysis for pipes with surface cracks. The effect of ductile tearing may be accounted for, and the pipe can be subjected to a combination of bending, tension and pressure loads. Local buckling is also included, which may be convenient since buckling and fracture are competing failure modes for a pipe subjected to bending loads.

Probabilistic calculations for ductile materials have mainly been contributed in the past decade by Rahman and various co-authors. Their main focus has been on through-wall and internal cracks on relatively thick-walled pipes using FEM and analytical methods [6-12].

In Sandvik et al. [13] 3D FEM models of surface-cracked pipes subjected

to tension in combination with internal pressure were presented. These models were used to establish a probabilistic fracture mechanics model (PFM) using the response surface technique. Another PFM model using simplified strain based equations from [3] was presented in Sandvik et al. [14].

In the present paper models of pipes with outer surface cracks subjected to uniform tension in combination with internal pressure are presented. The models include the effect of ductile tearing. In the first part we present the deterministic FE-models with shell and line-spring elements. Pipe and defect geometry, material properties and the ductile tearing model are presented and explained. Some of the results are compared with 3D FEM results obtained from Abaqus/Explicit analyses [13]. The subsequent section explains how the response surfaces are established. Thereafter, the proposed methodology is illustrated with examples where the probability of failure is determined using first and second order reliability methods (FORM and SORM) in addition to Monte-Carlo Simulations with and without importance sampling.

2 FEM-model

Line-spring elements

Three dimensional ductile tearing analysis of surface-cracked pipes represents high computational cost in addition to being time-consuming and complex to handle, see e.g. [13]. A simpler approach is to apply line-springs and shell elements. Here the crack is represented by nonlinear finite element springs, line-springs, with compliance dependent on the plastic deformation and the crack depth. The line-springs are connected to the neighbouring shell elements representing the global pipe. The line-spring concept was originally proposed by Rice and Levy [15], and extended to elastic-plastic stationary crack analysis by Lee and Parks [16]. Ductile crack growth was included in the line-spring formulation by Lee and Parks [17,18] using the ideas of McClintock et al. [19].

Link$_{pipe}$ is a tailor-made program for pipeline applications based on the line-spring technology. This program applies a co-rotated kinematic description of the ANDES shell and line-spring elements [20,21]. Implementation and numerical aspects of Link$_{pipe}$ are presented by Skallerud et al. [22]. In order to simulate the ductile crack growth the traditional material crack-growth resistance curve (i.e. CTOD-Δa curve) is applied as presented in Jayadevan et al. [23].

Geometry

A sketch of a pipe with a surface defect is shown in Fig 1 where a denotes the uniform crack depth and $2c$ the crack length. Three values of pipe wall thickness were considered, namely 15, 20 and 25mm, diameter to thickness ratio

of $D/t = 20$ for all cases. The pipe length, L, is six times the outer diameter of the pipe to limit so-called end effects, which means that the deformations around the defect are not influenced by the boundary conditions. The geometric parameters used in the analyses are found in Table 1 and Table 2.

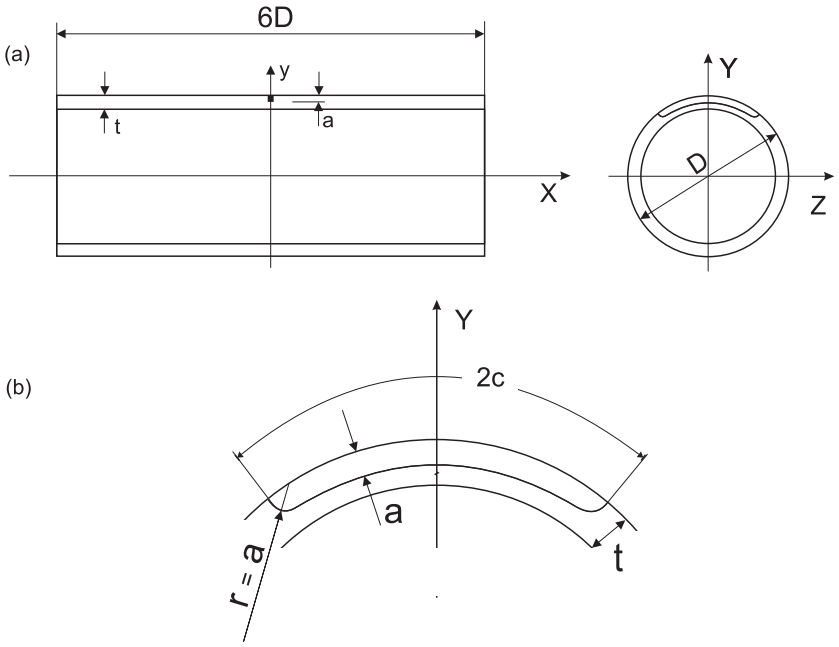

Figure 1: (a) Pipe geometry with an external circumferential constant-depth surface crack. (b) Details of the constant depth crack with arc length ($2c$) and end radius (r) equal to the crack depth (a).

Element mesh

Fig. 2 shows a typical shell mesh of a pipe with diameter 400 mm including a defect placed in the middle of the pipe with crack length $2c = 150$ mm. Line-spring elements simulate the defect. The figure shows that the shell and line-spring FE-mesh is fundamentally different to a 3D solid mesh, where a dense regular mesh around the defect is needed, as seen in Fig. 3. This results in a significant difference in problem size: the depicted Link_{pipe} model has about six thousand degrees of freedom, whereas the 3D Abaqus/Explicit model is about thirty times larger.

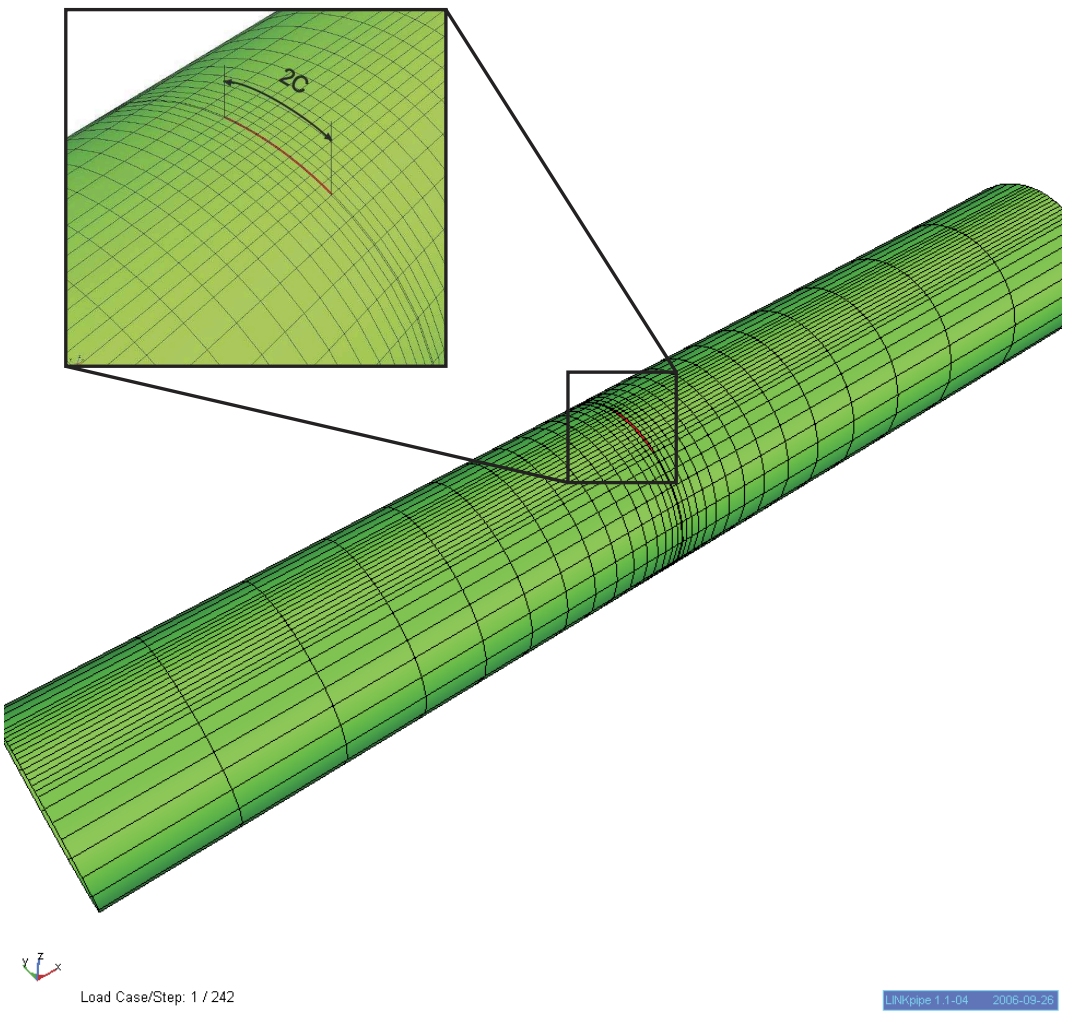

Figure 2: A typical shell & line-spring element mesh of a pipe with surface crack. Insert shows details around the crack.

Loads and boundary conditions

For the pressurized cases, the internal pressure load was applied as a separate load step prior to the tension load. The pressure level is expressed by the ratio between the hoop stress, σ_h, and the stress at 0.2 % plastic strain, $\sigma_{0.2}$, i.e. $\sigma_h/\sigma_{0.2}$. Three load levels were analysed, $\sigma_h/\sigma_{0.2} = 0, 0.25$ and 0.5. The uniform tension load was applied through a displacement at one pipe end.

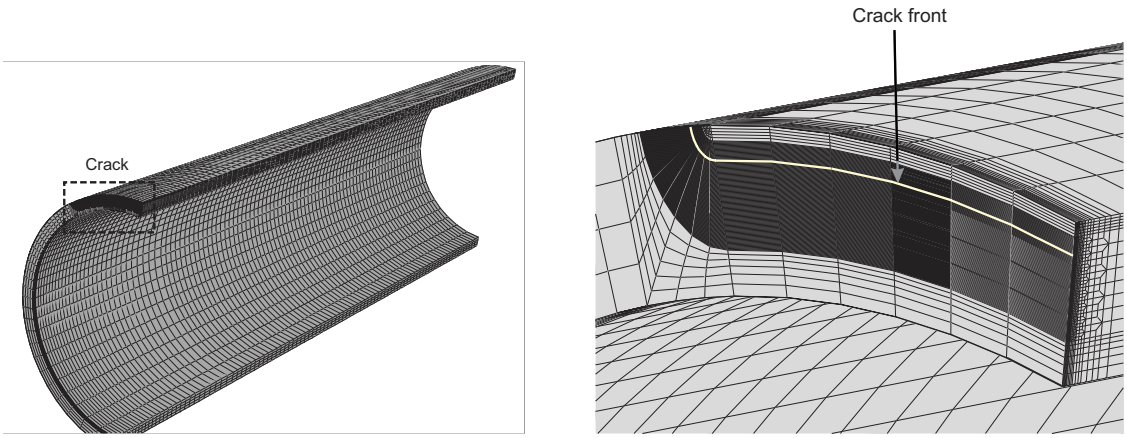

(a) (b)

Figure 3: (a)A typical 3D FE-mesh of one quarter of a pipe containing a surface defect. The dotted frame marks the close-up view of the defect zone shown in (b) where the smallest element size is 0.1 mm, see [13].

Material

The material's plasticity was characterized by an isotropic power-law hardening relationship:

$$\sigma_i = \sigma_0 \left(1 + \frac{\varepsilon_p}{\varepsilon_0}\right)^n, \tag{1}$$

where σ_0 is the stress at the proportional limit, σ_i is the flow stress, ε_p is the plastic strain and n the hardening exponent. $\varepsilon_0 = \sigma_0/E$, is the strain at the proportional limit, and E is Young's modulus. For $\sigma < \sigma_0$ the material behaviour is linear elastic. In the analyses $\sigma_0 = 460$MPa, $E = 200$GPa and the Poisson ratio $\nu = 0.3$.

Three different CTOD-Δa curves were used in the models. Such material curves are obtained from experiments where the ductile crack growth, Δa, and the crack tip opening displacement (CTOD), δ_R, are measured. Similar curves may also be extracted from 3D FEM models including the effect of ductile tearing. Such curves are then used as input to the Link$_{pipe}$ software in the form:

$$\delta_R = c_1 + c_2(\Delta a)^{c_3}, \tag{2}$$

where Δa denotes the ductile crack growth and c_1, c_2 and c_3 are constants. In the following analyses three different c_2 values were chosen in the simulations, Table 1 and Table 2.

Table 1: Input parameters for the FEM-models with 20 and 25mm pipe wall thickness.

Model	a mm	$2c$ mm	c_1	c_2	c_3	$\sigma_h/\sigma_{0.2}$	D mm	D/t
1	3	100	0.45	0.5	0.7	0, 0.25 and 0.5	400 and 500	20
2	3	100	0.45	1.0	0.7	0, 0.25 and 0.5	400 and 500	20
3	3	100	0.45	1.5	0.7	0, 0.25 and 0.5	400 and 500	20
4	4	175	0.45	0.5	0.7	0, 0.25 and 0.5	400 and 500	20
5	4	175	0.45	1.0	0.7	0, 0.25 and 0.5	400 and 500	20
6	4	175	0.45	1.5	0.7	0, 0.25 and 0.5	400 and 500	20
7	5	250	0.45	0.5	0.7	0, 0.25 and 0.5	400 and 500	20
8	5	250	0.45	1.0	0.7	0, 0.25 and 0.5	400 and 500	20
9	5	250	0.45	1.5	0.7	0, 0.25 and 0.5	400 and 500	20

Table 2: Input parameters for the FEM-models with pipe wall thickness 15mm.

Model	a mm	$2c$ mm	c_1	c_2	c_3	$\sigma_h/\sigma_{0.2}$	D mm	D/t
1	3	50	0.45	0.5	0.7	0, 0.25 and 0.5	300	20
2	3	50	0.45	1.0	0.7	0, 0.25 and 0.5	300	20
3	3	50	0.45	1.5	0.7	0, 0.25 and 0.5	300	20
4	4	100	0.45	0.5	0.7	0, 0.25 and 0.5	300	20
5	4	100	0.45	1.0	0.7	0, 0.25 and 0.5	300	20
6	4	100	0.45	1.5	0.7	0, 0.25 and 0.5	300	20
7	5	150	0.45	0.5	0.7	0, 0.25 and 0.5	300	20
8	5	150	0.45	1.0	0.7	0, 0.25 and 0.5	300	20
9	5	150	0.45	1.5	0.7	0, 0.25 and 0.5	300	20

2.1 Results from FEM simulations

In this paper CTOD has been applied as the fracture mechanics parameter for the characterization of initiation and ductile crack-growth. The results are presented as driving force curves, i.e. CTOD versus global strain. Some characteristic features of the driving force curve are shown in Fig. 4, where three different regions are indicated for a pipe subjected to tension. In Region 1 only minor

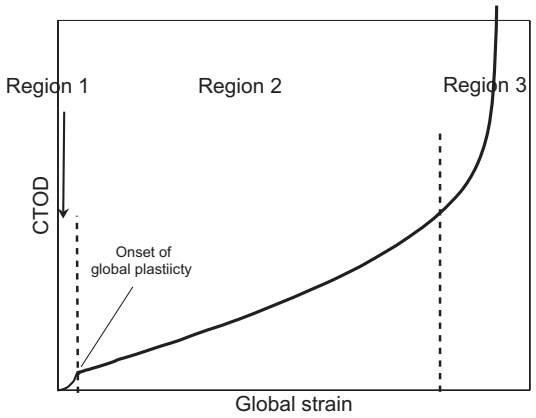

Figure 4: Three characteristic regions on the crack driving force curve.

plastic deformations occur in the crack ligament and the the global deformation is elastic. The main focus in this work is prediction of fracture after global plastic deformation has occurred, Region 2 and Region 3. As the loading increases the plasticity develops through the crack ligament, Region 2, where a relatively linear relationship between the CTOD and global strain is observed. The slight upward curvature of the curve is due to the increase of the local inelastic deformations in the crack ligament and ductile tearing initiation. However, in this region the crack growth will stop if the pipe is unloaded since the material is purely ductile. Finally, Region 3 defines the collapse region with rapid increase of CTOD where large plastic deformations and ductile tearing develop in the crack ligament. The rapid crack growth leads to loss of strain capacity, shown as an almost vertical crack driving force curve, indicating a limit for the pipe's global strain capacity, Jayadevan et al. [24].

Link$_{pipe}$ vs. 3D Abaqus/Explicit

To illustrate the simulation capacity of Link$_{pipe}$ some simulation results are compared with 3D Abaqus/Explicit simulations presented in [13]. These simulations are for the case with $t = 20$mm and $D/t = 20$, subjected to a tension load in

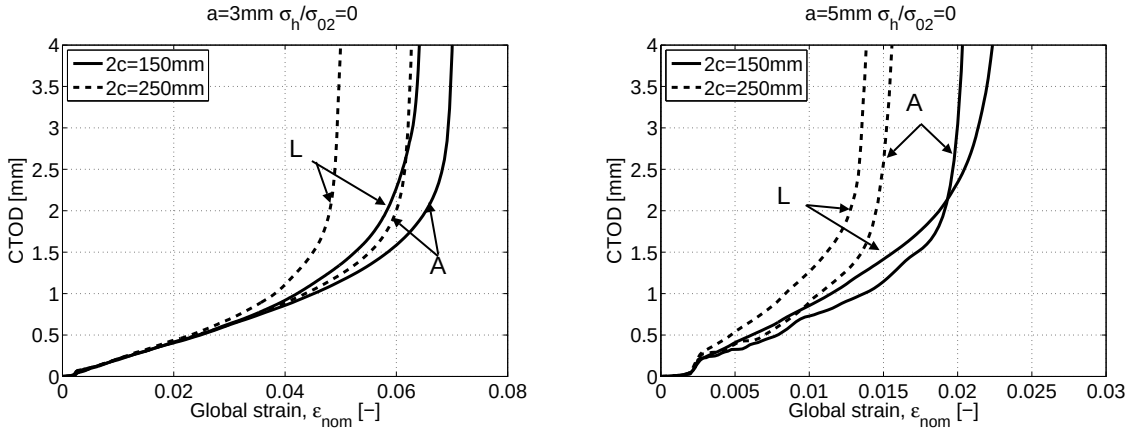

(a) (b)

Figure 5: Comparison of Abaqus/Explicit and Link$_{pipe}$ analyses fortwo different crack lengths, (a) $a = 3$mm and (b) $a = 5$mm.

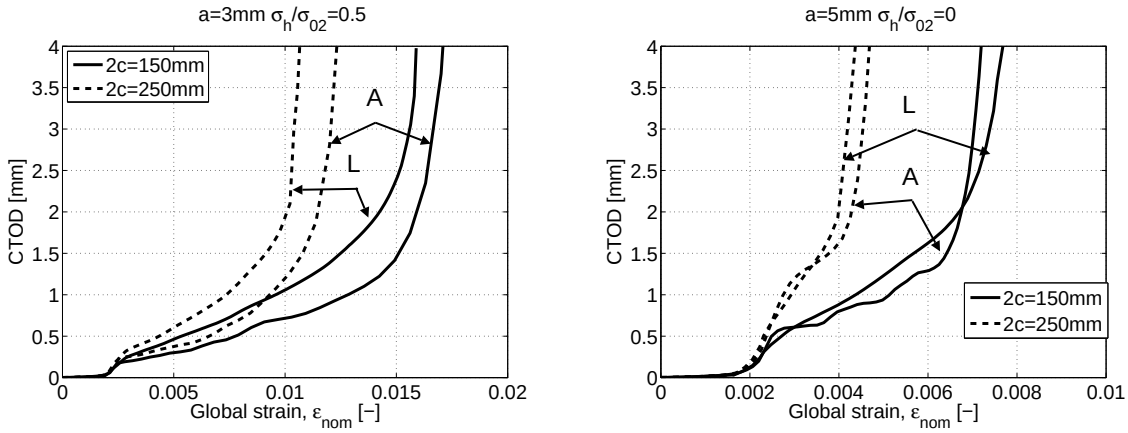

(a) (b)

Figure 6: Abaqus/Explicit vs. Link$_{pipe}$ analyses for pressurized pipes, two crack lengths and (a) $a = 3$mm and (b) $a = 5$mm.

combination with internal pressure. The material resistance input to the Link$_{pipe}$ simulations was obtained from the Abaqus/Explicit simulations as:

$$\delta_R = 0.45 + 1.15(\Delta a)^{0.7}. \tag{3}$$

The Abaqus/Explicit simulations calculate the ductile tearing using the Gurson-Tvergaard-Needleman model whereas Link$_{pipe}$ uses the CTOD-Δa curve to ad-

vance the crack front. It should be noted that Link$_{pipe}$ does not account for the ductile tearing contribution in the hoop direction, but this is not considered to be important in this work. However, development including this effect is ongoing [25].

In Fig. 5(a) the results with $a = 3$mm and $2c = 150$mm and 250mm and no internal pressure are compared. These crack lengths are chosen for comparison since they are in line with the defect sizes in the probabilistic model presented in Section 3. The Abaqus/Explicit and Link$_{pipe}$ results are denoted as 'A' and 'L', respectively. The dotted line refers to the $2c = 250$mm defect, whereas the solid line denotes the $2c = 150$mm defect. For the shorter crack (150mm) the Link$_{pipe}$ analysis yields higher CTOD for a given strain in Region 2. The CTOD values are seen to close up to about ~ 0.6mm, whereafter the CTOD increases faster in the Link$_{pipe}$ simulations. In Region 3 the Link$_{pipe}$ simulation predicts a lower strain capacity. For the longer cracks (250mm) the Link$_{pipe}$ results deviate earlier and more from the Abaqus/Explicit results.

For the deeper defect with $a = 5$mm, Fig. 5(b), Link$_{pipe}$ predicts higher CTOD for the 150mm crack at any given strain level. However, the strain capacity prediction is almost the same as from the Abaqus/Explicit simulation. For the longer crack Link$_{pipe}$ predicts slightly higher CTOD than the 3D simulation. However, the two driving force curves cross at $CTOD \approx 2$mm, resulting in prediction of slightly higher strain capacity in the Link$_{pipe}$ simulation.

A better agreement is observed when an internal pressure giving $\sigma_h/\sigma_{0.2} = 0.5$ is included, Figs. 6(a)-6(b), where the same defect geometries are compared. The Abaqus/Explicit and Link$_{pipe}$ simulations show some difference for the shallower crack, where Link$_{pipe}$ yield higher CTOD values. However, an excellent agreement between the two simulation techniques is obtained when $a = 5$mm, Fig. 6(b). In summary, the Link$_{pipe}$ results are in reasonable accordance with the Abaqus/Explicit simulations and should be suitable for the pipeline fracture assessment considered in this work.

Comparison with experiment

A comparison has been made between a full-scale experiment and an analysis using Link$_{pipe}$ of a surface-cracked pipe subjected to four point bending and internal pressure. The experimental and computational details are not presented here, but the obtained crack driving force curves are depicted in Fig. 7 and are in good agreement. The horizontal lines on the test curve are due to unloading done to perform crack-growth measurements during the test.

Link$_{pipe}$ simulations

This section presents some results from Link$_{pipe}$ analyses conducted to highlight the effects of the parameters investigated.

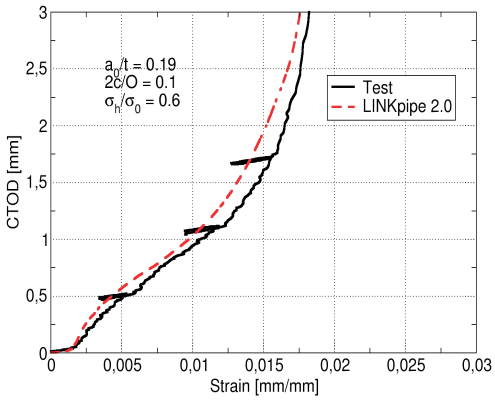

Figure 7: Comparison between Link$_{pipe}$ simulation and a large scale test of a surface-cracked pipe loaded with internal pressure and bending.

Crack depth and crack length

Data presented in Fig. 8(a) illustrates the significant influence of the crack depth variation on the crack driving force:increasing crack depth giving increased CTOD. Region 2 is narrowed as the crack depth increases, which indicates higher plastic deformation localization in the crack ligament. This also influence the ductile crack-growth contribution at a given strain level. Additionally, the strain capacity decreases as the crack depth increases since the crack influences the global capacity. A similar, but weaker, effect is also seen from the crack length variation, Fig. 8(b). However the influence increases with increasing crack depth.

Internal pressure

If the pipe is subjected to tension in combination with internal pressure the defect and pipe reach a bi-axial stress state. The bi-axial loading condition results in a significant stress localization in the crack ligament compared with an non-pressurized pipe case, see e.g. [24]. This explains the considerable loss of strain capacity and corresponding increase in CTOD as the internal pressure is increased, Fig. 9(a).

Pipe wall thickness

Data from three different pipe wall thicknesses, with the same defect geometry and a fixed D/t ratio, is presented in Fig. 9(b). The solid line denotes the crack

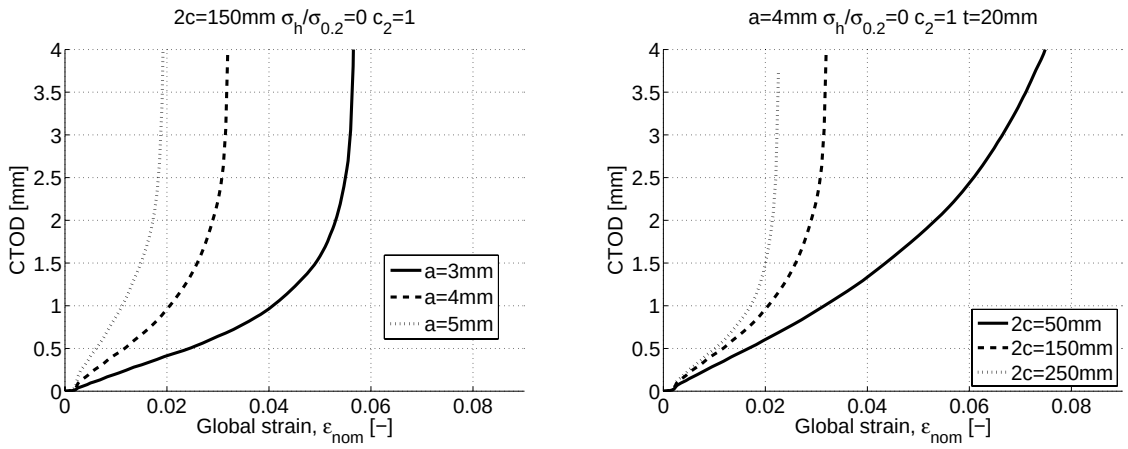

(a) (b)

Figure 8: Driving force curves from Link_{pipe} simulations for different (a) crack depths and (b) crack lengths, for a pipe with thickness 20mm and D/t=20, and no internal pressure.

driving force in the case with $t = 15$mm, whereas the dotted lines represents the 20mm and 25mm cases. The CTOD is definitely higher for the thinnest pipe for a given strain. In addition, as the relative crack depth increases the strain capacity decreases.

Material crack-growth resistance curve

The effect from variation in the material resistance curve is observed in Fig. 10(a). The ductile tearing starts at ~ 0.5mm and the curves deviate significantly as the strain increases. In the case with a "low" resistance curve ($c_2 = 0.5$) the CTOD increases strongly after the ductile crack-growth is initiated. These results demonstrate the importance of the crack-growth resistance curve in determining the strain capacity of pipes with defects.

3 The probabilistic fracture mechanics model

In conjunction with structural reliability analyses of a surface-cracked pipe, we need to establish a convenient model to calculate the failure probability. This is done by solving the probability of failure integral, i.e.

$$p_f = \int_{G(\mathbf{x})\leq 0} f_{\mathbf{X}}(\mathbf{x})\mathbf{dx}. \tag{4}$$

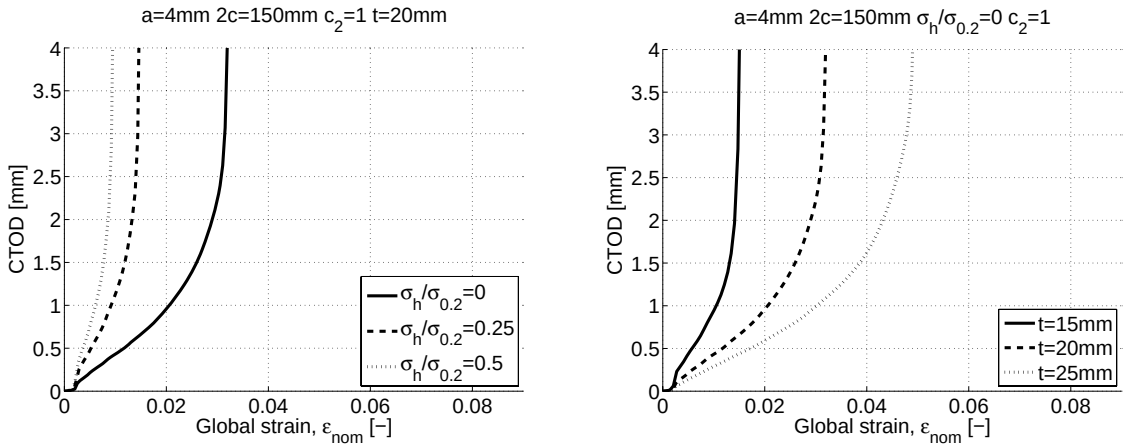

(a) (b)

Figure 9: Driving force curves from Link_{pipe} simulations for different (a) $\sigma_h/\sigma_{0.2}$ and (b) pipe wall thicknesses and no internal pressure.

$f_{\mathbf{X}}(\mathbf{x})$ is the joint probability density function of $\mathbf{X}$. The limit state function is expressed as

$$G(\mathbf{X}) = \varepsilon_{\text{crit}}(\mathbf{X}_1) - \varepsilon_{\text{app}}(\mathbf{X}_2). \tag{5}$$

where $\mathbf{X} = (\mathbf{X}_1, \mathbf{X}_2)$ contains the basic variables. The capacity part is expressed as $\varepsilon_{\text{crit}}(\mathbf{X}_1)$ with the variables of interest represented in the vector $\mathbf{X}_1$. In the present case $\mathbf{X}_1 = (a, 2c, \delta_R, \sigma_h/\sigma_{0.2})$. The "load part" is denoted as $\varepsilon_{\text{app}}(\mathbf{X}_2)$, where the vector $\mathbf{X}_2$ contains the "load" variables.[2] The structural failure region is defined as, $G(\mathbf{X}) \leq 0$, and the safe region as $G(\mathbf{X}) > 0$. Several methods exist to solve the multi-dimensional integral in Eq. (4) [26-28]. A simple numerical integration technique is Monte Carlo Simulation (MCS) with or without sampling techniques, see e.g. Melchers [26]. MCS with importance sampling (MCSI) is convenient to apply in this paper, since the limit state equation is explicitly described. Shinozuka [29] suggested to use the design point as sampling point in **u**-space. The sampling density is represented by a normal distribution for each variable centered around this point.

When FORM and SORM solution techniques are applied, Eq. (4) is solved by performing a mapping from **x**-space with n correlated uncertainty variables $\mathbf{X} = (X_1, X_2, ..., X_n)$ to uncorrelated, independent, standard, normal-distributed variables in **u**-space with uncertainty variables $\mathbf{U} = (U_1, U_2, ..., U_n)$. This is followed by an approximation of the failure surface at the design point, also called the most probable point, with a hyperplane or a parabolic surface. An

[2]It has been chosen to apply the strain due to external loading since the limit state function is expressed in terms of strains.

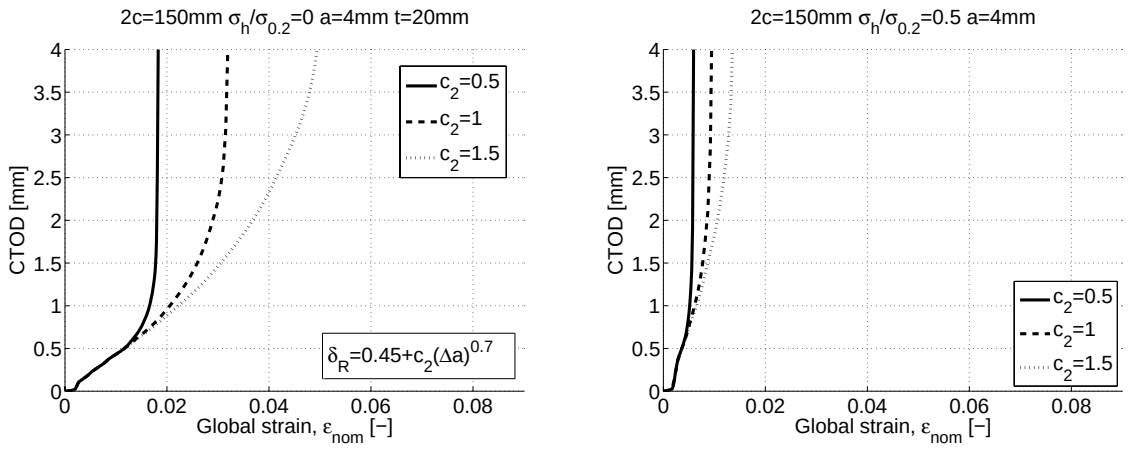

(a) (b)

Figure 10: Link$_{pipe}$ simulation results. Influence due to variation of the c_2 coefficient in the material crack growth resistance curve in Eq. 9. $\sigma_h/\sigma_{0.2} = 0$, $2c = 150$mm, $a = 4$mm and $t = 20$mm in the case (a) without internal pressure and (b) including the effect of internal pressure.

important property from this mapping is that it retains the statistical properties of the probabilistic model. If the limit state function is linearized around the design point using the Taylor expansion in the **u**-space the probability of failure can be approximated from

$$p_f \approx \Phi(-\beta), \tag{6}$$

where Φ is the univariate standard normal integral. The design point represents the point giving the highest probability of failure on a specific failure surface. The distance from the origin to the design point is denoted β, and is known as the safety index. This solution technique is referred to as first order reliability method (FORM). Alternatively, the failure surface can be approximated by a parabolic function around the design point. This solution technique is termed the second order reliability method (SORM), and the theory of this method is found in e.g. Madsen et al. [27] or Melchers [26].

In this work we have employed FORM, SORM, MCS and MCSI. 10^5 simulations were performed to obtain the p_f estimate with MCSI. In general a coefficient of variation (COV) of approximately 1 percent was reached for all the solutions using this method. To verify the MCSI simulations the $t = 20$mm case is solved by using MCS employing 10^7 simulations.

3.1 Failure and response surfaces

The Response Surface Method (RSM) is applied to establish a continuous functional representation of the capacity term, ε_{crit}, Eq. 5. The function is established from the deterministic failure points obtained from the Link$_{pipe}$ simulations and failure criteria presented in Section 3.2.

A second degree polynomial was found to be sufficient to represent the wide range of failure points. Simpler polynomial representations were also employed but the polynomial cross terms were found to be crucial to completely represent the deterministic failure points. The challenge was to establish a rather complex relation between the strain capacity of pipes subjected different loading conditions, defect sizes and material crack-growth resistances. A general second degree polynomial with m variables can be written as

$$\bar{\varepsilon}_{crit} = \alpha_0 + \sum_{i=1}^{m} \alpha_i y_i + \sum_{i=1}^{m} \alpha_{ii} y_i^2 + \sum_{i<j}^{m} \sum^{m} \alpha_{ij} y_i y_j. \tag{7}$$

y_i and y_j denote the variables and the α coefficients are determined through regression analyses and least square optimization. The functions were established with one constraint, a base point, to ensure a qualitatively good fit between the deterministic points and the derived polynomial function[3]. The basis point was the center point from the input values listed in Table 1 and Table 2. This point is denoted as $(a_b, (2c)_b, (\delta_R)_b, (\frac{\sigma_h}{\sigma_{0.2}})_b)$. For the cases with pipe wall thickness 20 and 25mm, the base point values were $a_b = 4$ mm, $(2c)_b = 175$ mm, $(\delta_R)_b = 1.0$, and $(\frac{\sigma_h}{\sigma_{0.2}})_b = 0.25$. The 15mm case is similar but here $(2c)_b = 100$mm, Table 2. When the basis point was chosen the following linear variable transformation was performed prior to the polynomial fit: $y_1 = \frac{a}{a_b} - 1$, $y_2 = \frac{2c}{(2c)_b} - 1$, $y_3 = (\frac{\sigma_h}{\sigma_{0.2}})/(\frac{\sigma_h}{\sigma_{0.2}})_b - 1$ and $y_4 = \frac{\delta_R}{(\delta_R)_b} - 1$. It should be noted that the calculated design point should appear within the region of input values from the deterministic analyses, see i.e. Table 1. This will ensure a more representative estimate of the failure probability than if the design point appears outside the region.

3.2 Failure criteria

The maximum global load criterion for a tension loaded surface-cracked pipe is illustrated in Fig. 11(a). When the maximum load is found the corresponding critical strain, ε_{critG}, is determined. The critical strain is also depicted in Fig. 11(b) where the crack driving force curve is almost vertical.

Alternatively we apply the local failure criterion proposed by Østby et al. [30].

[3]The uncertainty in the established function with respect to the probability of failure estimate is not considered in this work.

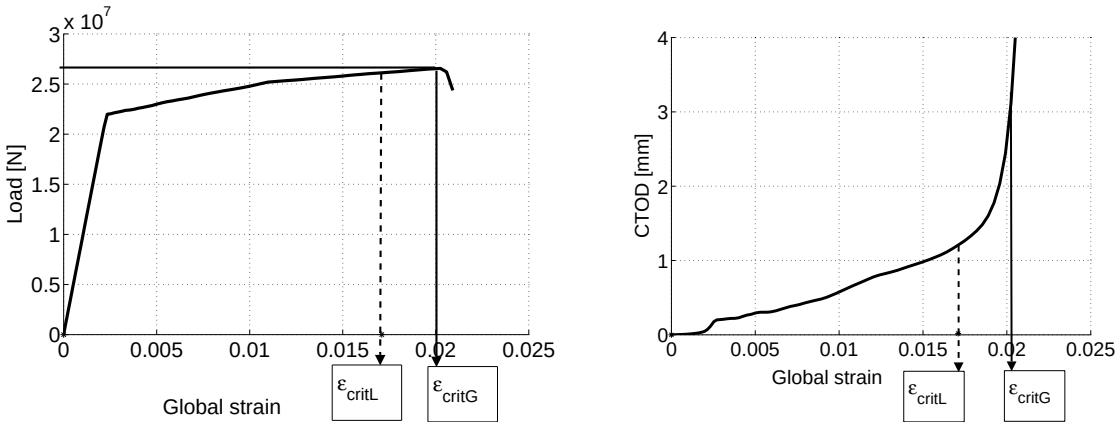

(a) (b)

Figure 11: The critical strain using the maximum load failure criteria (solid lines) and the local failure criteria (dotted line). (a) Load vs. strain curve, (b) CTOD vs. strain for a tension loaded pipe. ε_{critL} and ε_{critG} denote the critical strain using the local and global criterion, respectively.

Table 3: Coefficient values for the response surface established from 4 variables using the local and global failure criteria.

	$t = 15$mm		$t = 20$mm		$t = 25$mm	
	Local	Global	Local	Global	Local	Global
α_0	0.0078	0.0107	0.0093	0.0105	0.0134	0.0180
α_1	−0.0238	−0.0350	−0.0315	−0.0388	−0.0392	−0.0460
α_2	−0.0096	−0.0259	−0.0073	−0.0174	−0.0081	−0.0220
α_3	−0.0054	−0.0115	−0.0091	−0.0142	−0.0142	−0.0207
α_4	0.0111	0.0206	0.0115	0.0191	0.0157	0.0291
α_{11}	0.0337	0.0375	0.0382	0.0413	0.0422	0.0393
α_{22}	0.0090	0.0273	0.0047	0.0168	0.0057	0.0198
α_{33}	0.0021	0.0056	0.0048	0.0078	0.0080	0.0109
α_{44}	0.0001	0.0034	0.0003	0.0047	0.0012	0.0052
α_{12}	0.0089	0.0207	0.0055	0.0145	0.0028	0.0103
α_{13}	0.0157	0.0244	0.0256	0.0303	0.0325	0.0361
α_{14}	−0.0221	−0.0317	−0.0234	−0.0317	−0.0262	−0.0370
α_{23}	0.0027	0.0109	0.0021	0.0081	0.0015	0.0087
α_{24}	−0.0103	−0.0271	−0.0070	−0.0207	−0.0066	−0.0236
α_{34}	−0.0057	−0.0115	−0.0074	−0.0131	−0.0103	−0.0189

This criterion is denoted as ε_{critL}. In this case the CTOD at maximum load, δ_{max}, in the crack ligament is predicted according to the formula

$$\delta_{max} = (0.03(t-a) + \delta_{\Delta a=1mm} - 0.61)(-12.1(\frac{\sigma_{0.2}}{\sigma_{TS}})^2 + 18.9(\frac{\sigma_{0.2}}{\sigma_{TS}}) - 6.28). \quad (8)$$

$t-a$ denotes the ligament height, $\delta_{\Delta a=1}$ mm is the CTOD at 1 mm crack-growth and $\sigma_{0.2}$ and σ_{TS} are the engineering yield stress and tensile strength, respectively. Since the ductile tearing curves starts at $c_1 = 0.45$, $\delta_{\Delta a=1}$ mm was reduced by $CTOD/2 = 0.45/2$mm to reflect the CTOD at initiation. In general this failure criterion predicts similar or lower failure strains than the global criterion dependent on the loading conditions and defect sizes. This is clearly indicated in Figs. 11(a)- 11(b) where the two different criteria are applied for the same case.

3.3 Example

In order to illustrate how the models may be applied, some examples are presented. The PFM-model is customized to represent a pipeline in operation including bending and differential pressure. The results from the tension loaded pipes are applied, but the external load was assumed to form a linear strain variation over the pipe cross-section as depicted in Fig. 12. The crack localization in the circumferential direction was determined from a stochastic sampling using MCS from the uniform distribution for ϕ (Table 4), and the maximum strain at the given defect was obtained. This assumption implies that the defect was subjected to a uniform strain corresponding to the maximum strain. The critical strain for the specific case was obtained from the established capacity response functions. The effective crack length was defined as the part of the defect positioned in the tension part of the pipe cross section. As a consequence, if the defect location passed the top of the pipe (12 o'clock in the cross-section in Fig. 12) the maximum strain was set to remain ε_{lay}. Otherwise, the strain was modified to ε_{mod}.

One load case was investigated for various deterministic pressure levels. It was chosen to represent the load with a corresponding strain, ε_{lay}, since the limit state equation is expressed in terms of strain. Variable X_j was chosen to represent the statistical variation in the material resistance curve with the relation $Z_j = log(X_j)$. This means that the material resistance curve is expressed as

$$\delta_R = c_1 + X_j c_2 (\Delta a)^{c_3}. \quad (9)$$

The input data for the reliability analyses is listed in Table 4.

4 Results of the probabilistic simulations

In Figs. 13-20 the probability of failure, p_f, is plotted against internal pressure, $\sigma_h/\sigma_{0.2}$ for different c_2 coefficients in Eq. 9. Lines are plotted for clarity between

Table 4: Input parameters and distributions used in the analyses.

Description		Distribution	Scale, α	Shape, β	Lower limit
Depth, [mm]	a	Weibull	0.9	1.2	1.8
Length,[mm]	2c	Weibull	33	1	0
			Mean	COV* or StD**	
Strain, [-]	ε_{lay}	Lognormal	0.05 and 0.01	0.3*	0
Angle [-]	ϕ	Uniform	π	-	
Pressure [-]	$\sigma_h/\sigma_{0.2}$		$0-0.5$	-	
δ_R	Z_j	Normal	0	0.11**	
δ_R	c_2	-	$0.5-1.5$		

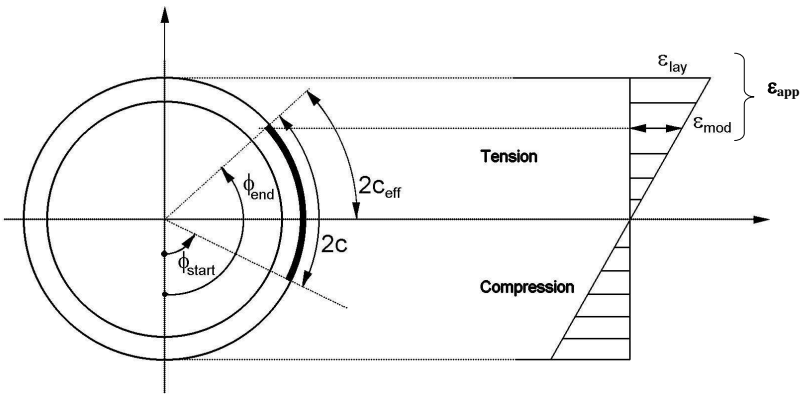

Figure 12: The effective crack length and the applied strain, ε_{app}, in a given pipe cross section for a pipe in bending.

the calculated points. The solid lines refer to the example with $c_2 = 1.5$, the dashed lines $c_2 = 1.0$ and the dotted lines $c_2 = 0.5$ in the material resistance curve. One load case is considered with 1% mean strain in the lognormal distribution in Table 4. A comparison between FORM and SORM solutions is presented

in Fig. 13, where $t = 15$mm and the global criterion is employed. The SORM solutions tend to predict lower failure probabilities for all pressure levels and material resistances, but from a practical point of view the difference is negligible. As a consequence, we do not show this comparison for the other cases.

The SORM results are compared with the MCSI results, in Figs. 14 and 15 for the global and local criteria cases, respectively. There is about half an order of magnitude between the MCSI and the SORM results. This means that approximate solutions using FORM and SORM when solving the integral, Eq. (4), overestimate the probability of failure.

In Fig. 16 the local and global failure criteria are compared with MCSI. As observed, the global criterion predicts lower failure probabilities than the local criterion, which is in line with the illustration in Fig. 11(b). Here ε_{critL} had a lower value than ε_{critG}. Irrespective of the solution technique, the effect of internal pressure is clear: as the internal pressure increases the probability of failure increases. When the c_2 parameter of the CTOD-Δa curve decreases the probability of failure decreases.

Results from the $t = 20$mm case where the global criterion is applied are presented in Fig. 17. The probability of failure increases as the internal pressure increases. From the non-pressurized to the pressurized condition (i.e. $\sigma_h/\sigma_{0.2} = 0-0.5$) a difference of about two order of magnitude is observed for all the curves. Some differences are observed between two different failure criteria depicted in Fig. 18, and the local criterion predicts slightly higher failure probabilities than the global criterion. The difference is largest for the non-pressurized case. In order to ensure that the MCSI solutions produce qualitatively robust results, we performed MCS in the 20mm case for both failure criteria. It was chosen to apply 10^7 simulations, and the results are shown with the symbol '$\mathbf{x}$' in Fig. 18. The MCSI results are plotted with connecting lines for clarity. As seen, the results coincide with the results from the MCSI simulations.

Finally, Figs. 19 and 20 present the results when $t = 25$mm. Similar trends as in the previous case are observed, which means that the local and global criterion yield similar results in the pressurized case, but some differences are observed in the non-pressurized case. The probability of failure is significantly influenced by the internal pressure.

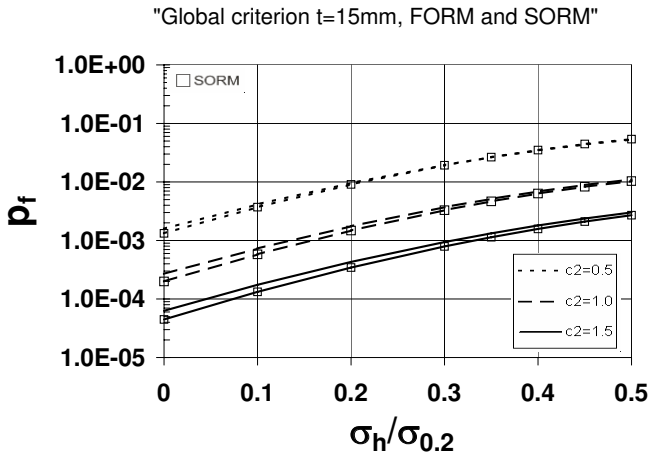

Figure 13: Comparison between SORM and FORM for the $t = 15$mm case using the global failure criterion and 1% mean strain.

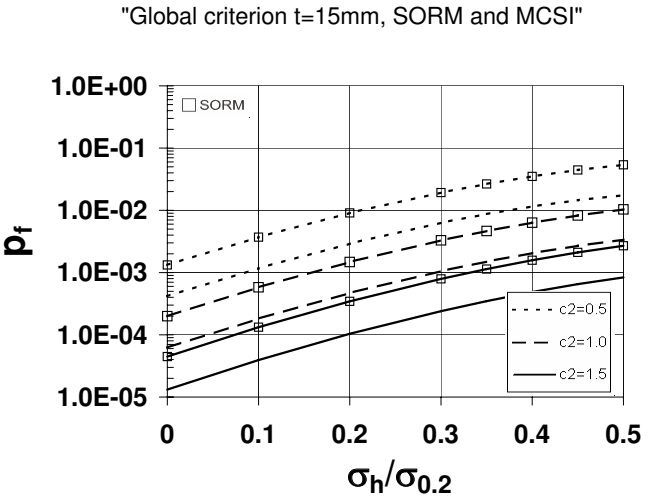

Figure 14: Comparison between SORM and MCSI for the $t = 15$mm case using the global failure criterion and 1% mean strain.

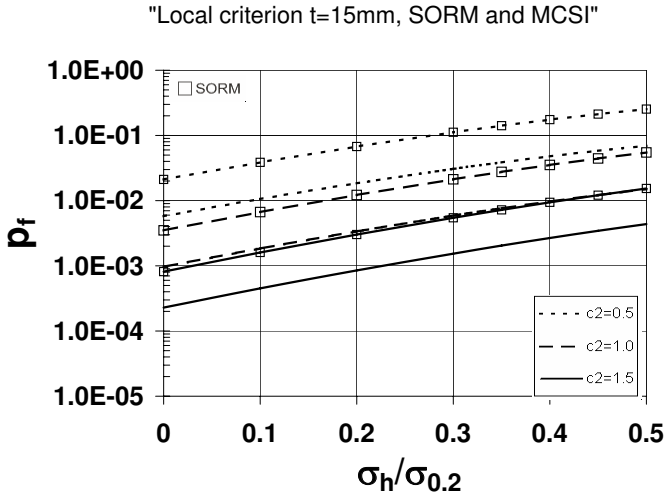

Figure 15: Comparison between SORM and MCSI $t = 15$mm case using the local criterion and 1% mean strain.

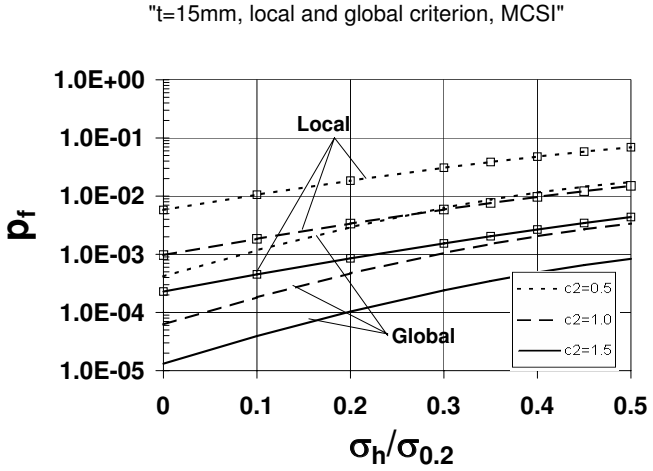

Figure 16: Comparison between the local and global criterion when $t = 15$mm and 1% mean strain. Probability of failure results are obtained from MCSI.

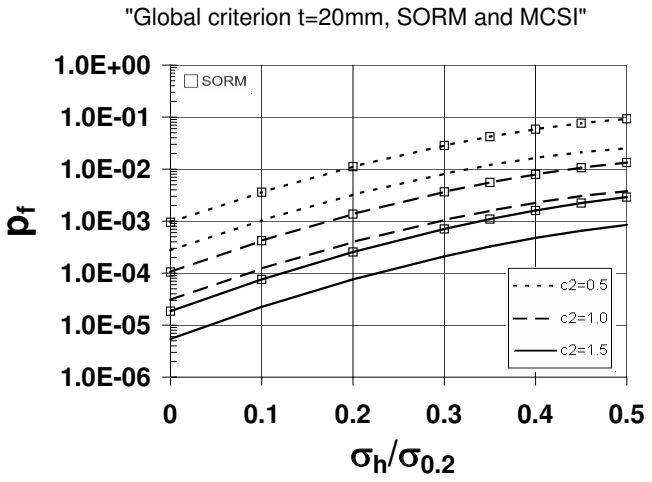

Figure 17: Comparison between SORM and MCSI for the $t = 20$mm case using the global failure criterion and 1% mean strain.

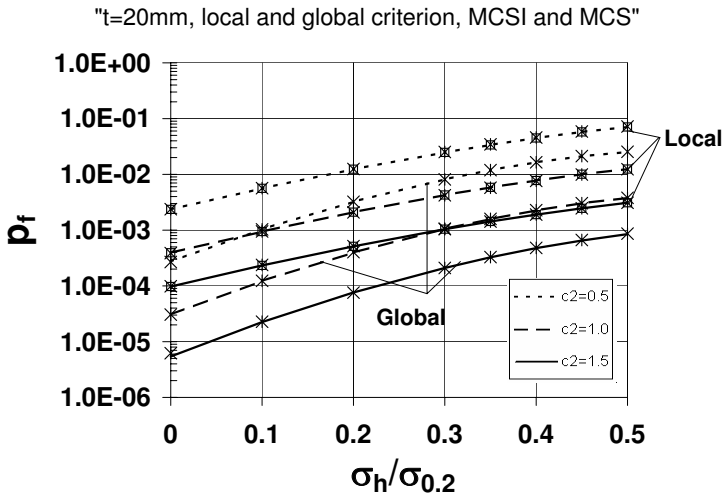

Figure 18: Comparison between the local and global criterion when $t = 20$mm and 1% mean strain. Probability of failure results are obtained from MCSI and MCS ('x' from MCS).

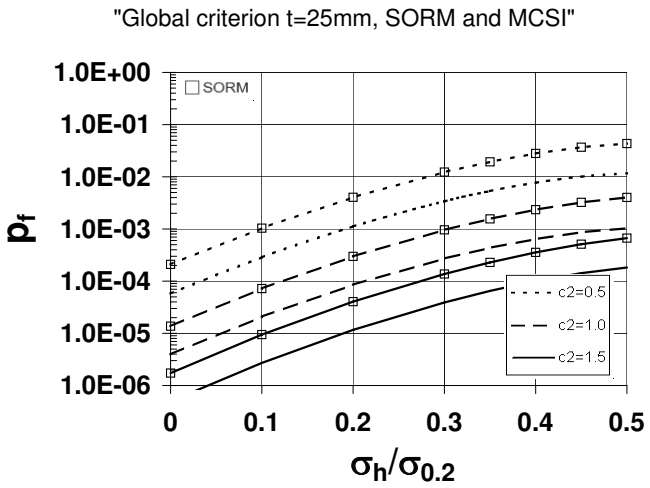

Figure 19: Comparison between SORM and MCSI for the $t = 25$mm case using the global failure criterion and 1% mean strain.

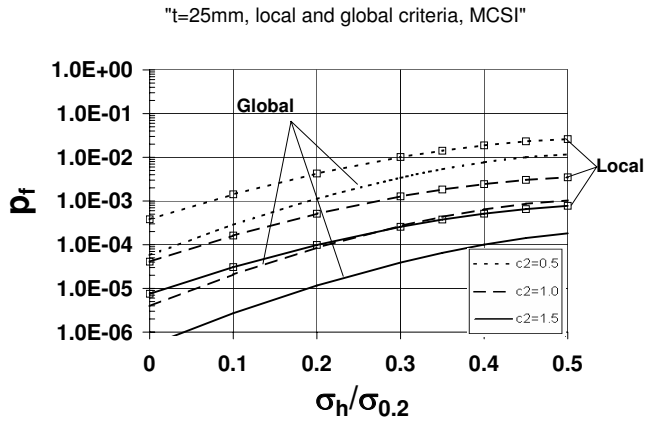

Figure 20: Comparison between the local and global criterion when $t = 25$mm and 1% mean strain. Probability of failure results are obtained from MCSI.

4.1 Discussion

When analysing pipeline fracture in general, two different scenarios should be addressed, i.e. pipeline installation and pipeline operation. In the analyses presented above the same defect distribution and variation in applied strain has been assumed for all cases for convenience. However, when applying the model for practical purposes some topics should be noted. In our cases including internal pressure and a relatively large variation in applied strain are representative for a pipeline in service. In this case usually only a small part of the pipeline is subjected to large deformations, since this typically occurs in relation to free-spans or global buckling phenomena. During installation more or less the whole pipeline is subjected to the same loading, thus there is a system effect that must be accounted for in the probabilistic calculations. Another effect that should be included is the chance of having a defect in at a highly loaded location. This is directly linked to the expected defect rate from the welding procedures. This would probably lead to lower fracture probability levels for the operational cases with internal pressure compared with the reported values above. Consequently, these issues should be addressed and accounted for in practical applications.

5 Conclusions

A probabilistic fracture mechanics model have been established. The model was based on FEM-simulations using shell and line-spring elements. Ductile tearing was included, and the material crack-growth resistance curve was employed to advance the crack front. Link$_{pipe}$ and Abaqus/Explicit simulations were compared. The Link$_{pipe}$ program showed very promising results, and various internal pressure levels, different defect geometries and CTOD-Δa curves were considered. The strain capacity was calculated with two different criteria; the maximum load criterion and a local criterion that predicted the CTOD at maximum load in the crack ligament. These failure criteria were applied to 243 analyses to establish models for each of the three pipe wall thicknesses. Each model was established with four variables, including crack depth, crack length, material resistance and internal pressure. The failure points were used to establish a continuous surface representing the capacity term in the limit state equation. It was shown that a second degree polynomial represented the deterministic failure points satisfactory. Finally, an example on how this model could be applied was presented. The failure probabilities were calculated using FORM, SORM and MCSI. Similar results were obtained from FORM and SORM. However, MCSI around the design point gave robust results and estimated lower failure probabilities than the transformation methods. The failure probability simulations clearly demonstrated the effect of internal pressure and the material resistance curve.

Acknowledgements

The authors wish to express their gratitude to the Joint Industry Project Fracture Control - Offshore Pipelines with the following funding participants: Statoil, Hydro, BP, ENI Norge, Technip and the Research Council of Norway. The assistance from PhD-candidate Espen Berg, stud. techn. Eirin Mohn Lem and stud. techn. Pål Are Eikrem at The Norwegian University of Science and Technology is also appreciated.

References

[1] C. Thaulow, B. Skallerud, K. Jayadevan, E. Berg, Fracture control offshore pipelines - advantages of using direct calculations in fracture assessments of pipelines, In: 24th International Conference on Offshore Mechanics and Arctic Engineering (2005).

[2] SINTEF, Fracture control-offshore pipelines (JIP), Trondheim, Norway, 2002-2006.

[3] E. Østby, Fracture control offshore pipelines - new strain-based fracture mechanics equations including the effects of biaxial loading, mismatch, and misalignment, 24th International Conference on Offshore Mechanics and Arctic Engineering (2005).

[4] DNV-OS-F101, Offshore standard, submarine pipeline system, Standard, Det Norske Veritas (2000).

[5] Y. Chen, S. Lampert, Numerical modeling of ductile tearing for elliptical surface cracks in wide plates, International Journal of Pressure Vessels and Piping 82 (2005) 417–426.

[6] S. Rahman, A stochastic model for elastic-plastic fracture analysis of circumferential through-wall-cracked pipes subject to bending, Engineering Fracture Mechanics 52 (2) (1995) 265–288.

[7] S. Rahman, Probabilistic fracture analysis of cracked pipes with circumferential flaws, International Journal of Pressure Vessels and Piping 70 (1997) 223–236.

[8] S. Rahman, F. Brust, Approximate methods for predicting J-integral of a circumferentially surface-cracked pipe subject to bending, International Journal of Fracture 85 (1997) 111–130.

[9] S. Rahman, Probabilistic elastic-plastic fracture analysis of circumferentially cracked pipes with finite-length surface flaws, Nuclear Engineering and Design 195 (2000) 239–260.

[10] M. Francis, S. Rahman, Probabilistic analysis of weld cracks in center-cracked tension specimen, Computers and Structures 76 (2000) 483–506.

[11] S. Rahman, G. Chen, R. Firmature, Probabilistic analysis of off-center cracks in cylindrical structures, International Journal of Pressure Vessels and Piping 77 (2000) 3–16.

[12] J. Foxen, S. Rahman, Elastic-plastic analysis of small cracks in tubes under internal pressure and bending, Nuclear Engineering and Design 197 (2000) 75–87.

[13] A. Sandvik, E. Østby, C. Thaulow, A probabilistic fracture mechanics model including 3D ductile tearing of bi-axially loaded pipes with surface cracks, Accepted with minor revision to Engineering Fracture Mechanics.

[14] A. Sandvik, E. Østby, C. Thaulow, Probabilistic fracture assessment of surface cracked pipes using strain-based approach, Engineering Fracture Mechanics 73 (2006) 1491–1509.

[15] J. Rice, N. Levy, The part through surface crack in an elastic plate, Journal of applied mechanics (1972) 185–194.

[16] H. Lee, D. Parks, Enhanced elastic-plastic line spring finite element, International Journal of Solids and Structures 32 (1995) 2393–2418.

[17] H. Lee, D. Parks, Line-spring finite element for fully plastic crack growth-I. formulation and one-dimensional results, International Journal of Solids and Structures 35 (36) (1998) 5115–5138.

[18] H. Lee, D. Parks, Line-spring finite element for fully plastic crack growth-II. surface cracked plates and pipes, International Journal of Solids and Structures 35 (36) (1998) 5139–5158.

[19] F. McClintock, Y.-J. Kim, D. Parks, Test for fully plastic fracture mechanics of plane strain mode i crack growth., In:Constraint effects in fracture: Theory and applications, ASTM STP 1256, ed. M. Krik and A. Bakker (1995) 199–222.

[20] B. Skallerud, B. Haugen, Collapse of thin shell structures-stress resultant plasticity modelling within a co-rotated andes finite element formulation, International Journal for numerical methods in engineering 46 (1999) 1961–1986.

[21] B. Skallerud, Numerical analysis of cracked inelastic shells with large displacements for mixed mode loading, International Journal of Solids and Sturctures 36 (1999) 2259–2283.

[22] B. Skallerud, K. Holthe, B. Haugen, Thin shell and surface crack finite elements for simulation of combined failure modes, Computer methods in applied mechanics and engineering 194 (2005) 2619–2640.

[23] K. Jayadevan, E. Berg, C. Thaulow, E. Østby, B. Skallerud, Numerical investigation of ductile tearing in surface cracked pipes using line-springs, International Journal of Solids and Structures 43 (2006) 2378–2397.

[24] K. Jayadevan, E. Østby, C. Thaulow, Fracture response of pipelines subjected to large plastic deformation under tension, International Journal of Pressure Vessels and Piping 81 (2004) 771–783.

[25] E. Berg, B. Skallerud, C. Thaulow, Circumferential crack growth and two-parameter fracture mechanics in surface cracked pipe-lines using line-spring elements, Preprint submitted to Elsevier Science.

[26] R. Melchers, Structural reliability analysis and prediction, 2nd Edition, John Wiley & Sons, 1999.

[27] H. Madsen, S. Krenk, N. Lind, Methods of structural safety, Prentice Hall, 1986.

[28] P. Thoft-Christensen, M. Baker, Structural Reliability Theory and its Applications, 1st Edition, Springer-Verlag, Berlin, Germany, 1982.

[29] M. Shinozuka, Basic analysis of structural safety, Journal of Structural Engineering 109(3) (1983) 721–740.

[30] E. Østby, E. Torselletti, E. Levold, A strain-based approach to fracture assessment of pipelines, FITNET 2006 Conference, Paper no. 35, 17-19th of May 2006, Amsterdam, The Netherlands.